UNIVERSITÀ
degli STUDI
di CATANIA

Dipartimento
di Fisica
e Astronomia
"Ettore Majorana"

PhD programme in physics

Federico Bonasera

Manipulation and analysis of topological properties in hybrid Dirac materials

PhD thesis

Supervisors:
Prof. Elisabetta Paladino
Prof. Francesco M.D. Pellegrino

academic year 2024/2025

Contents

Introduction

In recent years, the Landau paradigm of classifying phases of matter through symmetry breaking mechanisms and order parameters has proven incapable of capturing new classes of systems [1]. These systems exhibit a different kind of order, known as topological order, and a more robust and general framework rooted in topology has emerged for their characterization [2–10]. In topologically non-trivial systems, the wavefunction describing the ground state is fundamentally different from that of trivial states of matter, such as an atomic insulator: the two cannot be adiabatically connected without undergoing drastic changes in the band structure of the system, e.g. closing or opening a gap. The non-triviality of the system wavefunction is measured in terms of quantized topological invariants that, as the name suggests, remain unchanged under adiabatic transformations of the system, as long as there are no structural modifications in the band structure. The first experimental realization of a topological system has been the Integer Quantum Hall State (IQHS) in 2D electron gases subjected to strong magnetic fields [1]. The ground state wavefunction of this system is characterized by a $\mathbb{Z}$ integer number, known as the Chern number [3,11]. After the IQHS, the first material discovered to manifest topological order without an external magnetic field was the topological insulator state in HgTe/CdTe semiconductor quantum wells [12]. In such a system, the strong spin-orbit interaction opens an inverted band gap in which the valence band wavefunction inherits properties from the conduction one. In this way, it is impossible to restore the normal insulating phase without closing the band gap. Moreover, the band gap is protected against any interaction that preserves time-reversal symmetry, and for this reason, topological band insulators are among the symmetry-protected topological states.

From the discovery of the first topological insulator, new materials have been found that are topologically non-trivial. Among these there are gapped phases such as the topological crystalline insulator [13], in which the topological state is protected by crystalline symmetries, or the theoretically proposed topological superconductor [14, 15]; and gapless phases in which the Fermi surface is composed of band touchings that act as topological defects [10]. These band touchings can vary in dimensionality, and in the directions away from the degeneracy the energy dispersion is linear. For this reason, these gapless topological phases are broadly known as Dirac materials. Among the others, in a three dimensional Brillouin zone we can have the Nodal Line Semimetal (NLSM), which is characterized by linear valence and conduction bands that cross each other along a one-dimensional curve at the Fermi energy [9, 10, 16], and the Weyl Semimetal (WSM), in which the linear valence and conduction bands touch each other at single points, known as Weyl Point (WP) [8, 17]. As we will see in the first part of this thesis, WPs act either as a source or a sink of a quantum of Berry flux, which is the essence of the Chern number invariant, and because of this they are fundamental in the description of both gapless and gapped topological phases. If, for example because of spin degeneracy, four bands linearly meet at a single point of degeneracy, this point is known as Dirac Point (DP), in analogy with the description of relativistic particles in quantum field theory, and the system as Dirac Semimetal (DSM) [8, 17]. Graphene is an example of DSM in two spatial dimensions.

One of the most dramatic effects of a non-trivial topology in many materials is the existence of metallic, dissipationless, and symmetry-protected states that occur at the boundaries of the sample. This property is known as bulk-boundary correspondence. It was first discovered in the context of the IQHS [18], where a bulk Chern number ν (one for each filled Landau level) predicts the existence of ν edge states that results in a quantized Hall conductance of $\sigma_{xy} = \nu(e^2/h)$, and it was then predicted and observed also in topological insulators [6,7,10,12,19–21], NLSM [9,10,22–30], WSM [8, 10, 31–40] and in DSM [8, 10, 41–45]. In WSM, in particular, at least two WPs are found in the band structure and, in momentum slices between them, the system effectively behaves as a 2D IQHS of unit Chern number and with characteristic conductive surface states. Hence, the defining features of a WSM are an open Fermi arc at the surface of the sample and a non-quantized Anomalous Hall Effect [8].

Recently, interest in topological materials has shifted towards their potential applications in quantum technologies [14,46–53]. In fact, the robustness of their topological properties against weak perturbations makes these materials good candidates as efficient platforms for quantum computing [14, 54]. In this framework, the problem of controlling and engineering these topological phases of matter arises.

In particular, the Floquet engineering of a system through a periodic drive has been the subject of a wide theoretical investigation [25, 55, 56, 56–88], and experimental studies on the subject have also been performed [66, 89–94]. The concept of Floquet engineering has also been recently applied to topological systems with the aim of, for example, creating anomalous topological states with no static counterpart [56, 61, 71–80, 95] and, in particular, of inducing topological phase transitions [25, 62, 63, 69, 81–84, 96, 97]. Specifically, it was predicted that irradiating a NLSM with circularly polarized light induces, to first order in the inverse frequency of light $1/\omega$, a transition to a Floquet-Weyl Semimetal (FWSM) phase with tunable WPs [85–88]. Moreover, the study of interface states between materials comprising topological ones has raised a lot of interest. It has been proved, in fact, that these interface states can have substantially different properties compared to open surfaces ones [98] or even an entirely different phase of matter [99, 100]. Thus, the first part of this thesis is devoted to the detailed study of the interface state, especially its energy dispersion and pseudo-spin texture, which emerges when two regions of a spinless NLSM are illuminated with opposite light polarizations at zero temperature. Indeed, the difference in light polarization provides the two induced FWSMs with opposite Chern numbers (± 1), thus generating two interface states. The most interesting aspect of this setup is its high tunability: both Chern numbers and the WPs position depend on the polarization and intensity of the light. It is then possible to explore various scenarios, based on the relative positions of the WPs, that lead to tunable van Hove singularities and topological interface states, which can be experimentally reproduced and possibly lead to future device applications.

In the second part of this thesis, instead, we are going to focus on graphene. In particular, we study how substrate engineering via the proximity effect, which can modify the topological properties of the system, affects its superconducting transport properties in a Graphene Josephson Junction (GJJ).

Josephson Junction (JJ) have an extensive role as vital components in quantum information processing applications, such as in qubits [101]. In particular, the semiconductor-based JJ has opened up new possibilities for superconducting qubits with a gate-tunable ratio between the Josephson and the charging energies, E_J/E_C. Implementations of this kind have been made with a variety of materials [102–106], including graphene [107]. Moreover, semiconductor-based JJ often work in the quasi-ballistic regime and are characterized by a few high transmission channels that produce a skewed Current-Phase Relation (CPR) with higher harmonic content [103,108,109]. The highly skewed CPR is at the base of multiterminal topological effects [110–112] and of implementations of high-efficiency superconducting diodes [113, 114] and parity protected $\sin(2\phi)$ qubits [114–116]. Graphene is one of the most promising materials for such applications. In fact, thanks to advances in the fabrication of encapsulated graphene, it is now possible to produce high-quality superconducting graphene heterostructures [117–119]. These systems show ballistic transport, gate-tunable supercurrents, and forward-skewed CPRs [120–128]. Graphene is a 2D DSM with two inequivalent DPs that define its valley degree of freedom. In its pristine form (only the kinetic Hamiltonian), the graphene layer is topologically trivial. Nevertheless, even with just a small mass term, the presence of the two separate Dirac points provides each valley of the system with some independent topological properties; provided that the sample preserves the valley degree of freedom. Indeed, each valley of graphene is characterized by an independent quantization, to half an integer, of the Chern number. This leads to peculiar transport properties such as the valley Hall effect [129] and to the existence of kink edge states at an interface between trivially gapped graphene layers with opposite mass terms [130]. When considering Spin-Orbit Coupling (SOC) in graphene, its phase diagram becomes even richer. In the two seminal papers [4, 19], Kane and Mele proved that in a certain SOC parameter range graphene can become a Quantum Spin Hall State (QSHS), a 2D topological insulator, described by a $\mathbb{Z}_2 = \{0, 1\}$ index and characterized by two helical edge states (one per spin) that circulate in opposite directions along the edges of a sample. More recently, it was found that for other SOC values graphene can establish a gapped (trivial) phase characterized by both spin-polarized and time-reversal protected *pseudo*helical edge states together with valley-polarized ones, a phase that was dubbed Quantum Valley Spin Hall State (QVSHS) [131]. Unfortunately, pristine graphene was shown to have an intrinsic SOC too weak to produce an observable effect [132]. For these reasons, substrate engineering of proximity-induced SOC can have a profound impact on tailoring the properties of the graphene layer. First-principles and experimental studies demonstrate that graphene on transition metal dichalcogenides heterostructures can exhibit strong proximity-induced SOC without compromising the Dirac dispersion [133–139]. For example, it was experimentally proved that graphene on WSe_2 shows an enhanced robustness of the supercurrent for extremely high magnetic fields [140], which could be a consequence of the edge transport due to the non-trivial QSHS or QVSHS graphene phase.

Our analysis of the superconducting transport properties of proximitized graphene is divided into bulk contributions and finite width effects. In the former, we focus on the short and wide junction limits, in which the junction length is much smaller than the coherence length of the superconductors. We employ an analytical approach and use a low-energy description of graphene based on the continuum low-energy Hamiltonian. We thus compute the effect on the critical current and skewness of the CPR of the different types of SOCs that are induced in proximitized graphene. We find that depending on the modifications of the band structure, these different terms result in a wide range of effects on the CPR of the junction. Among them, a Rashba SOC, while having little effect on the critical current of the CPR, produces heavy swings in its skewness, allowing for a tunable harmonic content. In the finite width section, we compute the edge contribution to the transport, for Fermi level values inside the energy gap, and analyze its robustness against scalar disorder in the form of edge roughness. We also analyze the magnetic interference pattern of the critical current for a junction of finite width. We find that at high magnetic fields the interference pattern is dominated by robust oscillations that slowly decay with the strength of the magnetic field, which is consistent with the localized nature of the edge transport. For magnetic fields of low intensities we also find clear signatures of non-reciprocal transport which leads to a Superconducting Diode Effect (SDE) with efficiencies up to 60%. The root cause of this effect is found to reside in asymmetric edge transport and a minimal transport model that reproduces the result is given.

This thesis is organized into four chapters as follows.

Chapter 1 provides the theoretical background necessary for our study of topological phases in Dirac materials, in particular WSMs and graphene. We start by introducing the Dirac equation and its topological aspects: with due modifications, the Dirac equation will be the central analytical model throughout the rest of this work. After a brief introduction on the Berry curvature and the Chern theorem, we explore the concept of conical intersections and WPs, which are essential in the understanding of topological materials in general, and of WSMs and graphene in particular. We will then show how it is possible to tune the topological properties of these materials. We will explicitly show how one can induce a topological transition in a NLSM system to a tunable FWSM state via light irradiation; and we will analyze how, via proximity coupling, a substrate can modify the properties of a graphene layer and, in particular, of its edge states. The Chapter ends with a brief overview of superconductivity and superconductive transport in JJ, described in terms of Andreev Reflection (AR) and Andreev Bound State (ABS).

In *Chapter 2*, we present the first original work of this thesis: the analysis of the interface system between two FWSMs. The interface is created by irradiating a NLSM with two monochromatic light beams of opposite circular polarization. Due to the topological mismatch between the two sides of the junction, the interface can host up to two interface modes for a given 2D momentum projection. The electronic structure and pseudospin texture of the interface states are subsequently investigated. The results demonstrate that the interface system exhibits a highly tunable band structure, with the possibility of inducing van Hove singularities in the density of states. Furthermore, it is shown that the introduction of a narrow magnetic barrier enables the realization of a switchable topological state at the interface, which can be controlled by adjusting the intensities of the incident light beams.

In *Chapter 3*, we analyze the effects of proximity-induced interactions in the CPR of a short and wide GJJ. The analysis starts by introducing the low energy Hamiltonian and the transfer matrix method, which are used to compute the transmission probabilities across a normal ballistic graphene stripe. Then, using methods elaborated in *Chapter 1*, these transmissions are directly linked to the CPR of the GJJ, which is investigated under the effects of Kane-Mele Spin-Orbit Coupling (KM-SOC), valley-Zeeman Spin-Orbit Coupling (VZ-SOC), and Rashba Spin-Orbit Coulping (R-SOC), as well as of an onsite scalar potential. First, we study the cases without R-SOC, which we were able to fully compute analytically. Already at this stage, the results reveal a broad range of effects on both the critical current and skewness: while the KM-SOC and onsite potential terms significantly suppress them, the VZ-SOC enhances both, acting as a valley-dependent chemical potential. Finally, we introduce the R-SOC and resort to solving the problem numerically for some of the most experimentally relevant parameter values. Interestingly, we find that a R-SOC can produce heavy swings in the skewness of the CPR, allowing for GJJ with a tunable harmonic content.

Chapter 4 is devoted to the analysis of the finite-width effects in a setup similar to that studied in Chapter 3. This is done numerically by performing tight-binding simulations using the KWANT Python package. Due to its rich edge behavior and to its experimental plausibility, we focus on the aforementioned QVSHS of graphene. Firstly, we examine how the edge contribution affects superconducting transport by considering the system's Fermi level and various types of edge terminations. Subsequently, we proceed to investigate the robustness of the system with respect to edge disorder and conclude with an examination of the magnetic interference pattern observed in the junction.

List of Acronyms

ABS Andreev Bound State

AR Andreev Reflection

CPR Current-Phase Relation

DP Dirac Point

DSM Dirac Semimetal

FWSM Floquet-Weyl Semimetal

GJJ Graphene Josephson Junction

IQHS Integer Quantum Hall State

JJ Josephson Junction

KM-SOC Kane-Mele Spin-Orbit Coupling

NLSM Nodal Line Semimetal

QSHS Quantum Spin Hall State

QVSHS Quantum Valley Spin Hall State

R-SOC Rashba Spin-Orbit Coulping

SDE Superconducting Diode Effect

SOC Spin-Orbit Coupling

SQUID Superconducting Quantum Interference Device

VZ-SOC valley-Zeeman Spin-Orbit Coupling

WP Weyl Point

WPP Weyl Points surface Projection

WSM Weyl Semimetal

Chapter 1

Topology in Dirac materials

The discovery of topological materials has opened a vibrant frontier in condensed matter physics, where the interplay between symmetry, topology, and band structure gives rise to remarkable physical phenomena. One of the hallmarks of topological matter is the prediction, via the *bulk-boundary correspondence*, of topologically protected edge states that live on the boundaries of the sample. The Dirac Hamiltonian and its variants are ubiquitous in the description of many topological systems, that collectively are referred to as Dirac materials. We will see how the Dirac Hamiltonian naturally predicts edge states between regions with different mass signs and how it can be generalized to model real condensed matter systems.

In this chapter, we begin by introducing the Dirac Hamiltonian and its central role in capturing the essential physics of topological materials. We will then quickly review the mathematical concept of Berry curvature and the Chern theorem, which together form the backbone of the modern understanding of topological invariants. We then examine the concept of 3D conical intersections and their influence in the topology of 2D Brillouin zones. This will set the basis for the introduction of the generalizations of the Dirac Hamiltonian to describe the two main characters of this thesis: the WSM and graphene. We will then describe how the topology of a FWSM can be influenced via light-irradiation of a NLSM, and how the interaction with a substrate can modify the topological properties of a graphene layer. Finally, we conclude the Chapter discussing superconductivity and transport in a JJ via means of AR and ABS.

Through this progression, the chapter lays the conceptual groundwork for the rest of the thesis, establishing both the theoretical tools and the physical context necessary for the study of Dirac materials.

1.1 The Dirac equation and its topological properties

Since most electronic properties are governed by states near the Fermi energy, a material is often modeled through the electronic bands arising from weakly bound valence orbitals of its constituent atoms. In a minimal model, we can focus only on the very few bands closest to the Fermi energy. We generally consider the last occupied and first non occupied bands close to the Fermi energy (or two with spinful electrons), still capturing the essential low-energy physics of the system. The Dirac Hamiltonian falls into this minimal model description.

The Dirac equation was proposed as a relativistic counterpart to the Schrödinger equation by P.A.M. Dirac in 1928. The Dirac Hamitonian proposed to describe the dynamics of relativistic particle is

$$H_D = c\boldsymbol{\alpha} \cdot \boldsymbol{p} + \beta m c^2, \tag{1.1}$$

where $\boldsymbol{p}$ is the momentum, m is known as the mass term, c is the speed of light and the matrices $\{\beta, \alpha_i\}$ square to 1 and anti-commute with each other. In three dimensions the four matrices must at least be of dimension 4 and solving the time-independent problem gives four independent solutions that differ for spin and energy. The negative energy solutions posed a great problem of interpretation, the solution of which led to the discovery of the positron.

In a condensed matter setting, the negative solutions of Eq. (1.1) do not present any interpretational difficulty, as they can naturally be identified with valence-band electrons whose energy is negative relative to the Fermi level. In this way, the Dirac Hamiltonian serves as an effective model for capturing the dynamics of a gapped system in the vicinity of the Fermi energy. The relevance of the Dirac Hamiltonian in describing topological states can be hinted at through the bound state solutions that emerge at the interface between two regions of opposite mass. Considering a 2D system, Eq. (1.1) can be rewritten as

$$h(x) = vp_y\alpha_y + vp_x\alpha_x + m(x)v^2\beta \tag{1.2}$$

where we have used a general velocity v and where

$$m(x) = \begin{cases} -m_1 & \text{for} \quad x < 0 \\ m_2 & \text{for} \quad x > 0 \end{cases}, \tag{1.3}$$

with $m_1 m_2 > 0$. It can be shown that this system holds two conductive interface states [141] given by

$$\Psi_\pm(x, k_y) = \sqrt{\frac{v}{h}\frac{m_1 m_2}{m_1 + m_2}}\, \phi_\pm \, e^{-|m(x)vx|/\hbar + ik_y y} \tag{1.4}$$

where $\phi_+ = (i, 0, 0, 1)^T$ and $\phi_- = (0, i, 1, 0)^T$. Their energy is found as $E_\pm = \pm v\hbar k_y$ with an effective velocity $v_\pm = \pm v$, meaning that each state carries a current along the interface, but electrons with opposite spins move in different directions. In some way, these edge states are precursor of the helical edge states of the Quantum Spin Hall Effect, which we will see in Sec. 1.5.3 when dealing with graphene on a substrate.

The difficulty with employing Eq.(1.1) to describe topological materials lies in the symmetry between positive and negative masses. In fact, the Hamiltonians corresponding to positive and negative mass are connected through a unitary transformation that flips $\beta \to -\beta$ while leaving α_i unchanged. As a consequence, the sign of m alone does not allow one to distinguish whether a system is topologically trivial or not. One might attempt to resolve this by assigning, for instance, an infinite *positive* mass to the vacuum as a reference, and then defining as "topological" those systems governed by a Dirac equation with negative mass. However, since the appearance of bound states is intrinsically dictated by the band structure, the introduction of such a vacuum benchmark should not be necessary. We are thus led to conclude that the Dirac Hamiltonian in Eq.(1.1) is inadequate for the description of topological systems. The problem can be solved with the introduction of quadratic corrections as [141]

$$H = c\boldsymbol{\alpha} \cdot \boldsymbol{p} + \beta(mv^2 - B\boldsymbol{p}^2). \tag{1.5}$$

The quadratic term $B\boldsymbol{p}^2$ breaks the symmetry between positive and negative masses: for $mB > 0$ the Hamiltonian reduces to a form proportional to β at $|\boldsymbol{p}| = 0$, whereas for $|\boldsymbol{p}| \gg 1$ it becomes proportional to $-\beta$, making it topologically distinct from the $mB < 0$ case. With minor adjustments, the Hamiltonian of Eq. (1.5) will therefore serve as the principal model used throughout this thesis.

1.2 Quick review of the Berry curvature and the Chern theorem

Considering a N-dimensional parameter space, every state of the system will be a function of the N parameters $|u(\lambda_1, \ldots, \lambda_N)\rangle = |u(\boldsymbol{\lambda})\rangle$. We can introduce the *Berry connection* as a $\boldsymbol{\lambda}$-dependent N-dimensional vector $\boldsymbol{A} = (A_1, \ldots, A_N)$ with

$$A_\mu = \langle u(\boldsymbol{\lambda})|i\partial_\mu u(\boldsymbol{\lambda})\rangle, \tag{1.6}$$

where $\partial_\mu = \partial/\partial\lambda_\mu$. We can then define the *Berry phase* around any loop in parameter space as the integral of the Berry connection

$$\phi = \oint \boldsymbol{A} \cdot d\boldsymbol{\lambda} \ (\text{mod } 2\pi), \tag{1.7}$$

where the (mod 2π) operation is needed to keep ϕ a gauge invariant quantity. In a 3D parameter space we can apply Stokes' theorem and write

$$\oint_{\partial S} \boldsymbol{A} \cdot d\boldsymbol{\lambda} := \int_S \boldsymbol{\Omega} \cdot d\boldsymbol{S}. \tag{1.8}$$

where $d\boldsymbol{S}$ is an oriented area element on the surface S, whose boundary is ∂S, and

$$\boldsymbol{\Omega} = \nabla \times \boldsymbol{A}. \tag{1.9}$$

is the *Berry curvature*. The integrating function on the right hand side of Eq. (1.8) is called the *Berry flux* and its a gauge invariant quantity. For this reason, the := symbol means that the equality is valid only in those gauge choices where $\boldsymbol{A}$ is smooth on the S surface and Stokes' theorem holds; for the other gauges there may be a mismatch of $2\pi n$, with n integer.

Let us now consider S a closed surface, we can divide it into two surfaces $S = S_A \cup S_B$ separated by a closed loop Γ. We can then apply Eq. (1.8) and write

$$\begin{aligned}\int_S \boldsymbol{\Omega}\cdot d\boldsymbol{S} &= \int_{S_A} \boldsymbol{\Omega}\cdot d\boldsymbol{S_A} + \int_{S_B} \boldsymbol{\Omega}\cdot d\boldsymbol{S_B} \\ &:= \oint_\Gamma \boldsymbol{A}^A \cdot d\boldsymbol{\lambda} - \oint_\Gamma \boldsymbol{A}^B \cdot d\boldsymbol{\lambda} = 2\pi C,\end{aligned} \tag{1.10}$$

where $\boldsymbol{A}^A$ and $\boldsymbol{A}^B$ are obtained, in principle, from two different gauge choices, and C is called the *Chern number*. Eq. (1.10) is the *Chern theorem*: it states that the Berry flux over any closed 2D manifold must be a multiple of 2π and its related to the impossibility of creating a smooth gauge between the two surfaces S^A and S^B. We can now move on and apply this to crystals.

1.2.1 Anomalous quantum Hall effect and bulk-boundary correspondence

In a crystal, electrons move in a periodic potential and can be described by virtue of the Bloch theorem. In this way electrons are represented by real space periodic wavefunctions $|u_n(\boldsymbol{k})\rangle$ that are also periodic in the crystal momentum $\boldsymbol{k}$. This periodicity in the 3 directions makes the Hilbert space of the electron states a 3D torus. If we limit the analysis to only 2 spatial dimensions the Hilbert space will be a torus, which is a closed 2D manifold on which we can compute the Chern number.

The experimentally measurable quantity linked to a non-vanishing Chern number is the anomalous Hall conductivity, which predicts a transverse response to an electric field: $J_i = \sigma_{ij}\mathcal{E}_j$, where $\sigma_{ij} \neq 0$ is known as the Hall conductivity. The semiclassical equations of motions for a crystal electron in the presence of both electric and magnetic field and with a non-zero Berry curvature can be written as [142]

$$\dot{\boldsymbol{r}} = \boldsymbol{v}_g - \dot{\boldsymbol{k}} \times \boldsymbol{\Omega} \tag{1.11a}$$

$$\dot{\boldsymbol{k}} = -\frac{e}{\hbar}\boldsymbol{\mathcal{E}} - \frac{e}{\hbar c}\dot{\boldsymbol{r}} \times \boldsymbol{B} \tag{1.11b}$$

where $\boldsymbol{v}_g = \hbar^{-1}\boldsymbol{\nabla}_{\boldsymbol{k}} E_{n\boldsymbol{k}}$ is the group velocity and the $-\dot{\boldsymbol{k}} \times \boldsymbol{\Omega}$ is known as the anomalous velocity. For example, considering a 2D insulator with a single band filled, subjected to only an electric field, the contribution to the current arising from to the anomalous velocity is

$$\frac{J_y}{V_{cell}} = \frac{-e}{(2\pi)^2}\int_{BZ} \dot{y}(\boldsymbol{k})d^2k = \frac{-e}{(2\pi)^2}\int_{BZ} \dot{k}_x\Omega(\boldsymbol{k})d^2k = \frac{e^2\mathcal{E}_x}{(2\pi)^2\hbar}\int_{BZ}\Omega(\boldsymbol{k})d^2k,$$

so that, taking the derivative in $\mathcal{E}_x$, we find, for the Hall conductivity,

$$\sigma_{yx} = \frac{e^2}{(2\pi)^2\hbar}\int_{BZ}\Omega(\boldsymbol{k})d^2k = \frac{e^2}{h}C \tag{1.12}$$

where e^2/h is the conductivity quantum [1]. Note that the Hall conductivity of Eq. (1.12) is a bulk property, since we have reasoned with the Brillouin zone of an infinite sample. An insulator with a non-vanishing Chern number is known as a Chern insulator.

Let us now consider the case of a finite sample of a Chern insulator under the influence of an electric field, while not being attached to any metallic leads. If its dimensions are big enough, we expect its bulk electrons to behave as we just described and move perpendicularly to the applied field. It seems that electrons will accumulate on one edge of the sample and deplete on the other one. But this is not possible since once k_y evolves, under the influence of the electric field in Eq. (1.11b), over one full period the Hamiltonian of the system returns the same and the state of the electrons must not change. The resolution of this issue lies in the *surface states*. The excess electrons accumulating on one side of the sample must be transferred back to the opposite side. This necessitates the presence of two surface states crossing the gap: on one edge, a surface state rises in energy and depletes the accumulated electrons, while on the other edge, a surface state lowers in energy and repopulates them. The number of electrons circulating along the edges coincides with the Chern number, which also determines the number of surface states. Hence, to a non trivial bulk band structure directly corresponds the existence of edge states. This is known as the *bulk-boundary correspondence*. Materials that

---

[1] A more precise derivation, based on quantum linear response theory, of the Hall conductivity can be found in most textbooks on transport theory, for example [143]

behave in this way are known as *topological* and, depending on the spacial dimension and their symmetry properties, they are characterized by different topological invariants [10]. The Chern number of a Chern insulator is an example of topological invariant and, since it can span all the integer numbers, it is a $\mathbb{Z}$ topological invariant. Time-reversal symmetric topological insulators are another example of topological matter, described by a $\mathbb{Z}_2 = \{0, 1\}$ topological invariant. We will see in the next section that, generally, a non-trivial bulk topology is consequence of linear points of degeneracy in the energy spectrum of a system in the parameter space. When non-accidental, these degeneracy points are the effect of symmetries in the system. Hence, both the topological phase of a system and its correspondent edge states are said to be topologically protected by any perturbation that does not break these symmetries.

Some remarks on the role of symmetries in the Berry curvature are in order. These will become relevant later, when we discuss WSM and graphene. From the explicit expressions of the Berry connection and curvature in Eqs. (1.6, 1.9), applied to the Bloch modes $|u_{n\boldsymbol{k}}\rangle$, one can show that:

1. when the crystal preserves spatial inversion symmetry, then $\boldsymbol{\Omega}_n(\boldsymbol{k}) = \boldsymbol{\Omega}_n(-\boldsymbol{k})$.
2. when the crystal preserves time-reversal (TR) symmetry, then $\boldsymbol{\Omega_n}(\boldsymbol{k}) = -\boldsymbol{\Omega_n}(-\boldsymbol{k})$.
3. when the crystal preserves both symmetries above then $\boldsymbol{\Omega_n}(\boldsymbol{k}) = 0$ everywhere in the Brillouin Zone.

Of particular importance is point 2 above: if an insulating crystal has TR symmetry then every integral of the Berry curvature over the Brillouin zone will vanish and it cannot experience a non-vanishing Hall conductivity. We will see that this is the case of graphene, although it will not prevent it from having a topological phase (different from the Chern insulating one).

1.3 Conical interections: Weyl points

A conical intersection is a point of degeneracy in the energy dispersion in which the splitting of the degeneracy is linear in the distance from the touching point in any given direction in parameter space. A conical intersection between two bands is called a *WP* and in this section we will briefly explore its topological properties.

As anticipated, we confine our attention to the two-dimensional Hilbert subspace spanned solely by the two touching bands [24, 25, 29]. Within this reduced two-state space, the effective Hamiltonian takes the form:

$$H(\boldsymbol{\lambda}) = f_0(\boldsymbol{\lambda})\sigma_0 + f_x(\boldsymbol{\lambda})\sigma_x + f_y(\boldsymbol{\lambda})\sigma_y + f_z(\boldsymbol{\lambda})\sigma_z, \tag{1.13}$$

where the Pauli matrices $\{\sigma_i\}$ form a basis for the general 2×2 traceless Hermitian Hamiltonian, σ_0 is the identity matrix, and where the components f_i are smooth and real functions of the parameters $\boldsymbol{\lambda}$. The eigenvalues of this Hamiltonian are

$$E = f_0 \pm \sqrt{f_x^2 + f_y^2 + f_z^2}. \tag{1.14}$$

A degeneracy will occur only if $f_x(\boldsymbol{\lambda}) = f_y(\boldsymbol{\lambda}) = f_z(\boldsymbol{\lambda}) = 0$. Given that three conditions must be simultaneously met, we expect it to occur in a parameter space of dimension $D \geq 3$, unless there are symmetry constraints imposed on the f functions. In the last case, adjusting certain parameters of the model, like including disorder, while still respecting the symmetries of the system, will not cause the conical intersections to vanish; rather, to first order, they are merely displaced, appearing at slightly shifted locations in parameter space.

We can linearly expand the Hamiltonian of Eq. (1.13) into the vicinity of a WP, at $\boldsymbol{\lambda} = \boldsymbol{\Lambda}$, to obtain

$$H(\boldsymbol{\lambda}) = \sum_{ij} A_{ij}(\boldsymbol{\lambda}_i - \boldsymbol{\Lambda}_i)\sigma_j, \tag{1.15}$$

where $A_{ij} = \partial_i f_j$ is the Jacobian matrix evaluated at $\boldsymbol{\lambda} = \boldsymbol{\Lambda}$. We can then assign the following value to a WP

$$\chi = \operatorname{sgn}(\det A), \tag{1.16}$$

known as its *chirality*. The chirality of a WP is a topological quantity, in the sense that it will be constant even when modifying the parameters of the model, unless a singularity ($\det A = 0$) is encountered. When the matrix A is non-singular, we can diagonalize it into the form

$$H(\boldsymbol{\lambda}) = \sum_i B_i(\lambda_i - \Lambda_i)\sigma_i \equiv \boldsymbol{d}(\boldsymbol{\lambda}) \cdot \boldsymbol{\sigma}, \tag{1.17}$$

which is known as Weyl Hamiltonian. Restricting to a 3-dimensional parameter space, a surface S enclosing the WP at $\boldsymbol{\lambda} = \boldsymbol{\Lambda}$ is mapped onto the entire Bloch sphere in pseudo-spin space. It is well established [143] that an eigenstate on the Bloch sphere carries a Chern number $|C| = 1$, therefore

$$\left| \oint_S \boldsymbol{\Omega}_\pm(\boldsymbol{\lambda}) \cdot d\boldsymbol{S} \right| = 2\pi, \tag{1.18}$$

where $\boldsymbol{\Omega}_\pm(\boldsymbol{\lambda})$ is the Berry curvature, Eq. (1.9), of the upper/lower eigenstate of the Weyl Hamiltonian. Thus, WPs function as sources or sinks of a 2π quantum of Berry flux in the surrounding momentum space. By convention, a positive (negative) chirality provides the lower eigenstate with a positive (negative) Berry flux and a $C = 1$ ($C = -1$). The typical hedgehog shape of the Berry curvature around a WP is sometimes called a *skyrmion* [12], in analogy with the spin configuration in a magnetic monopole.

When at least two of the three $\boldsymbol{\lambda}$ parameters are crystal momenta, because of their periodicity, we can smoothly deform a sphere surrounding a WP into two planes on opposite sides of it, see Fig. 1.1. Each plane is a 2D Brillouin zone where each eigenband has its own Chern number. Therefore, from Eq. (1.18), and keeping into account both the chirality of the WP and the flux direction of the Berry curvature, we can write

$$\chi = C_b - C_a, \tag{1.19}$$

where C_b (C_a) is the Chern number of the lower eigenband for the upper (lower) 2D Brillouin zone. If the last parameter is also a crystal momentum, then periodicity along this direction will enforce

$$\sum_i \chi_i = 0, \tag{1.20}$$

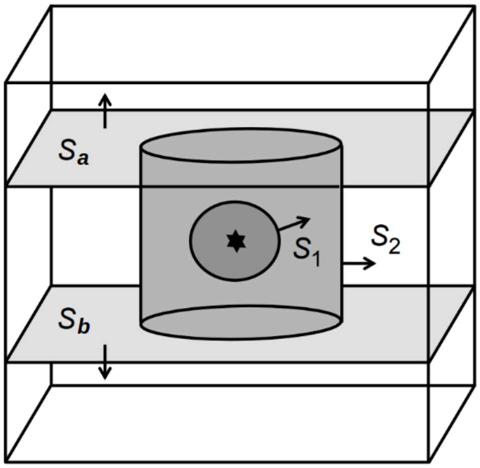

Figure 1.1: Surfaces in parameter space built around a WP (black star). First the S_1 sphere is stretched into the cylinder S_2 and then again into the two tori S_a and S_b. Figure adapted from [143].

which is known as the Nielsen-Ninomiya theorem [144].

In the next section, we will see what a WSM is and how Eq. (1.19) can shape its topology. We will also describe how it is possible to create a FWSM of tunable topology via light-irradiation of a NLSM. This will set the foundation for the first original work of this thesis, presented in Chapter 2, which concerns the study of the interface states that originate between two FWSMs.

In the following, we will introduce graphene and show how, via Eq. (1.19) the interaction with a substrate can modify its topological properties, mainly regarding its edge states. This will set the basis for the second original work of this thesis, presented in Chapter 3, which concerns the study of the SOC effects in a GJJ. For this reason, at the end of this Chapter, there will also be a brief description of superconductivity and the JJ.

1.4 Tunable Floquet-Weyl Semimetals

In this section, we will give a short pedagogical introduction to WSMs. We will also describe one of their main features which is the existence of metallic surface modes only in a finite portion of a projected 2D Brillouin zone. Because of this, WSMs host a peculiar open Fermi line on the quasi-2D surface of the material. After this we will quickly introduce a model for a NLSM and show how by shining circularly polarized light on a NLSM it is possible to induce a topological transition to a WSM, for this last part we will follow Ref. [85].

The results of this section will be the starting point for the work done in Chapter 2 on the analysis of the interface states that originates between two regions of a NLSM illuminated with light beams of opposite circular polarization.

1.4.1 Weyl semimetals

When $\boldsymbol{\lambda} = \boldsymbol{k}$ is the 3D momentum space, we have a 3D crystal with WPs that is known as a WSM [8,17,32,33]. As we have discussed in the previous section, due to the general repulsion between energy levels, in order to host a non-accidental degeneracy, a WSM needs to have a protecting symmetry. Because of this, a WSM is generally time-reversal symmetric with broken inversion symmetry or inversion symmetric with broken time-reversal symmetry [8]. Most importantly, it cannot have both symmetries otherwise the Berry curvature of any state would be vanishing, as we saw previously at the end of section 1.2.1. Either one of these symmetries protects the existence of WPs in the crystal, meaning that disorder that does not break the degeneracy and can only shift the position of a WP [10, 145]. If a WSM has either TR or I symmetry we can say more about the population of the WPs. In these cases the energy spectrum is symmetric and any WP at $\boldsymbol{K}$ has a symmetric one at $-\boldsymbol{K}$. Given what we said in section 1.2.1 about the symmetry aspects of the Berry curvature, we can write

$$\begin{array}{ll} \chi(\boldsymbol{K}) = -\chi(-\boldsymbol{K}), & \text{I symmetry} \\ \chi(\boldsymbol{K}) = \chi(-\boldsymbol{K}), & \text{TR symmetry} \end{array}. \tag{1.21}$$

Thus, if a WSM possesses I symmetry, a WP at $\boldsymbol{K}$ is paired by a WP of opposite chirality at $-\boldsymbol{K}$ with the same energy, fulfilling the Nielsen-Ninomiya theorem with a minimal set of WPs. Conversely, if only TR symmetry is present, the paired WPs share the same chirality, and the Nielsen-Ninomiya theorem then requires at least one additional pair of WPs with opposite chirality.

A simple Hamiltonian describing an I-symmetric WSM with a minimal set of WPs is [8]

$$H(\boldsymbol{k}) = \left[m - B\left(k_x^2 + k_y^2 + k_z^2\right)\right]\sigma_x + v_y k_y \sigma_y + v_z k_z \sigma_z, \tag{1.22}$$

with $mB > 0$ and $\mathcal{P}H(\boldsymbol{k})\mathcal{P}^\dagger = H(-\boldsymbol{k})$, with $\mathcal{P} = i\sigma_x$ the I symmetry operator. Note that this is very close to the Dirac Hamiltonian with quadratic correction that we have discussed in Sec. 1.1. The eigenenergies of the Hamiltonian (1.22) are

$$E_\pm(\boldsymbol{k}) = \pm\sqrt{\left[m - B\left(k_x^2 + k_y^2 + k_z^2\right)\right]^2 + \left(v_y k_y\right)^2 + \left(v_z k_z\right)^2}, \tag{1.23}$$

which are degenerate only at two WPs placed at $\boldsymbol{K}_\pm = \left(\pm\sqrt{m/B}, 0, 0\right)$. Linearizing the Hamiltonian expressed in Eq. (1.22) around the WPs and using the definition of Eq. (1.16) their chirality is found as $\chi_\pm = \mp 1$.

One of the most striking consequences of the presence of WPs is the existence of open Fermi lines on the surface of the material, known as Fermi arcs [8, 17, 38]. This is a consequence of the bulk-boundary correspondence we described earlier. Because of Eq. (1.19), every 2D projection of the Brillouin zone that falls between the WPs has a non-trivial Chern number for its valence and conductance bands. In the case of the Hamiltonian of Eq. (1.22), every (k_y, k_z) Brillouin zone for a fixed $\tilde{k}_x \in]\boldsymbol{K}_-, \boldsymbol{K}_+[$ has a Chern number $C(k_x) = 1$ for its valence band. As such, it can be regarded as an effective 2D Chern insulator [37], which is required to host a metallic edge mode (that cross the Fermi energy, $E = 0$) due to the bulk boundary correspondence. If we cut the sample, say in the z direction, for every $\tilde{k}_x$ between the surface projection of the two WP we find that the edge mode intersects the Fermi energy, $E = 0$, at a specific k_y. Linking all the $(\tilde{k}_x, k_y)$ couples so created, a line, known as Fermi arc, develops, which connects the two projections of the WPs [8]. Outside of these there

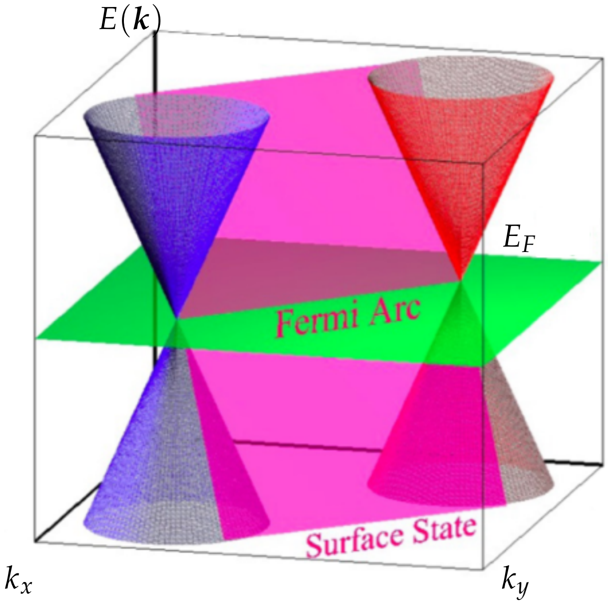

Figure 1.2: Example of energy dispersion in a WSM characterized by two WPs of opposite chiralities. In blue an red the energy dispersion originating from the WPs of opposite chiralities, in fuchsia the surface states dispersion which crosses the Fermi level, in green, generating a Fermi arc. Figure adapted from [33].

can be no Fermi line because the slices are not topological (they have zero Chern number) and do not host metallic edge modes. An example of Fermi arc is shown in Fig. 1.2. The fact that the Fermi arcs originate and end at the surface projections of WPs with different chiralities is a general feature, and its consistency is ensured by the Nielsen-Ninomiya theorem. The Fermi arcs are an example of an anomaly in the surface band structure. In fact, an open Fermi line could never exist in an isolated 2D system or even at the surface of a 3D topological insulator.

The existence of Fermi arcs has been experimentally proven via ARPES techniques in different materials [33–36, 146–152]. The presence of the WPs in a WSM also has two peculiar transport consequence. The first one, tightly connected to the Fermi arcs, is the anomalous Hall effect [8, 153, 154]. We saw that every 2D plane in momentum space that falls between the WPs acts as a Chern insulator; as such, every plane contributes with a e^2/h of Hall conductivity, from Eq. (1.12), to produce a non-quantizied Hall response from the whole WSM of $|\sigma_{ab}| = e^2/(2\pi h)k_c$, where k_c is the distance between the projected WPs in the direction perpendicular to the *ab* plane. The second one is a negative longitudinal magnetoresistance linked to an imbalance of charge at the two WPs in the presence of parallel electric and magnetic field [8, 17, 154].

1.4.2 Nodal Line Semimetals

Another class of topological materials closely related to WSMs is the NLSM. Unlike the zero-dimensional band touchings in a WSM (the WPs), a NLSM features band touchings that form a one-dimensional manifold, with linear dispersion in all directions perpendicular to the degenerate line. Depending on the symmetries of the system, there may be one nodal-line [9, 17, 22–30, 155, 156] or multiple with different connectivity structures [100, 157–161]. Materials that present a nodal line of degeneracies show peculiar surface and bulk properties, but we will not delve into it. A review on the topic can be found in [17]. For the rest of this thesis, we only need a minimal theoretical model to describe a NLSM.

One of the simplest effective models for a NLSM, very akin to that of a WSM in Eq. (1.22) (and still based on a variant of the Dirac Hamiltonian), is the following [9]

$$H(\boldsymbol{k}) = \left[m - B(k_x^2 + k_y^2 + k_z^2)\right]\sigma_x + v k_z \sigma_z, \tag{1.24}$$

with $mB > 0$. This Hamiltonian is symmetric with respect to the $\mathcal{M} = i\sigma_x$ z-mirror operator, so that $\mathcal{M}H(\boldsymbol{k})\mathcal{M}^\dagger = H(k_x, k_y, -k_z)$, which enforces a vanishing σ_y component and allows for a line of degeneracy from the effective Hamiltonian of Eq. (1.13). Its eigenenergies are

$$E_{\pm,\boldsymbol{k}} = \pm\sqrt{\left[m - Bk^2\right]^2 + v^2 k_z^2} \tag{1.25}$$

which creaste a line of degeneracy on the nodal ring defined by $k_z = 0$ and $k_x^2 + k_y^2 = m/B$. As we said before, this line of degeneracy is protected against all perturbations that conserve the z-mirror symmetry of the system.

1.4.3 Floquet-Weyl Semimetal via light irradiation

In this section, we show how, in a semiclassical treatment of the electromagnetic field, a beam of circularly polarized light can induce a transition from a NLSM to a FWSM. This section closely follows the results of Ref. [85].

Let us consider a beam of circularly polarized light that moves in the x direction, described by the vector potential

$$\boldsymbol{A}(t) = A_0\left[0, \cos\left(\omega t\right), \sin\left(\omega t + \phi\right)\right]. \tag{1.26}$$

We shine this beam of light on a NLSM described by the Hamiltonian of Eq. (1.24). Since the vector potential $\boldsymbol{A}(t)$ does not depend on spatial coordinates, it does not break the crystal translational invariance. Under the minimal coupling prescription, Eq. (1.24) becomes

$$\begin{aligned} H(\boldsymbol{k} + e\boldsymbol{A}(t)) = \{&m - B[k^2 + e^2A_0^2(\cos^2\left(\omega t\right) + \sin^2\left(\omega t + \phi\right)) + \\ &+ 2eA_0(\cos\left(\omega t\right)k_y + \sin\left(\omega t + \phi\right)k_z)]\}\sigma_x + \\ &+ v[k_z + eA_0\sin\left(\omega t + \phi\right)]\sigma_z. \end{aligned} \tag{1.27}$$

where $k^2 = k_x^2 + k_y^2 + k_z^2$. This Hamiltonian is time periodic and can be expanded in Fourier modes as $H(t, \boldsymbol{k}) = \sum_n H_n(\boldsymbol{k})e^{in\omega t}$ with $H_n(\boldsymbol{k}) = \dfrac{1}{T}\int_{-\frac{T}{2}}^{\frac{T}{2}} H(t, \boldsymbol{k})e^{-in\omega t}dt$ and $T = 2\pi/\omega$. The Fourier coefficients are easily computed as

$$\begin{aligned} H_0(\boldsymbol{k}) &= \left[m - Be^2A_0^2 - Bk^2\right]\sigma_x + vk_z\sigma_z, \\ H_{\pm1}(\boldsymbol{k}) &= -eA_0\left[2B\left(k_y \mp ie^{\pm i\phi}k_z\right)\sigma_x \pm ie^{\pm i\phi}v\sigma_z\right]/2, \\ H_{\pm2}(\boldsymbol{k}) &= -Be^2A_0^2\left(1 - e^{\pm i2\phi}\right)\sigma_x/4, \end{aligned} \tag{1.28}$$

and $H_n(\boldsymbol{k}) = 0$ for all $|n| > 2$. Applying Floquet degenerate perturbation theory, it can be demonstrated [162] that, in the high driving frequency regime, the system dynamics can be effectively approximated by a time-independent Hamiltonian, which takes the form

$$H_{eff}(\boldsymbol{k}) = H_0(\boldsymbol{k}) + \sum_{n\geq1}\frac{[H_{+n}(\boldsymbol{k}), H_{-n}(\boldsymbol{k})]}{n\omega} + \mathcal{O}\left(\frac{1}{\omega^2}\right). \tag{1.29}$$

The only commutator appearing in Eq. (1.29) that is different from zero is $[H_{+1}(\boldsymbol{k}), H_{-1}(\boldsymbol{k})]$. Using the Pauli matrix commutation relation $[\sigma_a, \sigma_b] = 2i\epsilon_{abc}\sigma_c$ it can be readily computed as

$$\begin{aligned}
[H_{+1}(\boldsymbol{k}), H_{-1}(\boldsymbol{k})] = \Big[&- eA_0 \left[2B\left(k_y - ie^{i\phi}k_z\right)\sigma_x + ie^{+i\phi}v\sigma_z\right]/2, \\
&- eA_0 \left[2B\left(k_y + ie^{-i\phi}k_z\right)\sigma_x - ie^{-i\phi}v\sigma_z\right]/2\Big] \\
&= \frac{e^2A_0^2}{4}\Big\{\Big[2B(k_y - ie^{i\phi}k_z)\sigma_x \ , \ -ie^{-i\phi}v\sigma_z\Big] + \\
&+ \Big[ie^{i\phi}v\sigma_z \ , \ 2B(k_y + ie^{-i\phi}k_z)\sigma_x\Big]\Big\} \\
&= e^2A_0^2Bv\Big[(ik_z - e^{-i\phi}k_y) - (e^{i\phi}k_y + ik_z)\Big]\sigma_y \\
&= -2e^2A_0^2Bv\cos(\phi)k_y\sigma_y \equiv \lambda\omega k_y\sigma_y. \qquad (1.30)
\end{aligned}$$

Putting together Eqs. (1.28-1.30), the final expression for the effective Hamiltonian is

$$H_{eff}(\boldsymbol{k}) = \left[\tilde{m} - Bk^2\right]\sigma_x + \lambda k_y\sigma_y + vk_z\sigma_z + \mathcal{O}(1/\omega^2) \qquad (1.31)$$

where

$$\lambda = -2e^2BvA_0^2\cos(\phi)/\omega, \qquad (1.32a)$$

$$\tilde{m} = m - Be^2A_0^2. \qquad (1.32b)$$

The main effect of the driving is to add a σ_y component to the NLSM Hamiltonian of Eq. (1.24) which now breaks the z-mirror symmetry. Therefore, we expect the 1D line of degeneracy to be lifted into a 0D one. Indeed, the eigenenergies of Eq. (1.31) are

$$\tilde{E}_{\pm,\boldsymbol{k}} = \pm\sqrt{[\tilde{m} - Bk^2]^2 + \lambda^2k_y^2 + v^2k_z^2} \qquad (1.33)$$

and they intersect at the isolated WPs $\boldsymbol{K}\pm = \pm(\sqrt{\tilde{m}/B}, 0, 0)$. Therefore, for $\lambda \neq 0$, the system will transition into a WSM phase. Due to the periodic driving by light, this phase is referred to as a FWSM. Additionally, the σ_y component introduces an imaginary part to the effective Hamiltonian, making it impossible to define a time-reversal operator Θ such that

$\Theta H(\boldsymbol{k})\Theta^{-1} = H(-\boldsymbol{k})$. This was expected, as the presence of circularly polarized light breaks time-reversal symmetry, and, as discussed after Eqs.(1.21), it allows for a FWSM with a minimal set of WPs. Indeed, the effective Hamiltonian (1.31) can be expanded near the gapless points as $H\pm(\boldsymbol{q}) = \sum_{ji} v_{ij} q_{\pm,j}\sigma_i$, where $v_{ij} = \partial_j f_i$ and $q_{\pm,j} = \boldsymbol{k} - \boldsymbol{K}_{\pm}$. We then get

$$v_{11} = \mp 2\sqrt{\tilde{m}B}, \quad v_{22} = \lambda, \quad v_{33} = v \tag{1.34}$$

and $v_{ij} = 0$ for $i \neq j$. In this way, we see that the two WPs possess opposite chirality, in agreement with the Nielsen-Ninomiya theorem, with their handedness determined by that of the incident circularly polarized light, as

$$\chi_{\pm} = \operatorname{sgn}\left[\det\left(v_{ij}\right)\right] = \pm\operatorname{sgn}\left(\cos\phi\right). \tag{1.35}$$

Moreover, the locations of the WPs can be tuned by changing the intensity of the incident light beam, see Eq. (1.32b), and by changing its directions. For example, the WPs would be at $\pm(0, \sqrt{\tilde{m}/B}, 0)$ for a light beam moving towards the y-direction.

More in general, the concept of Floquet engineering, which means tuning the properties of a system via a periodic drive, has gained much interest in the recent literature [57, 59, 64, 70, 72, 91]. In particular, this concept was theoretically applied to topological systems with the results of inducing topological phase transitions [55, 60, 69, 81–83, 85, 88], as we have just shown, or crating anomalous topological states with no static counterpart [61,74]. In the latter case even a new topological classification for these non-equilibrium states was necessary [56,71,75–77,79,80].

The conclusions of this section are the starting point for the original results shown in Chapter 2, where we study the electronic surface states that form at the interface between two half-spaces of a NLSM irradiated by two monochromatic light beams with opposite circular polarization.

1.5 Topology of graphene on a substrate

In this section, we give a pedagogical introduction to graphene and to how its properties can be modified by the interaction with a substrate.

We will start by introducing the crystal structure of intrinsic graphene and compute its band structure via a tight-binding procedure. From the tight-binding model we move to its low energy description via the continuum model. This model is based on the Dirac Hamiltonian found by expanding the band structure around the two non-equivalent Dirac points. This is where we will make contact with the previous sections on conical intersection. We will then review some topological properties that arise because of the Dirac points description, already in intrinsic graphene. Finally, we introduce the effects of a substrate, reviewing some of the recent literature on the topic.

This section will set the basis for the results of Chapter 3. In particular, the continuum model of graphene on a substrate is used to study the effects of Spin-Orbit coupling in a GJJ.

1.5.1 Crystal structure and tight-binding model

Graphene is a two-dimensional layer of carbon atoms arranged in a honeycomb pattern [163], see Fig. 1.3. Its atoms are connected by strong covalent bonds that originate from the planar hybridization of sp^2 orbitals, guaranteeing its robust structural form. The sp^2 orbitals form bonds so strong that they can be completely neglected when considering the electronic properties close to the Fermi energy. Instead, these are defined by the remaining p_z orbitals which loosely connect to other graphene layers via van der Waals forces, making it possible to isolate a single graphene sheet. As we will see shortly, the interaction between p_z orbitals in the peculiar honeycomb arrangement will give rise to an electron gas of massless relativistic-like particles [164].

The honeycomb structure is not a Bravais lattice, so it is instead represented as a triangular lattice with two atoms per unit cell. The two triangular sublattices that originates are generally called A and B, and together they make degree of freedom that creates the graphene two-band structure (when neglecting spin). Moreover they provide graphene with a chiral symmetry that will allow it to have a topological classification [10,165]. The two lattice vectors for each sublattice and the positions of the atoms in the unit cell are

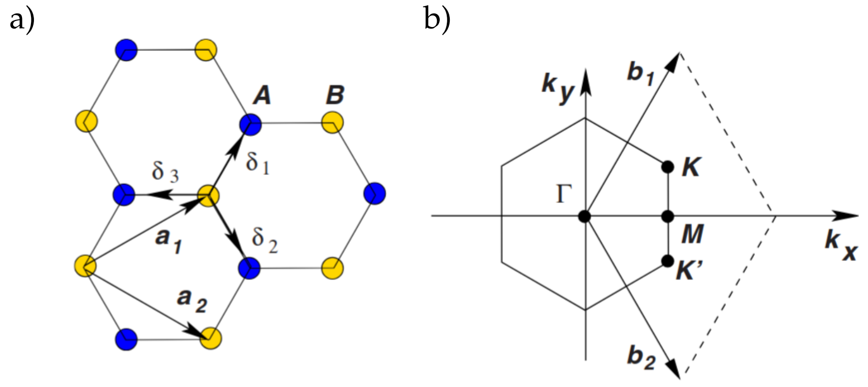

Figure 1.3: Crystal structure of graphene. (a) honeycomb lattice composed of two triangular sublattices A and B; $\boldsymbol{a}_i$ are the real space lattice vectors and $\boldsymbol{\delta}_i$ the vectors connecting nearest-neighboring atoms. (b) reciprocal lattice; $\boldsymbol{b}_i$ are the reciprocal lattice vectors, Γ and $\boldsymbol{M}$ high symmetry points (time-reversal invariant momenta) and $\boldsymbol{K}$ and $\boldsymbol{K}'$ the two non equivalent Dirac points. Figure adapted from [164].

$$\begin{aligned} \boldsymbol{a}_1 &= \frac{a}{2}\left(\sqrt{3}, 1\right) & \qquad \boldsymbol{d}_1 &= (0,0) \\ \boldsymbol{a}_2 &= \frac{a}{2}\left(\sqrt{3}, -1\right) & \qquad \boldsymbol{d}_2 &= a\left(-\frac{1}{\sqrt{3}}, 0\right) \end{aligned} \tag{1.36}$$

where $a \approx 2.46$ Å is the lattice constant of graphene; and the vectors connecting nearest-neighboring atoms are

$$\boldsymbol{\delta}_1 = \frac{a}{2}\left(\frac{1}{\sqrt{3}}, 1\right) \tag{1.37}$$

$$\boldsymbol{\delta}_2 = \frac{a}{2}\left(\frac{1}{\sqrt{3}}, -1\right) \tag{1.38}$$

$$\boldsymbol{\delta}_3 = a\left(-\frac{1}{\sqrt{3}}, 0\right), \tag{1.39}$$

with $|\boldsymbol{\delta}_i| \approx 1.42$ Å. Using the orthogonality relations $\boldsymbol{a}_i \cdot \boldsymbol{b}_j = 2\pi\delta_{ij}$ the reciprocal lattice primitive vectors are found as

$$\boldsymbol{b}_1 = \frac{2\pi}{a}\left(\frac{1}{\sqrt{3}}, 1\right) \tag{1.40}$$

$$\boldsymbol{b}_2 = \frac{2\pi}{a}\left(\frac{1}{\sqrt{3}}, 1\right). \tag{1.41}$$

The graphene Hamiltonian can be written in a tight-binding form as (neglecting for now the spin degree of freedom)

$$H = -t\sum_{\langle ij \rangle}(c^{\dagger}_{iA}c_{jB} + h.c.) \tag{1.42}$$

where $c^{\dagger}_{i\alpha}$ ($c_{i\alpha}$) creates (annichilates) an electron on the i-th cell on sublattice α; $t \approx 2.8$ eV is the hopping parameter, due to the overlap of p_z orbitals, between nearest-neighboring cells $\langle ij \rangle$ (avoid double counting). Clearly, as one would expect, if there are no sublattice dependent interaction the graphene layer is symmetric for the exchange of the two sublattices, $A \leftrightarrow B$; this symmetry is also known as the chiral symmetry. Fourier transforming the $c_{i\alpha}$ operators based on their position $\boldsymbol{R}_{i\alpha}$ on the real-space lattice $c_{i\alpha} = \sum_{\boldsymbol{k}} e^{i\boldsymbol{R}_{i\alpha}} c_{\boldsymbol{k}\alpha}$ and substituting in Eq. (1.42) one obtains

$$H = \sum_{k} \begin{bmatrix} c^{\dagger}_{iA} \\ c^{\dagger}_{iB} \end{bmatrix} H(\boldsymbol{k}) \begin{bmatrix} c_{iA} & c_{iB}, \end{bmatrix} \tag{1.43a}$$

$$H(\boldsymbol{k}) = \begin{bmatrix} 0 & -t\sum_{\boldsymbol{a}_i} e^{i\boldsymbol{k}\cdot\boldsymbol{a}_i} \\ -t\sum_{\boldsymbol{a}_i} e^{-i\boldsymbol{k}\cdot\boldsymbol{a}_i} & 0 \end{bmatrix} \tag{1.43b}$$

where $\boldsymbol{a}_i$ runs over the lattice vectors of Eq. (1.36) plus the null vector. The eigenenergies of $H(\boldsymbol{k})$ are

$$E(\boldsymbol{k}) = \pm\sqrt{3 + 2\cos(k_x a) + 4\cos(k_x a/2)\cos(\sqrt{3}k_y a/2)}, \tag{1.44}$$

where the sign ± indicates to the conduction or valence band. $E(\boldsymbol{k})$ of Eq. (1.44) has two non equivalent points of degeneracy at

$$\boldsymbol{K} = \frac{2\pi}{a}\left(\frac{1}{\sqrt{3}}, \frac{1}{3}\right) \tag{1.45a}$$

$$\boldsymbol{K}' = \frac{2\pi}{a}\left(\frac{1}{\sqrt{3}}, -\frac{1}{3}\right). \tag{1.45b}$$

They are known as Dirac points because the energy dispersion is linear in their vicinity, as we will see in the next section by expanding the Hamiltonian of Eq. (1.43b) to linear order in the momenta.

1.5.2 Continuum model and Dirac Hamiltonian

To find a low-energy model for (spinless) graphene the Hamiltonian of Eq. (1.43b) can be lineraly expanded around the Dirac points (1.45) to find [164]

$$H_{\boldsymbol{K}} = \hbar v_F \boldsymbol{\sigma} \cdot \boldsymbol{p} \tag{1.46a}$$

$$H_{\boldsymbol{K}'} = \hbar v_F \boldsymbol{\sigma}^* \cdot \boldsymbol{p} \tag{1.46b}$$

where $\hbar v_F = (\sqrt{3}/2)at$, $\boldsymbol{p} = \boldsymbol{k} - \boldsymbol{K}^{(')}$ and $\boldsymbol{\sigma} = (\sigma_x, \sigma_y)$ is the Pauli operator describing the pseudospin (because of the spinorial form) degree of freedom of the sublattices A, B. These are the two Dirac Hamiltonians that describe the low-energy, massless relativistic excitations of graphene. Each of the Hamiltonians of Eq. (1.46) is the equivalent of the Weyl Hamiltonian that we have see previously in Sec. 1.3 and 1.4.1, but in two dimensions. $\boldsymbol{K}$ and $\boldsymbol{K}'$ can be effectively regarded as another degree of freedom of graphene and are often called valleys, leading to the following compact form of Eq. (1.46)

$$H_\tau(\boldsymbol{p}) = \hbar v_F (\sigma_x p_x + \tau \sigma_y p_y) \tag{1.47}$$

where $\tau = \pm$ describes the valley degree of freedom. Note that the Hamiltonian (1.47) is time-reversal and inversion symmetric and satisfies the following relations

$$\sigma_x H_\tau(\boldsymbol{p}) \sigma_x = H_{-\tau}(\boldsymbol{p}) \tag{1.48a}$$

$$\mathcal{T} H_\tau(\boldsymbol{p}) \mathcal{T}^\dagger = H_{-\tau}(-\boldsymbol{p}) \tag{1.48b}$$

$$\mathcal{P} H_\tau(\boldsymbol{p}) \mathcal{P}^\dagger = H_{-\tau}(-\boldsymbol{p}) \tag{1.48c}$$

with $\mathcal{T} = \sigma_z \mathcal{K}$ the time-reversal symmetry operator, $\mathcal{K}$ being the operator that performs complex conjugation, and with $\mathcal{P} = \sigma_y$ the inversion symmetry operator. The eigenstates of Eq. (1.47) are

$$\psi_\tau(\boldsymbol{p}) = \frac{1}{\sqrt{2}} \begin{pmatrix} 1 \\ \xi e^{i\tau\theta_k} \end{pmatrix} \tag{1.49}$$

corresponding to the eigenvalues $E(\boldsymbol{p}) = \xi\hbar v_F|\boldsymbol{p}|$, with $\xi = \pm$, and $\theta_{\boldsymbol{k}} = \arctan(p_x/p_y)$. The massless Dirac Hamiltonians (1.47) commute with the following valley defined operator[2]

$$h_+ = \frac{1}{2}\boldsymbol{\sigma}\cdot\frac{\boldsymbol{p}}{|\boldsymbol{p}|} \qquad h_- = \sigma_x h_+ \sigma_x \tag{1.50}$$

known as the *chirality* operator. The chirality operator defines the alignment between momentum $\boldsymbol{p}$ and pseudospin $\boldsymbol{\sigma}$ in a given state and it is closely related to the chiral symmetry of graphene, $\mathcal{C} = \sigma_z$, which switches the chirality of any state, $\mathcal{C}h_\tau\mathcal{C}^\dagger = -h_\tau$. The eigenstates (1.49) have a defined chirality, which is opposite for the ones of the upper and lower eigenvalues and opposite at the two Dirac points

$$h\psi_\pm(\boldsymbol{p}) = \mp\xi\frac{1}{2}\psi_\pm(\boldsymbol{p}). \tag{1.51}$$

We can say that the Dirac points are chiral and have opposite chirality. One of the most striking consequences of the chirality of graphene electrons is that a backscattering process happening at normal incidence, $\theta_{\boldsymbol{k}=0}$ must flip the sign of the pseudospin. So in the absence of any sublattice breaking interaction, the pseudospin will be conserved wich leads to perfect transmission, a phenomenon known as Klein tunneling [166].

The well-defined chirality of the excitations near a Dirac point is closely related to a topological invariant known as the winding number. The winding number, ν, is analogous of the Chern number we saw in Sec. 1.2 for 1D closed loops. It can be defined from the eigenstates of the Hamiltonian as [167] (that we will use in Chapter 2)

$$\nu\left(\Gamma\right) = \frac{1}{2\pi}\int_\Gamma \left(\langle\boldsymbol{\sigma}\rangle_{\boldsymbol{p}}(t) \times \frac{d}{dt}\langle\boldsymbol{\sigma}\rangle_{\boldsymbol{p}}(t)\right)_z dt, \tag{1.52}$$

where $\langle\boldsymbol{\sigma}\rangle_{\boldsymbol{p}}(t) = \langle\psi(\boldsymbol{p}(t))|\boldsymbol{\sigma}|\psi(\boldsymbol{p}(t))\rangle$ is the average pseudospin for an eigenstate (1.49) at the point t along the path Γ in momentum space; or equivalently, it can be defined from the Hamiltonian (1.47) itself [165]

$$\nu(\Gamma) = \frac{i}{2\pi}\int_\Gamma \mathrm{Tr}[h^{-1}(\boldsymbol{p})\partial_{\boldsymbol{p}}h(\boldsymbol{p})]\cdot d\boldsymbol{p}, \tag{1.53}$$

---

[2] There are other basis choices, for example the switch of the $A \leftrightarrow B$ sublattice wavefunctions on the $\boldsymbol{K}'$ valley, which simplify the expression of the chirality operator.

where $h(\boldsymbol{p}) = \hbar v_F(p_x - i\tau p_y)$ is the upper right block of the Hamiltonian (1.47); in both definitions Γ is a path in momentum space that encloses the origin, i.e. the Dirac point.

Applying the definitions above to the Hamiltonian (1.47) one finds that the Dirac points have opposite winding number $\nu(\boldsymbol{K}) = -\nu(\boldsymbol{K}') = 1$. Because of the non-vanishing winding number, each eigenstate acquires a non-trivial Berry phase (1.7) when computed in a path that encloses a Dirac point

$$\gamma(\Gamma) = i \int_\Gamma \langle \psi_\tau(\boldsymbol{p}) | \nabla_{\boldsymbol{p}} \psi_\tau(\boldsymbol{p}) \rangle \cdot d\boldsymbol{p} = \pi \text{ (mod } 2\pi). \tag{1.54}$$

At this point, one can apply the same reasoning done in section 1.3 and say that, because of the periodicity of the Brillouin zone, each Dirac point has the effect of changing the Berry phase (at this point a Zak phase) of a 1D Brilluoin zone projection that crosses it; and, similarly, that the total winding number of the Dirac points in a 2D crystal must vanish (Nielsen-Ninomiya theorem) [165, 168]. In this way, intrinsic graphene behaves in 2D like a 3D WSM, and, similarly (see Sec. 1.4), hosts edge states for all those boundaries that allow to have a well-defined momentum $\boldsymbol{p}$ between the Dirac points [142, 145, 169–172]. Graphene has two main boundaries: the zigzag one, which makes a ribbon periodic along the $\boldsymbol{a}_1$ direction in Fig. 1.3a (or anyone rotated by $\pi/3$ from it); and the armchair one that is found rotating a zigzag edge by $\pi/6$. The armchair edge creates short range scattering and forces boundary conditions that do not preserve the graphene valley degree of freedom [169, 173, 174]; as such, it is the only edge that does not host edge modes in intrinsic graphene. All the other ones may host edge modes, depending on the width of the ribbon [171, 174–176]. This can also be seen explicitly from Fig. 1.3b where creating a zigzag edge means projecting the 2D Brillouin zone on the k_y axis, thus preserving the valleys, while creating an armchair edge means projecting on the k_x axis, superimposing the valleys. In intrinsic graphene, these edge modes have zero energy and are dispersionless [169], therefore they do not affect the transport properties of graphene.

In the next section, we explore how these proximity effects with a substrate can modify the topological properties of graphene. In particular, how the graphene phase and the dispersion and robustness of the edge modes are affected.

1.5.3 Graphene with proximity induced Spin-Orbit Coupling

In this section, we explore the effects on a graphene layer, especially on its low energy description, of the interaction with a substrate. When placing two materials in close proximity, their wavefunctions overlap and hybridize at the interface. This can lead to some properties of one material being transferred to the boundary layers of the other, decaying exponentially into the bulk. This is known as the *proximity effect* [177–181]. By its nature, the proximity effect is stronger in atomically thin materials interacting via van der Waal forces [182], allowing for a new way of material designing. Graphene, in particular, is emerging as a promising platform in proximity designed setups [139]. This is due to the strong proximity induced SOC it can acquire [133, 137, 138, 183–186] that may lead to promising spintronics applications [134, 135, 187–190].

From a symmetry breaking point of view, graphene on a substrate changes its point group symmetry class from D_{6h} to C_{3v}. Because of this reduction in symmetry the graphene layer may acquire new SOC terms. In a tight-binding description the most general graphene Hamiltonian with SOC can be expressed as [191]

$$\begin{aligned}\mathcal{H} = &-t \sum_{\langle i,j\rangle,s} c^{\dagger}_{is} c_{js} + \sum_{i,s} \left(U_z \eta_i - \mu\right) c^{\dagger}_{is} c_{is} + \frac{2i\lambda_{\mathrm{R}}}{3} \sum_{\langle i,j\rangle,s,s'} \left[\left(\hat{\boldsymbol{s}} \times \boldsymbol{d}_{ij}\right)_z\right]_{ss'} c^{\dagger}_{is} c_{js'} \\ &+ \frac{i}{3\sqrt{3}} \sum_{\langle\langle i,j\rangle\rangle,s,s'} \lambda^{i}_{\mathrm{I}} \nu_{ij} \left[\hat{\boldsymbol{s}}_z\right]_{ss'} c^{\dagger}_{is} c_{js'} + \frac{2}{3} \sum_{\langle\langle i,j\rangle\rangle,s\neq s'} \lambda^{i}_{\mathrm{PIA}} \left[i\hat{\boldsymbol{s}} \times \boldsymbol{d}_{ij}\right]_{ss'} c^{\dagger}_{is} c_{js'},\end{aligned} \tag{1.55}$$

where i is a composite index characterizing both the position of an atom and its sublattice A or B; U_z is a staggered sublattice dependent potential and λ_{R} is a R-SOC originating from the breaking of the horizontal $z \to -z$ inversion symmetry. $\lambda^{i}_{\mathrm{I}} = \{\lambda^{A}_{\mathrm{I}}, \lambda^{B}_{\mathrm{I}}\}$ is the next-nearest neighbor intrinsic SOC and, in general, it can differ for the two sublattices; it is spin conserving and depend on the clockwise ($\nu_{ij} = +$) or counterclockwise ($\nu_{ij} = -$) path connecting site j to site i along the hexagonal lattice.

$\lambda^i_{\mathrm{PIA}} = \{\lambda^A_{\mathrm{PIA}}, \lambda^B_{\mathrm{PIA}}\}$ is a sublattice dependent, spin flipping, next-nearest neighbor hopping also originating from the horizontal symmetry breaking. Since the main effects of the latter on the graphene band structure happen far from the Dirac points [192], it will not be treated in the present work. By Fourier transforming and expanding near the Dirac points, as we did before, the Hamiltonian can be written in its the low-energy form as [131,135,193,194]

$$\begin{aligned}\mathcal{H} = \hbar v \left[\sigma_x p_x + \tau_z \sigma_y p_y\right] - (\mu_0 - s_z \tau_z \lambda_{\mathrm{VZ}}) \\ + (U_z + s_z \tau_z \lambda_{\mathrm{KM}})\sigma_z + \lambda_{\mathrm{R}} \left(s_y \sigma_x - \tau_z s_x \sigma_y\right),\end{aligned} \tag{1.56}$$

which acts on an 8-dimensional spinorial space in which $\boldsymbol{\sigma}$, $\boldsymbol{\tau}$ and $\boldsymbol{s}$ are the three Pauli matrices that describe the sublattice (A, B), valley $(\boldsymbol{K}, -\boldsymbol{K})$ and spin z projection $(\uparrow, \downarrow)$ degrees of freedom, respectively; moreover, $\lambda_{\mathrm{KM}} = (\lambda^A_{\mathrm{I}} + \lambda^B_{\mathrm{I}})/2$ is known as KM-SOC and $\lambda_{\mathrm{VZ}} = (\lambda^A_{\mathrm{I}} - \lambda^B_{\mathrm{I}})/2$ as VZ-SOC. All of the above substrate induced terms preserve graphene time-reversal symmetry, Eq. (1.48b), but only λ_{KM} preserves its inversion symmetry, Eq. (1.48c)[3]. Moreover, λ_{R} is the only term that does not preserve the spin projection s_z. For this reason we begin analyzing Eq. (1.56) without the R-SOC term, so that s_z is still a good quantum number.

Let us start by considering U_z. It arises from an asymmetric interaction of the two sublattices with the substrate [195, 196]. For this reason it breaks graphene chiral symmetry and, because it completes the form of a Dirac equation in 2D, is generally known as the *mass* term. Hence, U_z changes the topology of the graphene layer. The graphene eigenenergy becomes $E(\boldsymbol{p}) = \sqrt{(\hbar v \boldsymbol{p})^2 + U_z^2}$ so that a $2|U_z|$ gap opens on both valleys. The fact that the Dirac degeneracy is lifted allows for the computation of the Chern number from Eq. (1.10). The Berry curvature can be computed as [129,197]

$$\Omega_z(\boldsymbol{p}) = \xi \tau \frac{U_z (\hbar v)^2}{2\left[U_z^2 + (\hbar v |\boldsymbol{p}|)^2\right]^{3/2}}, \tag{1.57}$$

so that for each band, $\xi = \pm$, Ω_z is extremely peaked around the Dirac points and is exactly opposite on the two valleys, $\tau = \pm$, a plot of the Berry curvature can be seen in Fig. 1.4 [129]. Hence, the total Chern

---

[3] Including spin and valley degrees of freedom the time-reversal symmetry operator becomes $\mathcal{T} = i s_y \tau_x \sigma_z \mathcal{K}$, and the inversion one $\mathcal{P} = i \tau_x \sigma_y$.

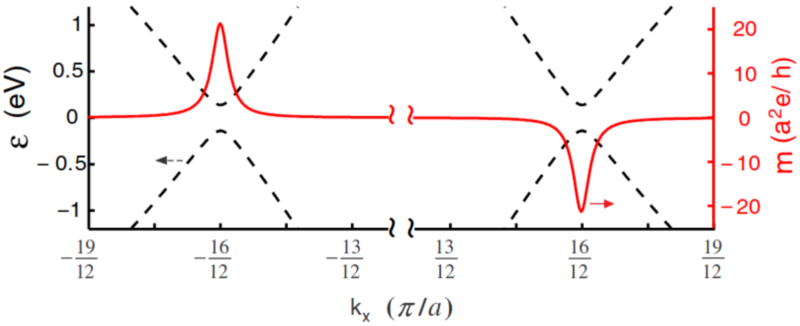

Figure 1.4: Example of Berry curvature around the lifted Dirac points in graphene. The magnetic moment $m(\boldsymbol{p}) \sim (e/\hbar)\Omega_z(\boldsymbol{p})$. Figure adapted from [129].

number is vanishing, meaning that graphene remains topologically trivial. Because of its strong localization, one can still approximately define a valley Chern number that turns out to be exactly half integer $C(\tau) = \tau\,\mathrm{sgn}\,(U_z)/2$, which, in resemblance to the magnetic case, is known as half-skyrmion, or a meron [12, 198]. Therefore, one could say that each valley is independently topological, which can be regarded as a realization of the parity anomaly [199] and leads, in intrinsic graphene, to peculiar steps in the Hall conductivities [163, 200–202]. Another effect of the extremely localized Berry curvature of Eq. (1.57) is the emergence of valley polarized Hall currents in the presence of an electric field [129]. In fact, following Eqs. (1.11), each valley would respond independently and in an opposite way to the electric field, with quantized half-integer Hall conductivity [203, 204]. This is a result of the time-reversal symmetry breaking of each valley independently [205] and could have important applications in the field of valleytronics, where one tries to harness the valley degree of freedom for information processing [206–209]. The nontrivial topology of each individual valley is seen in the existence of valley polarized, dispersive, zero energy modes at the boundary between two layers with opposite mass terms [130, 170, 210–214]. The boundary effectively creates a change in the Chern number of $\Delta C(\tau) = \tau$, which, because of the bulk-boundary correspondence, has to be accompanied by the presence of one metallic mode for each valley. This edge modes are known as kink states and make the interface an effective valley filtering device [215–218]. Note that this is effectively the situation we have seen at the beginning of this thesis in section 1.1.

A KM-SOC, instead, acts as a valley dependent mass term and combines with the staggered onsite potential to give a total mass term $m(\tau) = U_z + \tau\lambda_{\mathrm{KM}}$ for each valley. When increasing λ_{KM} past U_z the gap at one of the valleys closes and reopens. This means that the system passes through a WP in the $(p_x, p_y, \lambda_{\mathrm{KM}})$ parameter space. For what we saw in section 1.3 the graphene bands in the total Brillouin zone must experience a change in the Chern number of $|\Delta C| = 1$. Each spin degree behaves as a Chern insulator, with opposite Chern number $C(\uparrow) = -C(\downarrow)$, which is described by the Haldane Hamiltonian [219]. In this case the topology protects only an odd number of edge states and for this reason it is not labeled with a $\mathbb{Z}$ integer (like the Chern insulators) but with a $\mathbb{Z}_2 = 1, 0$ index, proper of topological insulators [4,10]. This is the Quantum Spin Hall State (QSHS) of graphene [19]. The bulk-boundary correspondence then predicts the existence of metallic edge modes that live on all boundaries of a sample, including the armchair one. These edge modes are helical, meaning the direction of propagation is linked to the spin; a tight-binding computed band structure is shown in Fig. 1.5a. These edge states are topologically protected and cannot backscatter in the absence of time-reversal symmetry breaking impurities [7, 170, 212]. It was predicted that intrinsic graphene has a small $\lambda_{\mathrm{KM}} \approx 40\ \mu\mathrm{eV}$ due to the interaction between the p_z and other orbitals, but this value is too small to produce observable effects at appreciable temperatures [132, 193, 194, 220]. Even though the interaction with a substrate seems to not be able to meaningfully increase the KM-SOC intensity [139, 192, 221], some works suggest that the inverted band structure is still feasible in graphene heterostructures by means of other induced SOCs and exchange interactions [192, 222–224].

Independently, λ_{VZ} and λ_{R} are the two SOCs that do not lift the Dirac degeneracies. The former shifts the Dirac points to energies $E_D = \tau s \lambda_{\mathrm{VZ}}$, opposite for both spin ($s = \pm$) and valley ($\tau = \pm$) degrees of freedom. The latter mixes the spins and shifts the Dirac points in momenta [225]. Due to the opposite energy shift for different spins, λ_{VZ} makes graphene a proper metal, but the two spins degrees are still independent and can be treated separately. In particular, since in intrinsic graphene the existence

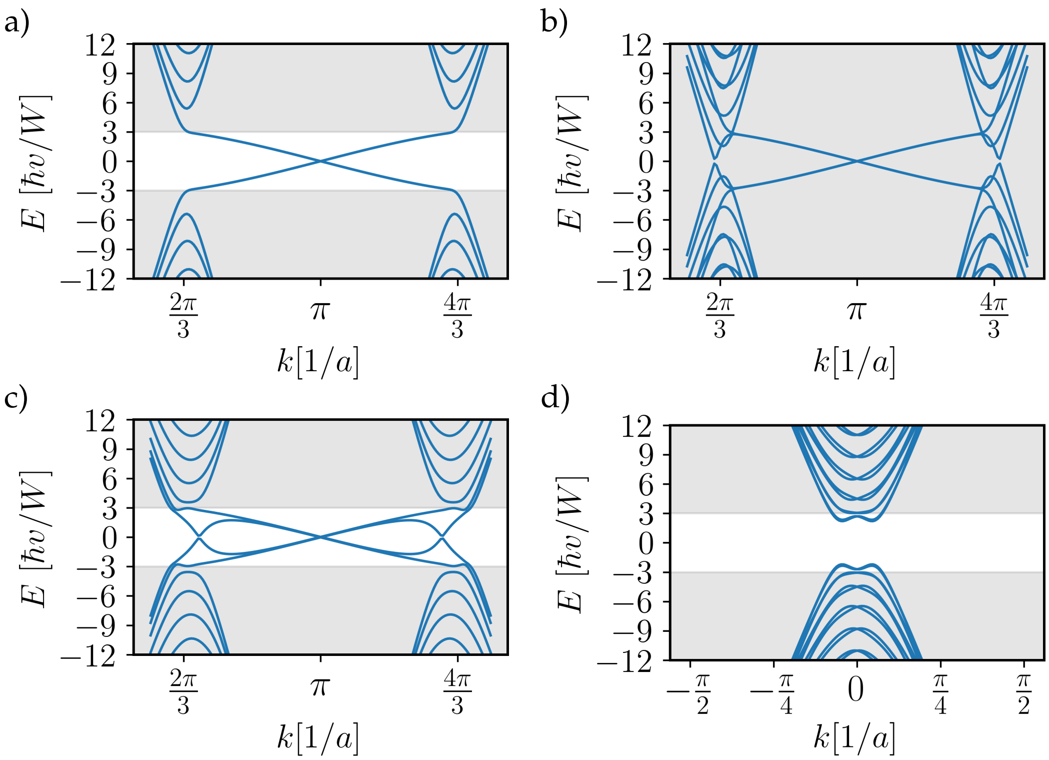

Figure 1.5: Tight-binding computed band structures for a ribbon of width $W = 50a$, where a is the graphene lattice constant. In (a) we have a zigzag ribbon with $\lambda_{\text{KM}} = 3\,\hbar v/W$; the system is in the QSHS phase with helical edge modes that cross the band gap, emphasized by the grayed out region. In (b) we have a zigzag ribbon with $\lambda_{\text{VZ}} = 3\,\hbar v/W$; the system is in a metallic phase with dispersive edge modes. In (c) we have a zigzag ribbon with $\lambda_{\text{VZ}} = 3\,\hbar v/W$ and $\lambda_{\text{R}} = 6\,\hbar v/W$; the system is in the QVSHS phase with both pseudohelical and valley localized edge modes that cross the band gap, emphasized by the grayed out region. In (d) we plot the band structure for an armchair ribbon with the same parameters as in (c): the topological triviality of the system shows in the absence of edge modes along a perfect armchair termination, as emphasized in the main text.

of the (zigzag) edge states was found to have a topological origin, we do not expect them to just vanish in the vicinity of each (shifted) Dirac point [10]. In fact, this is the case and the previously dispersionless edge modes are now forced to acquire a dispersion, proportional to $\lambda_{\rm VZ}$, in order to connect with the Dirac point at the other valley with the same spin but opposite energy [131]. An example of this kind of band structure is shown in Fig. 1.5b for a zigzag ribbon. Note that this is only valid for zigzag-like boundaries that preserve the valley degree of freedom. Indeed, the edge states produced by a VZ-SOC are not topological, like in the KM-SOC case: edge states localized on opposite boundaries but with the same spin polarization move in the same direction, for this reason they were dubbed *pseudo-helical* edge states [131].

The effect of $\lambda_{\rm R}$ on its own is also that of introducing a small dispersion in the graphene edge states, together with a spatial separation of the spin components [225]. Notably, because of its spin mixing effect, a strong enough R-SOC, $|\lambda_{\rm R}| \gtrsim |\lambda_{\rm KM}|$, breaks the graphene QSHS into a metallic phase [19]. When $\lambda_{\rm R}$ is introduced into the metallic phase generated by $\lambda_{\rm VZ}$, its effect is to mix the opposite spin bands that cross the Fermi level, resulting in a gap opening, with a gap width of $2\min(\lambda_{\rm R}, \lambda_{\rm VZ})$. Crucially, the already existing dispersive edge states are not influenced by the presence of $\lambda_{\rm R}$. This allows the existence of a topologically-trivial gapped phase combined with the presence of metallic edge states protected by time-reversal symmetry [131]. The system triviality is ensured by the presence of valley polarized edge states that originate from the bulk band inversion due to the R-SOC spin mixing. Because of this, the phase just described was dubbed QVSHS [131]. A tight-binding computed band structure for this case is shown in Fig. 1.5c, for a zigzag ribbon. In Fig. 1.5d we show the band structure for an armchair ribbon with the same set of parameters, which explicitly show that the system is topologically trivial and the existence of the edge states is limited to zigzag-like terminations.

Recent works suggest that in proximitized monolayer graphene the dominant induced SOCs are indeed of the $\lambda_{\rm VZ}$ and $\lambda_{\rm R}$ types [135, 136, 138, 139, 226–228].

In Chapter 3 we will study the effects of the proximity-induced terms appearing in Hamiltonian (1.56) on the supercurrent of a GJJ. In particular, in the first part of the chapter we will focus on the consequences in bulk transport and in the second one on edge transport. For this reason, in the next section we give a brief introduction to JJs with particular emphasis on those built with monolayer graphene.

1.6 Josephson junctions

In this section, we give an introduction to JJs and in particular on GJJs. This will serve as a basis for the model studied in Chapter 3. We will start by quickly referencing superconductivity, a phenomenon in which certain metals lose their electrical resistance below a critical temperature, and its description in terms of the Bogoliubov-de Gennes Hamiltonian. We will then introduce the JJ, which consists of a junction where a non-superconducting region is interposed between two superconducting elements. Eventually, we will finish with reviewing a general formulation to compute the supercurrent flowing in a JJ in terms of AR and ABS.

1.6.1 Superconductivity

Superconductivity is a phenomenon in which certain materials, when cooled below a characteristic critical temperature, exhibit zero electrical resistance and expel magnetic fields from the their bulk, a behavior known as the Meissner effect [229]. The first superconductor was discovered in 1911 by H.K. Onnes when studying the electrical behavior of mercury at extremely low temperatures [230]. It was not until the 1950s with the publication of the macroscopic Ginzburg-Landau theory [231] and the microscopic BCS theory, from Bardeen, Cooper and Schrieffer [232], that superconductivity was explained in an organic theoretical framework: it was found that superconductivity is an emergent quantum phenomena that survives macroscopic scales.

In a normal metal, the superconductive state is driven by an *attractive* interaction between electron. Because of it, in the BCS description, electrons from opposite crystal momenta and opposite spin, $(k\uparrow, -k\downarrow)$, form bosonic particles called *Cooper pairs*. The BCS Hamiltonian for superconductivity can be written in a second quantization form as[4]

$$H = \sum_{\boldsymbol{k},\sigma} (\varepsilon_{\boldsymbol{k}} - \varepsilon_F)\, c^{\dagger}_{\boldsymbol{k}\sigma}\, c_{\boldsymbol{k}\sigma} + \sum_{\boldsymbol{k},\boldsymbol{k}'} V_{\boldsymbol{k}\boldsymbol{k}'}\, c^{\dagger}_{\boldsymbol{k}\uparrow}\, c^{\dagger}_{-\boldsymbol{k}\downarrow}\, c_{-\boldsymbol{k}'\downarrow}\, c_{\boldsymbol{k}'\uparrow} \tag{1.58}$$

where $V_{\boldsymbol{k}\boldsymbol{k}'}$ characterizes the interaction between electrons, $c^{\dagger}_{\boldsymbol{k}\sigma}$ ($c_{\boldsymbol{k}\sigma}$) creates (annihilates) an electron with momentum $\boldsymbol{k}$ and spin σ and ε_F is the Fermi level. The BCS Hamiltonian can be simplified further in a mean field description by substituting $c^{\dagger}_{\boldsymbol{k}\uparrow}\, c^{\dagger}_{-\boldsymbol{k}\downarrow} = \langle c^{\dagger}_{\boldsymbol{k}\uparrow}\, c^{\dagger}_{-\boldsymbol{k}\downarrow}\rangle + (c^{\dagger}_{\boldsymbol{k}\uparrow}\, c^{\dagger}_{-\boldsymbol{k}\downarrow} - \langle c^{\dagger}_{\boldsymbol{k}\uparrow}\, c^{\dagger}_{-\boldsymbol{k}\downarrow}\rangle)$, which leads to

$$H = \sum_{\boldsymbol{k},\sigma} (\varepsilon_{\boldsymbol{k}} - \varepsilon_F) c^{\dagger}_{\boldsymbol{k}\sigma} c_{\boldsymbol{k}\sigma} + \sum_{\boldsymbol{k}} \Delta_{\boldsymbol{k}} c^{\dagger}_{\boldsymbol{k}\uparrow} c^{\dagger}_{-\boldsymbol{k}\downarrow} + \Delta^*_{\boldsymbol{k}} c_{-\boldsymbol{k}\downarrow} c_{\boldsymbol{k}\uparrow} + C \tag{1.59}$$

where C is a constant and where we have dropped terms of second order in the fluctuations; $\Delta_{\boldsymbol{k}} = \sum_{\boldsymbol{k}'} V_{\boldsymbol{k}\boldsymbol{k}'} \langle c_{-\boldsymbol{k}\downarrow} c_{\boldsymbol{k}\uparrow}\rangle$ is both a definition and a self-consistency equation for the superconducting pairing energy $\Delta_{\boldsymbol{k}}$. We can then commute the creation and annihilation operators of the non-superconducting part for one of the spins, and shift to a Nambu basis representation to obtain[5]

$$H_{\mathrm{BdG}} = \sum_{\boldsymbol{k}} \begin{pmatrix} c_{\boldsymbol{k}\uparrow} & c^{\dagger}_{-\boldsymbol{k}\downarrow} \end{pmatrix} \begin{pmatrix} \varepsilon_{\boldsymbol{k}} - \varepsilon_F & \Delta_{\boldsymbol{k}} \\ \Delta^*_{\boldsymbol{k}} & -\varepsilon_{\boldsymbol{k}} + \varepsilon_F \end{pmatrix} \begin{pmatrix} c^{\dagger}_{\boldsymbol{k}\uparrow} \\ c_{-\boldsymbol{k}\downarrow} \end{pmatrix} \equiv \sum_{\boldsymbol{k}} \Psi^{\dagger} H(\boldsymbol{k}) \Psi \tag{1.60}$$

which is the Bogoliubov-de-Gennes representation of the BCS Hamiltonian. In this representation, the superconducting pairing describes a coupling between the electron, $c^{\dagger}_{\boldsymbol{k}\uparrow}$, and hole, $c_{-\boldsymbol{k}\downarrow}$, degrees of freedom. Diagonalizing $H(\boldsymbol{k})$ one finds that the spectrum of a superconductor is always gapped

$$E_{\boldsymbol{k},\pm} = \pm\sqrt{(\varepsilon_{\boldsymbol{k}} - \varepsilon_F)^2 + \Delta_0^2}, \tag{1.61}$$

where we have assumed a constant profile of the pairing potential in the

---

[4] This is already the reduced form, where one assumes that most of the energy contribution comes from interacting Cooper pairs at zero momentum.

[5] We assume $\varepsilon_{\boldsymbol{k}} = \varepsilon_{-\boldsymbol{k}}$. Moreover, if there was any interaction between the spins in the original Hamiltonian, then one would need to double entirely the Hamiltonian (1.59) and divide by 2 to avoid double counting.

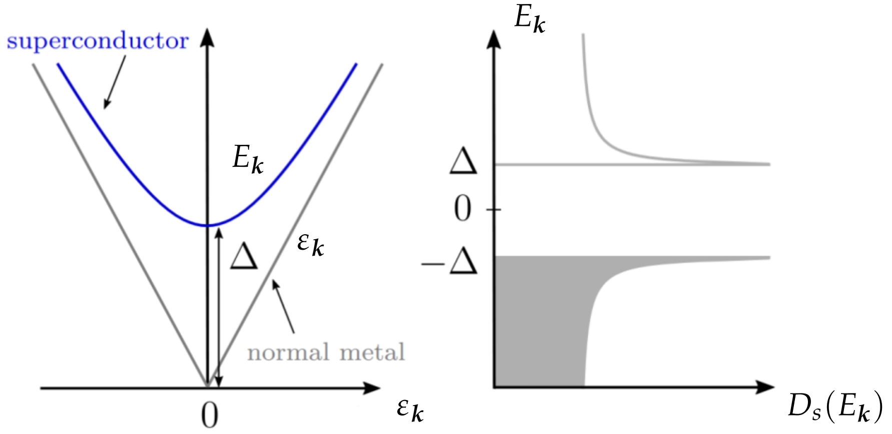

Figure 1.6: Energy dispersion (left) and density of states (right) of Eq. (1.61) for a superconductor with constant pairing potential. Figure adapted from [233].

momentum space[6], $\Delta_{\boldsymbol{k}} = \Delta_0 e^{i\varphi}$; and the eigenstates are

$$\psi_{\pm} = \begin{pmatrix} u_{\boldsymbol{k},\pm} \\ v_{\boldsymbol{k},\pm} \end{pmatrix} = \sqrt{\frac{\Delta_0}{2E_{\boldsymbol{k}}}} \begin{pmatrix} e^{\pm\frac{1}{2}\text{arccosh}(E_{\boldsymbol{k}}/\Delta_0)} e^{i\varphi/2} \\ e^{\mp\frac{1}{2}\text{arccosh}(E_{\boldsymbol{k}}/\Delta_0)} e^{-i\varphi/2} \end{pmatrix}. \tag{1.62}$$

A schematic plot of the energy spectrum and the relative density of state of a superconductor is shown in Fig. 1.6. The BCS ground state of the superconductor can then be written as [234]

$$|\psi_{BCS}\rangle = \Pi_{\boldsymbol{k}}(|u_{\boldsymbol{k}}| + |v_{\boldsymbol{k}}| e^{i\varphi} c^{\dagger}_{\boldsymbol{k}\uparrow} c^{\dagger}_{-\boldsymbol{k}\downarrow})|\psi_0\rangle \tag{1.63}$$

where $c_{\boldsymbol{k}\sigma}|\psi_0\rangle = 0$. Hence, the superconductor ground state is composed of Cooper pairs that all share the same phase factor of φ. This is the emergent macroscopic quantum behavior of superconductivity. Moreover, from a naïve application of the momentum-position uncertainty principle one can find the average distance between electrons in a Cooper pair, the *coherence length* of the superconductor, as [235]

$$\xi \approx \frac{\hbar v_F}{\Delta_0} \tag{1.64}$$

---

[6] An s-wave symmetric superconductor, but there may be pairing potentials with other symmetries.

where v_F is the Fermi energy of the metal in the non-superconducting phase.

1.6.2 Josephson effect

When placing a superconductor and a normal material in contact, the phase coherence between electrons, that characterizes the superconductor, is transferred (via AR [236]) to the normal material, over a length scale comparable to its coherence length ξ. This effect is also an example of proximity effect as we have seen for graphene on a substrate. Placing two superconductors on the side of a normal scattering region forms a JJ. A schematics of a JJ is shown in Fig. 1.7. In the early 60s it was predicted by B. D. Josephson that the overlap between the two superconducting wavefunction with a different phase would lead to a supercurrent flow between the superconductors even at zero voltage difference [237]. For a thin insulating link the supercurrent is sinusoidal in the phase difference [234]

$$I_{\mathrm{s}} = I_{\mathrm{c}} \sin(\varphi_2 - \varphi_1) \equiv I_{\mathrm{c}} \sin(\varphi), \tag{1.65}$$

which is known as the first Josephson equation. The sinusoidal form of this CPR is caused by the low transmission channels through the insulating link, but its shape can change for more transparent materials (such as semiconductors) to include higher harmonics. Josephson also proposed another equation describing the evolution of the phase difference in response to any applied voltage V across the junction [234]

$$\frac{d\varphi}{dt} = \frac{2eV}{\hbar}. \tag{1.66}$$

which is known as the second Josephson equation. Hence, a constant voltage causes an alternating current in the junction with a frequency of $2e/h \approx 484$ MHz/μV, which was initially used to improve the experimental value of $2e/h$ and, eventually, in the contest of the inverse AC Josephson effect [234], led to the definition of the voltage standard in metrology [238].

A very interesting and important setup is that of a superconducting loop interrupted by two JJs. This is known as Superconducting Quantum Interference Device (SQUID). Here, the relevant variable is the gauge

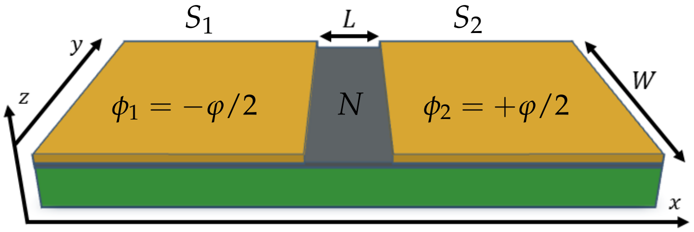

Figure 1.7: Schematic of a JJ, which consists of two superconductors, S_1 and S_2 with phase $\phi_{1,2} = \pm\varphi/2$ (in yellow), connected by a normal material N (in gray) that can be either an insulator (in tunnel junctions) or a metal-semiconductor. In the most general case, the junction is grown on a substrate (shown in green). Figure adapted from [239].

invariant phase, which links the superconducting phase differences between the junctions, $\Delta\varphi_1$ and $\Delta\varphi_2$, to the magnetic flux, Φ, threading the loop as [234]

$$\Delta\varphi_1 - \Delta\varphi_2 = \frac{2\pi\Phi}{\Phi_0} \,(\mathrm{mod}\ 2\pi) \tag{1.67}$$

where $\Phi_0 = h/2e$ is the magnetic flux quantum. For two equal junctions in the SQUID, this leads to a combined maximum supercurrent of

$$I_m = 2I_c|\cos\left(\pi\Phi/\Phi_0\right)|. \tag{1.68}$$

Because of this, SQUID devices are flux to voltage transducers and make for incredibly sensitive magnetometers [234].

From Eqs. (1.65,1.66) we can compute the energy of a JJ when used as a circuit element as

$$E_\mathrm{J}(\varphi) = \int I_\mathrm{s} V dt = \int I_\mathrm{c}\sin(\varphi)\frac{\hbar}{2e}d\varphi = -E_\mathrm{J}\cos(\varphi), \tag{1.69}$$

where $E_\mathrm{J} = I_\mathrm{c}\hbar/2e$ is the Josephson energy. When coupled with a capacitance, the non-linearity of Eq. (1.69) provides the circuit with an anharmonic energy spectrum, that lends itself to perform as a quantum bit. For this reason, JJs are at the core of the development in superconducting quantum computing. In particular, the ratio between the Josephson energy and the charging energy of the capacitance , $E_\mathrm{C} = 2e^2/C$, selects the mode of operation of the qubit, making it suitable for different applications [240]. More recently, semiconductor-based JJs have attracted much attention in the literature due to the possibility of modifying the number of carriers of the superconducting element via a gate voltage. This allows for a gate-tunable E_J/E_C ratio. Implementations of this kind are sometimes known as gatemons and have been made with a variety of materials, including semiconducting nanowires [102, 241], InAs [102, 103, 241–244], 2D materials [104], van der Waals heterostructures [105], germanium [106, 245–247] and graphene [107, 248]. Unlike JJs with an insulating weak link, semiconductor-based JJs are generally characterized by few high transmission channels that produce a skewed CPR with higher harmonic content [103,108,109,249]. JJs of this kind are being theoretically proposed as a means to realize topological matter in the phase space [110, 111] and topological superconductivity [112, 250]. They were also proven to suppress charge dispersion in transmon-like qubits [251–254]. Moreover, when arranged in a SQUID configuration, it was demonstrated that the higher harmonics could be used to implement high-efficiency superconducting diodes [113,114,246,255] and also parity protected $\sin(2\varphi)$ qubits [114–116,246,256–261].

In chapter 3, we show the results for the CPR of a JJ made with proximitized graphene. We will study the ballistic and short junction regime and find that this setup allows for a JJ with a highly tunable harmonic content via external gates and electric fields, which can be appropriate for electronic applications such as the ones we just discussed.

1.6.3 Andreev reflection and supercurrent

In this section, we describe the supercurrent flowing in a JJ in terms of AR and ABSs. After introducing these two concepts, we will show how to apply them in the computation of the supercurrent via a scattering matrix formalism [262].

The AR is a unique process that can occur at the interface between a normal conductor and a superconductor [263, 264]. At the interface, an electron incoming from the normal conductor can pair with a second electron in the superconductor to form a Cooper pair; as a consequence of momentum and charge conservation, a hole with opposite spin and momentum is retroreflected inside the normal conductor. We can write the wavefunction of the process as

$$\psi(x) = \left[\begin{pmatrix}1\\0\end{pmatrix} e^{ik_e x} + r\begin{pmatrix}0\\1\end{pmatrix} e^{ik_h x}\right]\Theta(-x) + t\begin{pmatrix}u\\v\end{pmatrix} e^{ik_s x}\Theta(x) \tag{1.70}$$

where $\Theta(x)$ is the Heaviside function and (u, v) is the positive energy eigenvector of $H(\boldsymbol{k})$ in Eq. (1.62). Eq. (1.70) is only valid in the Andreev approximation limit, where we assume that the Fermi level is much higher than the other energies: in such a way $k_{e,h} \approx k_s \approx k_F$ and imposing the continuity of the wavefunction also guarantees the continuity of its derivative. Setting $\psi(0^-) = \psi(0^+)$ one gets $1 = tu$ and $r = v/u$; so that the acquired phase of the reflected hole is

$$r(\varphi) = e^{-i\varphi}\begin{cases} e^{-i\,\mathrm{arccos}(E/\Delta_0)} & \text{for} \quad E < \Delta_0 \\ e^{-\mathrm{arccosh}(E/\Delta_0)} & \text{for} \quad E > \Delta_0 \end{cases} . \tag{1.71}$$

Similarly, one obtains $r(-\varphi)$ for the reverse process of a hole being retroreflected as an electron. A plot of the probabilities of being reflected, $R = rr^*$, versus of being transmitted, $T = tt^*$, as a function of the energy is shown in Fig. 1.8. Inside the superconducting gap, $E < \Delta_0$, there are no propagating states in the superconductor, so the probability of retroreflection is unity. Therefore, at subgap energies in a JJ, the cycle of retroreflection of an electron into a hole from one superconductor and again into an electron from the other one can continue indefinitely when the total acquired phase is a multiple of 2π. The state thus formed is called an ABS. As we saw, in an ABS, the electrons and holes move in opposite direction. In this way, even though there is no quasiparticle current, there can be a net charge current flowing through the junction, carried by the ABSs.

The constructive interference condition can also be stated in a different way using the scattering matrix formalism [262]. In order to obtain a well-defined scattering problem we imagine inserting clean normal leads between the central region of the JJ, that we call now the scattering region, and the superconducting leads. In these leads we can define a basis of incoming (toward the scattering region) and outgoing (toward the superconducting leads) modes for both electron and hole degrees of

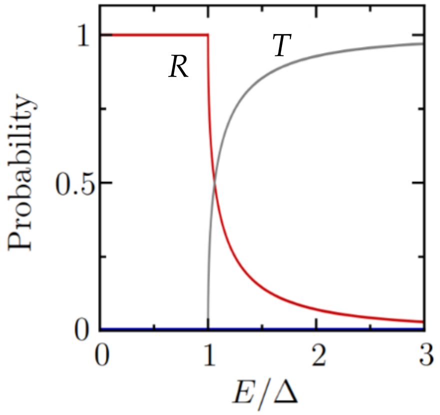

Figure 1.8: Probabilities of an electron to be Andreev reflected, R, and to be transmitted into the superconducor, T. Figure adapted from [265].

freedom. $\Psi_{\mathrm{in}} = (\psi^e_{\mathrm{in}}, \psi^h_{\mathrm{in}})$ and $\Psi_{\mathrm{out}} = (\psi^e_{\mathrm{out}}, \psi^h_{\mathrm{out}})$ are the components of a wavefunction in terms of the previously defined basis of incoming and outgoing modes. In particular, each of the components $\psi^{e,h}_{\mathrm{in,out}}$ refers to modes on both sides of the scattering region. Using Eq. (1.71) the effect of the scattering with the superconductors can be collectively written as $\Psi_{\mathrm{in}} = S_{\mathrm{A}}(E)\Psi_{\mathrm{out}}$ with

$$S_{\mathrm{A}}(E) = e^{-i\arccos(E/\Delta_0)} \begin{pmatrix} 0 & r^*_{\mathrm{A}} \\ r_{\mathrm{A}} & 0 \end{pmatrix}, \tag{1.72}$$

where

$$r_{\mathrm{A}} = \begin{pmatrix} e^{i\varphi/2}\mathbf{1} & 0 \\ 0 & e^{-i\varphi/2}\mathbf{1} \end{pmatrix} \tag{1.73}$$

is the matrix of phases acquired in a electron to hole AR, and viceversa for r^*_{A}. In Eq. (1.73), $\mathbf{1}$ is the $N \times N$ identity matrix, where N is the number of modes on the two imaginary leads (which we are assuming equal for simplicity) and the phases of the right and left superconductors are $\varphi_{\mathrm{R}} = +\varphi/2$ and $\varphi_{\mathrm{L}} = -\varphi/2$, respectively. The effect of the scattering within the central region is given instead by $\Psi_{\text{out}} = S_{\text{N}}(E)\Psi_{\text{in}}$ with

$$S_{\text{N}}(E) = \begin{pmatrix} s(E) & 0 \\ 0 & s^*(-E) \end{pmatrix}, \tag{1.74}$$

where

$$s(E) = \begin{pmatrix} r_{\text{LL}} & t_{\text{LR}} \\ t_{\text{RL}} & r_{\text{RR}} \end{pmatrix}, \tag{1.75}$$

is the scattering matrix for the electrons and $s^*(-E)$ that for the holes [7]. At this point, we can write the condition for the constructive interference of an ABS as [110,262]

$$S_{\text{A}} S_{\text{N}}(E)\Psi_{\text{in}} = \Psi_{\text{in}}, \tag{1.76}$$

which can be rewritten in the following way

$$\begin{pmatrix} s^\dagger(E) & 0 \\ 0 & s^T(-E) \end{pmatrix} \begin{pmatrix} 0 & r_{\text{A}} \\ r_{\text{A}}^* & 0 \end{pmatrix} \Psi_{\text{in}} = e^{-i \arccos(E/\Delta_0)} \Psi_{\text{in}}. \tag{1.77}$$

We can then use the transformation $X \to \frac{1}{2}(X + X^{-1})$ to obtain

$$\begin{pmatrix} 0 & A^\dagger(E) \\ A(E) & 0 \end{pmatrix} \Psi_{\text{in}} = \frac{E}{\Delta_0} \Psi_{\text{in}}, \tag{1.78}$$

where $A(E) = \frac{1}{2}\left[r_{\text{A}}^* s(E) + s^T(-E) r_{\text{A}}^*\right]$. Eq. (1.78) can then be squared to separate electron and hole subspaces; for the electron subspace we obtain

$$\left[A^\dagger(E) A(E)\right] \psi_{\text{in}}^e = \left(\frac{E}{\Delta_0}\right)^2 \psi_{\text{in}}^e. \tag{1.79}$$

In the short junction regime, for $L \ll \xi$, where L is the length of the JJ, $\hbar v_F/L$, known as Thouless energy, becomes the dominant energy scale. This allows us to neglect the energy dependence of $A(E)$ in the above

---

[7] In order for $s^*(-E)$ to be the scattering matrix of the hole subsector, the hole modes of the lead have to be chosen as the particle-hole symmetric of the electron ones. Otherwise, there may be extra phases or permutations that would need to be addressed.

equations. Doing so and deriving Eq. (1.79) with respect to the phase difference across the junction, we obtain [266]

$$\frac{dE_p}{d\varphi} = \frac{\Delta_0^2}{2E_p} \left\langle \psi_{\text{in}}^e \middle| \frac{d(A^\dagger A)}{d\varphi} \middle| \psi_{\text{in}}^e \right\rangle_p \tag{1.80}$$

where p runs over the eigenstates of $A^\dagger A$. Finally, using Eq. (1.80) the supercurrent flowing through the JJ at zero temperature can be directly computed via the formula[8] [173,267–270]

$$I(\varphi) = -\frac{2e}{\hbar} \sum_{E_p<0} \frac{dE_p}{d\varphi}, \tag{1.81}$$

which is correct in the short junction approximation, when the supercurrent carried by the supragap, $|E| > \Delta_0$, propagating states can be neglected [268].

If the scattering region of the junction is time-reversal symmetric, then we can simplify the expression for the ABSs energy even more. Indeed, using $s^T = -s$ and performing a series of matrix manipulations[9], we can transform the eigenvalue problem of Eq. (1.79) into [268]

$$\det\left[\left(1 - \frac{E^2}{\Delta_0^2}\right)\mathbf{1} - t_{\text{LR}} t_{\text{LR}}^\dagger \sin^2\left(\frac{\varphi}{2}\right)\right] = 0, \tag{1.83}$$

which is solved for E in terms of the eigenvalues, T_p, of $t_{\text{LR}} t_{\text{LR}}^\dagger$ as

$$E_p = \pm\Delta_0\sqrt{1 - T_p \sin^2(\varphi/2)}. \tag{1.84}$$

Eq. (1.84) directly connects the transmission probabilities of the scattering problem inside the normal region of the junction to the supercurrent via

---

[8] In going from Eq. (1.78) to Eq. (1.79) we have lost information on the sign of the ABS energy and only have access to $|E_p|$. So, practically, in the next equation we do sum over all the egienstates of q. (1.79) and halve the result [266].

[9] These manipulations involve the use of the folding identity

$$\det\begin{pmatrix} a & b \\ c & d \end{pmatrix} = \det(ad - aca^{-1}b), \tag{1.82}$$

which allows us to reduce the dimensionality of the matrices involved.

Eq. (1.81)

$$I(\varphi) = \frac{2e\Delta_0}{\hbar} \sum_p \frac{T_p\,(k)\sin\phi}{4\sqrt{1 - T_p\,(k)\sin^2(\phi/2)}} \tag{1.85}$$

where the summation is on all transmission channels across the junction in one direction.

Chapter 2

Interface System between Floquet-Weyl semimetals

In this chapter, we study the emergence of electronic surface states at the interface between two half-spaces of a NLSM irradiated by two monochromatic light beams with opposite circular polarizations, respectively. Here, we show how two different light intensities can modify the electronic band structure and even introduce a Van Hove singularity (VHS) in the density of states of the interface system. A VHS is a logarithmic divergence in the density of states generally caused by a saddle point in the energy spectrum of 2D systems [235, 271]. When VHSs lie at the Fermi energy, they enhance electron interactions and can cause electronic instabilities: they can induce phenomena such as superconductivity [272–286], charge density waves [283,287,288] and spin density waves [282,283,289–291]. For these reasons, VHSs in topological systems have attracted great interest in the aim for exotic correlated quantum states [292–298], such as topological superconductivity [299–301]. Moreover, we find that, by adding a narrow magnetic barrier at the interface between the two induced WSMs, it is possible to switch on/off a topological phase of the interface system by using suitable different light intensities.

The results of this chapter have been published by F. Bonasera, S.-B. Zhang, L. Privitera, and F. M. D. Pellegrino in *Tunable interface states between Floquet-Weyl semimetals*, Phys. Rev. B **106**, 195115 [302].

This Chapter is organized as follows. In Sec. 2.1 we introduce a sim-

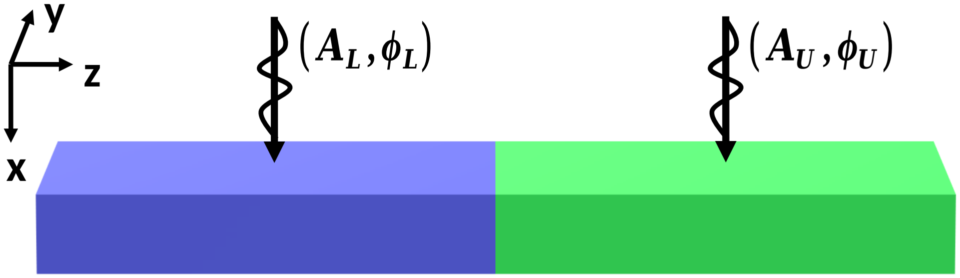

Figure 2.1: Schematic of the system. The lower, $z < 0$, and upper, $z > 0$, half-spaces of the infinite NLSM are irradiated by high frequency monochromatic lights of intensities and polarizations $(A_\mathrm{L}, \phi_\mathrm{L})$ and $(A_\mathrm{U}, \phi_\mathrm{U})$, respectively.

ple two-band model used to describe a z-symmetric NLSM, it is a simplified version of the one we presented in Sec. 1.4.2. In Sec. 2.2, following Ref. [85], we show how, using the Floquet formalism in the high frequency limit [162], the circularly polarized light induces a transition from NLSM to WSM; this is similar to what we already showed in Sec. 1.4.3 but using the simplified version of the model. In Sec. 2.3, we study the interface states which lay along the boundary between two induced WSMs. Within the two-band model, the interface eigenstates have a spinorial form, where the components represent the orbital degree of freedom. Here, we focus on energy dispersion and pseudo-spin texture $\langle \boldsymbol{\sigma} \rangle$ evaluated on the interface states, where the Pauli matrix vector $\boldsymbol{\sigma}$ acts on the orbital subspace. Finally, we show in Sec. 2.4 the topological effects on the interface system of introducing a magnetic barrier between the two induced WSMs.

2.1 Model

In this work, we study the interface states which emerge at the boundary plane of two half-spaces of an infinite NLSM irradiated respectively by two light beams of opposite circular polarizations. Figure 2.1 shows the setup analyzed, where the upper (lower) half-space $z < 0$ ($z > 0$) is represented by the blue (green) region of the NLSM, and it is irradiated by a light beam characterized by an intensity $A_{\rm L}$ ($A_{\rm U}$) and a phase $\phi_{\rm L}$ ($\phi_{\rm U}$). Here, we focus on monochromatic light in the high frequency regime, such that we can use the high frequency expansion within the Floquet formalism [162]. Without loss of generality, we consider a light drive polarized along the $y-z$ plane and described by the following vector potential

$$\boldsymbol{A}(t) = A\left[0, \cos(\omega t), \sin(\omega t + \phi)\right], \tag{2.1}$$

where $\phi = 0$ ($\phi = \pi$) corresponds to the right (left) handed circular polarization.

In Sec. 1.4.1 we saw an example of a WSM Hamiltonian with a minimal set of WPs. To analyze the interface states which lay along the plane $z = 0$, without loss of generality, in the Hamiltonian expressed in Eq. (1.22) we disregard the quadratic momentum contribution along z-direction, proportional to σ_x. This simplification allows the use of a fully analytical approach without missing any topological features of the electron system. In the appendix A.1 we show that the numerical results, obtained including the quadratic k_z component, are in full agreement with the ones we find analytically. Therefore, we describe the low-energy electronic properties of the NLSM using the following Hamiltonian

$$H(\boldsymbol{k}) = \left[m - B\left(k_x^2 + k_y^2\right)\right]\sigma_x + v k_z \sigma_z, \tag{2.2}$$

where $\{\sigma_i\}$ are the Pauli matrices which act on an orbital subspace, and, for sake of simplicity, we have dropped the electron-hole symmetry breaking term proportional to the identity, $\varepsilon(\boldsymbol{k})\sigma_0$. It is useful to rewrite the Hamiltonian (2.2) as

$$\mathcal{H}\left(\boldsymbol{p}\right) = \left[1 - \left(p_x^2 + p_y^2\right)\right]\sigma_x + u p_z \sigma_z, \tag{2.3}$$

where the energies are expressed in units of m, and the dimensionless momentum and velocity are defined as $\boldsymbol{p} = \boldsymbol{k}/b$ and $u = (b/m)v$, with $b = \sqrt{m/B}$. The eigenenergies of the Hamiltonian (2.3) are expressed as

$$E_\pm(\boldsymbol{p}) = \pm\sqrt{\left[1 - \left(p_x^2 + p_y^2\right)\right]^2 + \left(u p_z\right)^2}\,, \tag{2.4}$$

where conduction and valence bands touch each other at the circular nodal ring defined by $p_x^2 + p_y^2 = 1$, on the $p_z = 0$ plane. Finally, as pointed out in Sec. 1.4.2, we notice that the nodal ring is protected by the z-mirror symmetry, i.e. $(i\sigma_x)\mathcal{H}(\boldsymbol{p}_\perp, p_z)(-i\sigma_x) = \mathcal{H}(\boldsymbol{p}_\perp, -p_z)$, where $\boldsymbol{p}_\perp = (p_x, p_y)$.

2.2 Driving a nodal-line semimetal into a Floquet-Weyl semimetal

Following Ref. [85], within the Floquet formalism and according to the high frequency expansion, we show here how a NLSM can be driven into a FWSM by shining circularly polarized monochromatic light on it. This is the same procedure as the one we explained in Sec. 1.4.3. We briefly repeat the procedure here because the Hamiltonian is slightly different, having neglected the k_z^2 term, and also for the sake of establishing a consistent dimensionless notation throughout the rest of the chapter.

In the presence of the vector potential of the form expressed in Eq. (2.1), by applying the Peierls substitution $\boldsymbol{p} \to \boldsymbol{p} + e\boldsymbol{A}(t)/b$, we obtain a time periodic Hamiltonian

$$\begin{aligned}\mathcal{H}(\boldsymbol{p}, t) = &\left\{1 - p_x^2 - \left[p_y + e\Lambda\cos(\omega t)\right]^2\right\}\sigma_x \\ &+ u\left[p_z + e\Lambda\sin\left(\omega t + \phi\right)\right]\sigma_z,\end{aligned} \tag{2.5}$$

where the dimensionless quantity $\Lambda = A/b$ is proportional to the light intensity A. The periodic Hamiltonian above can be expanded in Fourier series as $\mathcal{H}(\boldsymbol{p}, t) = \sum_n \mathcal{H}_n(\boldsymbol{p})e^{-in\omega t}$, where

$$\mathcal{H}_0 = \left[1 - e^2\Lambda^2/2 - \left(p_x^2 + p_y^2\right)\right]\sigma_x + up_z\sigma_z \tag{2.6a}$$

$$\mathcal{H}_{\pm1} = -e\Lambda\left(2p_y\sigma_x \pm ie^{\pm i\phi}u\sigma_z\right)/2, \tag{2.6b}$$

$$\mathcal{H}_{\pm2} = -e^2\Lambda^2\sigma_x/4\,, \tag{2.6c}$$

and $\mathcal{H}_{\pm n} = 0$ for $|n| > 2$. Within the Floquet formalism, in the high frequency regime ($\omega \gg |m|$), we resort to a perturbative approach which describes the dynamics of the system by the time independent effective Hamiltonian [162]

$$\mathcal{H}_{\text{eff}}(\boldsymbol{p}) = \mathcal{H}_0(\boldsymbol{p}) + \sum_{n\geq 1} \frac{[\mathcal{H}_{+n}, \mathcal{H}_{-n}]}{n\Omega} + \mathcal{O}\left(\frac{1}{\Omega^2}\right), \tag{2.7}$$

where $\Omega = \omega/m$ is the frequency of the incident light in units of m. Using the Fourier coefficients expressed in Eqs. (2.6), we obtain the following commutators

$$\begin{aligned}
[\mathcal{H}_{+1}, \mathcal{H}_{-1}] &= \frac{e^2\Lambda^2}{4}\left[2p_y\sigma_x + ie^{i\phi}u\sigma_z, 2p_y\sigma_x - ie^{-i\phi}\sigma_z\right] \\
&= \frac{e^2\Lambda^2 u p_y}{2}\left(e^{i\phi} + e^{-i\phi}\right) i\left[\sigma_z, \sigma_x\right] \\
&= -2e^2\Lambda^2 u \cos\left(\phi\right) p_y\sigma_y, && \text{(2.8a)} \\
[\mathcal{H}_{+2}, \mathcal{H}_{-2}] &= 0, && \text{(2.8b)}
\end{aligned}$$

which lead to the effective Hamiltonian

$$\mathcal{H}_{\text{eff}}(\boldsymbol{p}) = \left[\bar{p}^2 - \left(p_x^2 + p_y^2\right)\right]\sigma_x + \lambda p_y\sigma_y + u p_z\sigma_z, \tag{2.9}$$

where

$$\begin{aligned}
\bar{p} &= \sqrt{1 - e^2\Lambda^2/2}, && \text{(2.10a)} \\
\lambda &= -2e^2\Lambda^2 u \cos\left(\phi\right)/\Omega. && \text{(2.10b)}
\end{aligned}$$

The corresponding eigenenergies are

$$\mathcal{E}_{\pm}\left(\boldsymbol{p}\right) = \pm\sqrt{\left[\bar{p}^2 - \left(p_x^2 + p_y^2\right)\right]^2 + \left(\lambda p_y\right)^2 + \left(u p_z\right)^2}, \tag{2.11}$$

which are degenerate only at two WPs placed at $\boldsymbol{P}_{\pm} = (\pm\bar{p}, 0, 0)$. As already established, by linearizing the Hamiltonian in the WPs, we find their chiralities as $\chi_{\pm} = \mathrm{sgn}[\mathrm{Det}(v_{ij})] = \pm\,\mathrm{sgn}\left(\cos\phi\right)$. These are only determined by the polarization of the incident light [85].

2.3 Interface system

In this section, we focus on the states which emerge at the interface between two regions of an infinite NLSM irradiated by two beams of light with opposite circular polarizations. In the high frequency regime, we describe each region by the effective Floquet Hamiltonian of Eq. (2.11), which we denote as H_{U} (H_{L}) for the upper (lower) half-space $z > 0$ ($z < 0$). These effective Floquet Hamiltonians are expressed as

$$\mathcal{H}_j\left(\boldsymbol{p}\right) = \left[\bar{p}_j^2 - \left(p_x^2 + p_y^2\right)\right]\sigma_x + \lambda_j p_y \sigma_y + u p_z \sigma_z \tag{2.12}$$

where

$$\bar{p}_j = \sqrt{1 - e^2\Lambda_j^2/2}, \tag{2.13a}$$

$$\lambda_j = -2e^2\Lambda_j^2 u \cos\left(\phi_j\right)/\Omega, \tag{2.13b}$$

$$\Lambda_j = \frac{A_j}{b}, \tag{2.13c}$$

$j \in \{\mathrm{L}, \mathrm{U}\}$ denoting the relative half-space, and $\operatorname{sgn}\left(\lambda_{\mathrm{U}}\lambda_{\mathrm{L}}\right) < 0$ because of the opposite circular polarizations of the two beams of light.

We note here that the assumption we make of an infinitely sharp interface between the two regions does not undermine the results of the study. Indeed, in this work we study topological interface modes which are a consequence of the topology mismatch between the two regions and are thus robust against the details of the system, such as those of the interface. For example, this was shown in Ref. [303] where the authors find that the degree of smoothness of an interface between topological materials does not interfere with the metallic interface modes and does, instead, introduce spurious massive interface modes in addition to the topological ones.

In order to find the interface states, firstly, we solve separately the two Schrödinger equations associated with each half-space, then we impose the normalizability of the wavefunction, and its continuity at the $z = 0$ interface. To do so we replace p_z with $-i\partial_z$, while, because of the translational invariance along the x and y directions, p_x and p_y remain good quantum numbers. The stationary Schrödinger equation associated with each half-space is expressed as

$$\mathcal{H}_j\left(\boldsymbol{p}_\perp, p_z \to -i\partial_z\right)\psi_j\left(\boldsymbol{r}\right) = \mathcal{E}\left(\boldsymbol{p}_\perp\right)\psi_j\left(\boldsymbol{r}\right), \tag{2.14}$$

where $\boldsymbol{p}_\perp = \left(p_x, p_y\right)$, $\mathcal{E}\left(\boldsymbol{p}_\perp\right)$ is the eigenenergy, and all lengths are measured in units of $1/b$. To solve the problem above, we use the following Ansatz [304]

$$\psi_j(\boldsymbol{r}) = e^{ip_x x}e^{ip_y y}\begin{pmatrix}\psi_1^j\\ \psi_2^j\end{pmatrix}e^{\mu_j z}, \tag{2.15}$$

which is spatially localized close to the plane $z = 0$ only if $\mathrm{Re}\left(\mu_j z\right) < 0$, where $|\mathrm{Re}\left(\mu_j\right)|$ represents the inverse localization length of the interface states around the $z = 0$ plane. By replacing Eq. (2.15) into Eq. (2.14), we obtain the secular equation for the eigenenergies

$$\det\left[\mathcal{H}_j\left(\boldsymbol{p}_\perp, \partial_z \to \mu_j\right) - \mathcal{E}\mathbb{1}\right] = 0, \tag{2.16}$$

which is solved by $\mu_j = \pm\bar{\mu}_j$, where

$$\bar{\mu}_j \equiv \frac{1}{u}\sqrt{\left[\bar{p}_j^2 - \left(p_x^2 + p_y^2\right)\right]^2 + \left(\lambda_j p_y\right)^2 - \mathcal{E}^2}, \tag{2.17}$$

which can be either a real or a pure imaginary number. For each half-space j, by setting $\mu_j = \pm\bar{\mu}_j$, the non-trivial solutions of the homogeneous linear system $\left[\mathcal{H}\left(\boldsymbol{p}_\perp, \pm\bar{\mu}_j\right) - \mathcal{E}\right]\left(\psi_{1,\pm}^j, \psi_{2,\pm}^j\right)^T = 0$ are found as

$$\begin{pmatrix}\psi_{1,\pm}^j\\ \psi_{2,\pm}^j\end{pmatrix} = \begin{pmatrix}\bar{p}_j^2 - \left(p_x^2 + p_y^2\right) - i\lambda_j p_y\\ \pm iu\bar{\mu}_j + \mathcal{E}\end{pmatrix}. \tag{2.18}$$

For a given $\boldsymbol{p}_\perp$, the general wavefunction is expressed in the spinorial form as

$$\Psi_{\boldsymbol{p}_\perp}\left(\boldsymbol{r}\right) = \mathcal{N}e^{ip_x x}e^{ip_y y}[\Theta(-z)\Phi_{\mathrm{L}}\left(z\right) + \Theta(z)\Phi_{\mathrm{U}}\left(z\right)], \tag{2.19}$$

$$\Phi_j\left(z\right) = \sum_{\ell=\pm} C_\ell^j \begin{pmatrix}\psi_{1,\ell}^j\\ \psi_{2,\ell}^j\end{pmatrix} e^{\ell\bar{\mu}_j z}, \tag{2.20}$$

where $j \in \{\mathrm{L}, \mathrm{U}\}$, $\mathcal{N}$ is the normalization prefactor, and $\Theta(z)$ is the Heaviside step function. The coefficients $\{C_\ell^j\}$ are determined by imposing the boundary conditions. The first condition is the the normalizability of the wavefunction, which is equivalent to impose $\Psi(\boldsymbol{r}) \to 0$ for $|z| \to \infty$. The second one is the continuity of the wavefunction at $z = 0$. The former is satisfied by setting $C_{+}^{\mathrm{U}} = 0$ and $C_{-}^{\mathrm{L}} = 0$. Then, the continuity condition can be compactly expressed as

$$\mathcal{M}\boldsymbol{C} = 0, \tag{2.21}$$

where

$$\mathcal{M} = \begin{pmatrix} \psi_{1,-}^{\mathrm{U}} & -\psi_{1,+}^{L} \\ \psi_{2,-}^{\mathrm{U}} & -\psi_{2,+}^{\mathrm{L}} \end{pmatrix}, \tag{2.22}$$

and $\boldsymbol{C} = (C_{-}^{\mathrm{U}}, C_{+}^{\mathrm{L}})^{\mathrm{T}}$. For a given $\boldsymbol{p}_{\perp}$, Eq. (2.21) is solved by a non trivial set of coefficients $\{C_{-}^{\mathrm{U}}, C_{+}^{\mathrm{U}}\}$, for the values of energy $\mathcal{E}$ for which the determinant of $\mathcal{M}$ vanishes.

2.3.1 Interface electronic band

The secular equation $\det \mathcal{M} = 0$ is explicitly expressed as

$$\begin{aligned} &\left(-iu\bar{\mu}_{\mathrm{U}} + \mathcal{E}\right)\left(\alpha_{\mathrm{L}} - i\lambda_{\mathrm{L}} p_y\right) \\ &- \left(iu\bar{\mu}_{\mathrm{L}} + \mathcal{E}\right)\left(\alpha_{\mathrm{U}} - i\lambda_{\mathrm{U}} p_y\right) = 0, \end{aligned} \tag{2.23}$$

where $\alpha_j = \bar{p}_j^2 - \left(p_x^2 + p_y^2\right)$. Its solution is obtained performing simple algebraic calculations that are reproduced in Appendix A.2, and it is found as

$$\mathcal{E}\left(\boldsymbol{p}_{\perp}\right) = \frac{p_y \left\{\left[1 - \left(p_x^2 + p_y^2\right)\right]\left(\Lambda_{\mathrm{L}}^2 \cos\phi_{\mathrm{L}} - \Lambda_{\mathrm{U}}^2 \cos\phi_{\mathrm{U}}\right) - \frac{e^2}{2}\Lambda_{\mathrm{U}}^2 \Lambda_{\mathrm{L}}^2 \left(\cos\phi_{\mathrm{L}} - \cos\phi_{\mathrm{U}}\right)\right\}}{\sqrt{\left(\frac{\Omega}{4u}\right)^2 \left(\Lambda_{\mathrm{U}}^2 - \Lambda_{\mathrm{L}}^2\right)^2 + \left(\Lambda_{\mathrm{U}}^2 \cos\phi_{\mathrm{U}} - \Lambda_{\mathrm{L}}^2 \cos\phi_{\mathrm{L}}\right)^2 p_y^2}}, \tag{2.24}$$

where the inequality $\cos\phi_{\mathrm{U}} \cos\phi_{\mathrm{L}} < 0$ guarantees a mismatch in topology between the two regions and, consequently, the existence of the interface states. For each $\boldsymbol{p}_{\perp}$, $\mathcal{E}(\boldsymbol{p}_{\perp})$ represents the eigenenergy of an interface state when both $\mathrm{Re}\bar{\mu}_{\mathrm{L}} \neq 0$ and $\mathrm{Re}\bar{\mu}_{\mathrm{U}} \neq 0$. Otherwise, if $\mathrm{Re}\bar{\mu}_{\mathrm{L}} = 0$ ($\mathrm{Re}\bar{\mu}_{\mathrm{U}} = 0$) the solution obtained is delocalized along the lower (upper) half-space, and it describes a bulk state. Therefore, the condition $\bar{\mu}_{\mathrm{L}}\bar{\mu}_{\mathrm{U}} = 0$ allows defining the boundaries of the domain of existence in the two-dimensional (2D) momentum space of the interface states.

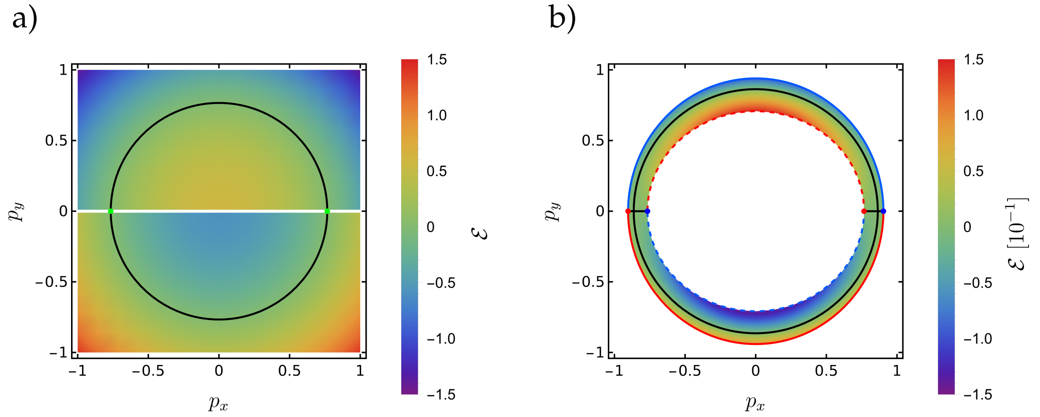

Figure 2.2: Density plots of the energy dispersion of the interface states as a function of the momentum $\boldsymbol{p}_\perp = (p_x, p_y)$. In both panels, the black lines represent the Fermi line $\mathcal{E} = 0$, and we set $u = 1, \Omega = 10$, $\phi_\mathrm{U} = \pi$ and $\phi_\mathrm{L} = 0$. In panel (a), the light intensities are identical, $\Lambda_\mathrm{U} = \Lambda_\mathrm{L} = 3$. Here, each green dot represents two coincident WPPs with opposite chiralities, and the solid white line represents the locus where the interface electronic band merges into the bulk bands. In panel (b), the light intensities are different, $\Lambda_\mathrm{U} = 2$ and $\Lambda_\mathrm{L} = 3$. Here, the boundary solid (dashed) lines are solutions of $\bar{\mu}_\mathrm{U} = 0$ ($\bar{\mu}_\mathrm{L} = 0$). In particular, the red (blue) lines describe the merging of the interface band into a conduction (valence) bulk band. Moreover, red and blue dots represent WPPs with positive and negative chirality, respectively.

We infer that the topological properties of the interface states depend on the relative arrangement in 2D momentum space $k_x - k_y$ of the Weyl Points surface Projection (WPP) of the upper and lower FWSMs. In our system, this relative arrangement is determined by the different light intensities on the two half-spaces of the NLSM. Indeed, for each FWSM, through Eq. (2.10a), the WPPs can be moved closer or farther away from the origin of momenta by changing the light intensities Λ_j. This degree of freedom can produce two relevant arrangements. A symmetric case, using two identical light intensities $\Lambda_\mathrm{U} = \Lambda_\mathrm{L}$, where the WPPs of the two FWSMs are coincident, $\bar{p}_\mathrm{U} = \bar{p}_\mathrm{L}$, and an asymmetric case, using different light intensities $\Lambda_\mathrm{U} \neq \Lambda_\mathrm{L}$, where the WPPs of the two FWSMs are separated, $\bar{p}_\mathrm{U} \neq \bar{p}_\mathrm{L}$. Figure 2.2 shows the density plots of the energy dispersion of the interface states as a function of the momentum components p_x and p_y, in the symmetric case, in panel (a), and the asymmetric case, in panel (b). In Fig. 2.2 (a), where $\Lambda_\mathrm{U} = \Lambda_\mathrm{L} = 3$, the interface states are well defined in the whole 2D momentum space with the exception of the $p_y = 0$ axis (solid white line). Along the $p_y = 0$ axis, for each p_x the electronic band composed of the interface states merges into the bulk conduction (valence) band at the energy $E = +|\bar{p}^2 - p_x^2|$ ($E = -|\bar{p}^2 - p_x^2|$). In Fig. 2.2 (b), where $\Lambda_\mathrm{U} = 2$ and $\Lambda_\mathrm{L} = 3$, the interface states are delimited by solid (dashed) boundary lines, which are the solutions of $\bar{\mu}_\mathrm{U} = 0$ ($\bar{\mu}_\mathrm{L} = 0$). In particular, at the red (blue) boundary lines the interface band merges into a conduction (valence) bulk band. The Fermi line, black line in Fig. 2.2 (b), is composed of a circumference that surrounds the origin of momenta and two segments that lay along the $p_y = 0$ axis. The intersections of the segments and the circumference of the Fermi line correspond to two saddle points.

The appearance of the saddle points at the Fermi energy leads to a Van Hove singularity in the density of interface states (DOS) [235]. Thus, starting from the dispersion relation of the interface states, we write the corresponding DOS as

$$\rho\left(\mathcal{E}\right) = \int \frac{d\boldsymbol{p}_\perp}{\left(2\pi\right)^2} \delta\left(\mathcal{E} - \mathcal{E}\left(\boldsymbol{p}_\perp\right)\right), \tag{2.25}$$

where $\delta(x)$ is the Dirac delta function. In the symmetric case, setting the opposite polarizations $\phi_\mathrm{U} = \pi$ and $\phi_\mathrm{L} = 0$ in Eq. (2.24), the energy dispersion simplifies into the following quadratic form

$$\mathcal{E}\left(\boldsymbol{p}_\perp\right) = \mathrm{sgn}\left(p_y\right) \left[\bar{p}^2 - \left|\boldsymbol{p}_\perp\right|^2\right]. \tag{2.26}$$

From Eq. (2.26) it is straightforward to obtain an analytical expression for the DOS

$$\rho(\mathcal{E}) = \frac{1}{8\pi} \left[\Theta\left(-\mathcal{E} + \bar{p}^2\right) + \Theta\left(\mathcal{E} + \bar{p}^2\right)\right], \tag{2.27}$$

which is shown in Fig. 2.3 (a). Figure 2.3 (b) displays the DOS, computed numerically, in the asymmetric case, where a Van Hove singularity appears at the Fermi energy $\mathcal{E} = 0$. A Van Hove singularity always appears in the DOS when $\Lambda_\mathrm{U} \neq \Lambda_\mathrm{L}$, independently of the specific values of Λ_U

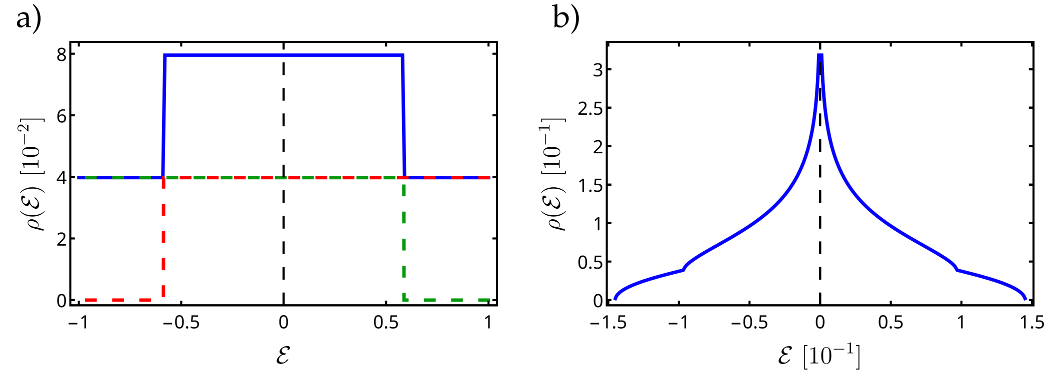

Figure 2.3: Density of interface states as a function of the energy $\mathcal{E}$, shown in the blue line in both panels. Panels (a) refers to the symmetric case ($A_{\mathrm{U}} = A_{\mathrm{L}} = 3$), where the supplemental dashed red [green] line corresponds to the contribution $\Theta\left(\mathcal{E} + \bar{p}^2\right)/(8\pi)$ [$\Theta\left(-\mathcal{E} + \bar{p}^2\right)/(8\pi)$]. Panel (b) refers to the asymmetric case ($A_{\mathrm{U}} = 2$, and $A_{\mathrm{L}} = 3$), where at zero energy a Van Hove singularity occurs. In all panels, we set $u = 1, \Omega = 10$, $\phi_{\mathrm{U}} = \pi$ and $\phi_{\mathrm{L}} = 0$.

and Λ_{L}. Therefore, we have seen that by tuning the intensities of the two beams of light, one can change the WPPs arrangements, generating modifications both in the domain of existence of the interface states and in the shape of the Fermi line. This is the first most important result of this work: one can engineer a Van Hove singularity in a 2D interface electron system by illuminating a NLSM with two beams of lights of different intensities and opposite polarizations.

2.3.2 Pseudo-spin texture

Here, we analyze the pseudo-spin texture of the interface eigenstates, which gives further information on the topological nature of the interface system. For each interface eigenstate, labeled by $\boldsymbol{p}_\perp$, we define the corresponding pseudo-spin vector as

$$\langle\sigma\rangle_{\boldsymbol{p}_\perp} = \int d\boldsymbol{r}\Psi^\dagger_{\boldsymbol{p}_\perp}(\boldsymbol{r})\sigma\Psi_{\boldsymbol{p}_\perp}(\boldsymbol{r}), \tag{2.28}$$

where $\Psi_{\boldsymbol{p}_\perp}(\boldsymbol{r})$ is the wavefunction expressed in spinorial form, accordingly to Eq. (2.19). In the symmetric case ($A_{\mathrm{U}} = A_{\mathrm{L}}$) the pseudo-spin

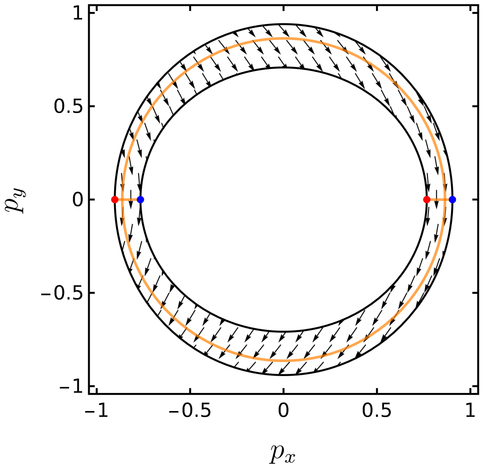

Figure 2.4: Pseudo-spin texture of the interface states in the asymmetric case ($\Lambda_{\mathrm{U}} \neq \Lambda_{\mathrm{L}}$), which shows a trivial structure with zero winding number. The orange solid line represents the Fermi line $\mathcal{E} = 0$, and the red and blue dots denote the WPPs of positive and negative chirality, respectively. The parameters used are: $u = 1, \Omega = 10$, $\Lambda_{\mathrm{U}} = 2, \Lambda_{\mathrm{L}} = 3$, $\phi_{\mathrm{U}} = \pi$, and $\phi_{\mathrm{L}} = 0$.

texture has a trivial pattern. Here, the pseudo-spins are all aligned along the x-direction, i.e. $\langle \boldsymbol{\sigma} \rangle_{\boldsymbol{p}_\perp} = \left(\mathrm{sgn}\left(\lambda p_y\right), 0, 0\right)$. In the asymmetric case ($A_{\mathrm{U}} \neq A_{\mathrm{L}}$) the domain of existence of the interface states is homeomorphic to an annulus (see Fig. 2.2 (b)), and we characterize the topological properties of the interface system by focusing on the generic closed paths that cannot be shrunk into points. In particular, we calculate the winding number [167], which is defined for any closed path Γ parametrized by $\tau \in [0, 1]$ as

$$\nu\left(\Gamma\right) = \frac{1}{2\pi} \int_0^1 \left(\langle \boldsymbol{\sigma} \rangle_{\boldsymbol{p}_\perp}\left(\tau\right) \times \frac{d}{d\tau} \langle \boldsymbol{\sigma} \rangle_{\boldsymbol{p}_\perp}\left(\tau\right) \right)_z d\tau, \tag{2.29}$$

where $\langle \boldsymbol{\sigma} \rangle_{\boldsymbol{p}_\perp}\left(\tau\right)$ is the interface states' pseudo-spin of Eq. (2.28) calculated at the momentum $\boldsymbol{p}_\perp$ corresponding to the parametric variable τ along the curve Γ. A nonzero integer ν corresponds to $|\nu|$-complete rotations of the pseudo-spin, namely a topologically nontrivial pseudo-spin texture. Figure 2.4 shows the pseudo-spin pattern within the domain of existence of the interface states in the asymmetric case, and the orange solid line represents the Fermi line $\mathcal{E}(\boldsymbol{p}_\perp) = 0$. Along the circumference at zero energy shown in Fig. 2.4 and parametrized by $(p_x, p_y) = R(\cos(\theta), \sin(\theta))$, where $R = \sqrt{\left(\lambda_U \bar{p}_L^2 - \lambda_L \bar{p}_U^2\right) / (\lambda_U - \lambda_L)}$, we obtain

$$\langle \sigma \rangle_{\boldsymbol{p}_\perp} \propto \left(\lambda_{\mathrm{U}} R \sin\theta, R^2 - \bar{p}_{\mathrm{U}}^2, 0\right). \tag{2.30}$$

Despite a nonzero y-component, along this circular path, the pseudo-spin texture does not make a full rotation, and the winding number is zero. Hence, independently of values of the light intensities, the pseudo-spin texture is topologically trivial.

2.4 Magnetic barrier

In this section, we introduce a delta-like magnetic barrier along the interface between the two FWSM regions, and we analyze how this additional term can induce a non-trivial pseudo-spin texture. Firstly, we study the modifications in the interface states of the setup in Fig. 2.1 by adding the following magnetic barrier [305]

$$\boldsymbol{B}(\boldsymbol{r}) = B_0 \delta(z) \hat{y}, \tag{2.31}$$

where we remind that all lengths are measured in units of $1/b$. Within our formalism, we introduce the effect of the magnetic field by resorting to the Peierls substitution $\boldsymbol{p} \to \boldsymbol{p} + e\boldsymbol{A}_0/b$, where the vector potential $\boldsymbol{A_0}$ generates the magnetic field through the definition $\boldsymbol{B} = b\nabla_{\boldsymbol{r}} \times \boldsymbol{A}_0$, and it is expressed as

$$\boldsymbol{A}_0(\boldsymbol{r}) = \frac{B_0}{2b} \operatorname{sgn}(z) \hat{x}. \tag{2.32}$$

For each half-space, the FWSM Hamiltonian of Eq. (2.12) is rewritten as

$$\begin{aligned} \mathcal{H}_j(\boldsymbol{p}) = \Big\{ \bar{p}_j^2 - \Big[(p_x - \zeta_j p_0)^2 + p_y^2 \Big] \Big\} \sigma_x \\ + \lambda_j p_y \sigma_y + u p_z \sigma_z, \end{aligned} \tag{2.33}$$

where $j \in \{\mathrm{L}, \mathrm{U}\}$, $p_0 = -eB_0/(2b^2)$, $\bar{p}_j$ and λ_j are defined in Eqs. (2.13), and $\zeta_{\mathrm{U}} = +1$ and $\zeta_{\mathrm{L}} = -1$. In each FWSM the WPs are placed at $\boldsymbol{P}_{j,\pm} =$

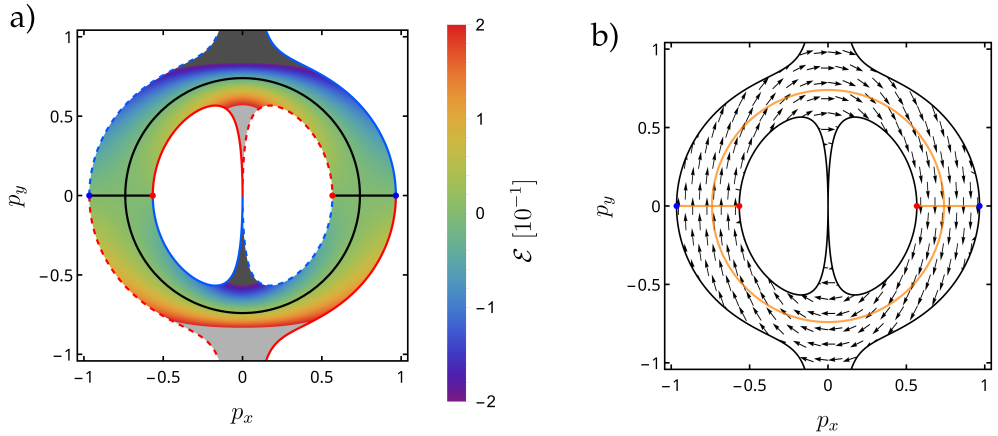

Figure 2.5: (a) Density plot of the energy dispersion, and (b) pseudo-spin texture plot of the interface states as a function of the momentum components p_x and p_y, with $\Lambda_{\mathrm{U}} = \Lambda_{\mathrm{L}}$ and in the presence of a delta-like magnetic field at $z = 0$. In panel (a), the boundary solid (dashed) lines represent the merging of the interface states' band with the upper (lower) FWSM bulk eigenbands. The red (blue) lines describe the merging into the conduction (valence) band, and red and blue dots represent WPPs of positive and negative chirality, respectively. Positive (negative) out of range values are depicted as light (dark) gray areas, and the Fermi line $\mathcal{E} = 0$ is shown in black in panel (a) and in orange in panel (b). The parameters used are: $u = 1, \Omega = 10$, $\Lambda_{\mathrm{U}} = \Lambda_{\mathrm{L}} = 3$, $\phi_{\mathrm{U}} = \pi$, $\phi_{\mathrm{L}} = 0$, and the magnetic parameter is set at $p_0 = 1/5$.

$\left(\pm\bar{p}_j + \zeta_j p_0, 0, 0\right)$. The magnetic term p_0 induces a rigid shift of each pair of WPs along the x-direction of the 2D momentum space. Hence, the intensity of the delta-like magnetic field, parametrized by p_0, represents a further knob for modifying the WPPs of the FWSMs, in addition to the intensities and polarizations of the beams of light. Here, we see how this further degree of freedom can enrich the energy dispersion and alter the structure of the pseudo-spin pattern. For sake of simplicity, we consider the symmetric case ($\Lambda_{\mathrm{U}} = \Lambda_{\mathrm{L}} = \Lambda$, $\phi_{\mathrm{U}} = \pi$, and $\phi_{\mathrm{L}} = 0$), where the dispersion relation assumes the following compact expression

$$\mathcal{E}\left(\boldsymbol{p}_{\perp}\right)=p_y\Lambda^2\frac{1-\frac{e^2\Lambda^2}{2}-\left(p_x^2+p_y^2+p_0^2\right)}{\sqrt{\left(\frac{\Omega}{u}\right)^2\left(p_xp_0\right)^2+\left(\Lambda^2p_y\right)^2}}. \tag{2.34}$$

Figure 2.5 (a) shows the density plot of the dispersion relation for this symmetric case. Like in the asymmetric case without magnetic barrier, there are two saddle points in the Fermi line (black line in Fig. 2.5 (a)) which cause the appearance of a Van Hove singularity in the DOS. Moreover, in Fig. 2.5 (a), the solid (dashed) boundary lines are solutions of the delocalization condition $\bar{\mu}_{\mathrm{U}}=0$ ($\bar{\mu}_{\mathrm{L}}=0$), where

$$\bar{\mu}_j=\frac{1}{u}\sqrt{\left\{\bar{p}_j^2-\left[(p_x-\zeta_jp_0)^2+p_y^2\right]\right\}^2+\left(\lambda_jp_y\right)^2-\mathcal{E}^2}, \tag{2.35}$$

and red (blue) lines describe the merging of the band composed by the interface states into a conduction (valence) bulk band. Besides a modification of the energy dispersion relation, the presence of the delta-like magnetic field has a strong impact on the pseudo-spin texture. Figure 2.5 (b) displays the pseudo-spin pattern within the domain of existence of the interface states in the symmetric case, and the orange solid line represents the Fermi line $\mathcal{E}(\boldsymbol{p}_{\perp})=0$. Along the circumference at zero energy shown in Fig 2.5 (b) and parametrized by $(p_x,p_y)=\bar{R}(\cos(\theta),\sin(\theta))$, where $\bar{R}=\sqrt{\bar{p}^2-p_0^2}$, we obtain

$$\langle\boldsymbol{\sigma}\rangle_{\boldsymbol{p}_{\perp}}\propto\left(\lambda\sin\theta,-2p_0\cos\theta,0\right), \tag{2.36}$$

where $\bar{p}$ and λ are defined in Eqs. (2.10). In this case, the pseudo-spin pattern has a nontrivial structure. In fact, along this closed path, the pseudo-spin makes a complete rotation, and we find a non-vanishing winding number $\nu=+1$, where the sign $+$ is given by the counterclockwise rotation of the pseudo-spin. This is the second most important result of this work: the presence of a magnetic barrier along the interface between the two FWSM regions can induce a nontrivial topology in the pseudo-spin pattern. Specifically, the pseudo-spin structure is nontrivial under the condition

$$\left|\bar{p}_{\mathrm{U}}-\bar{p}_{\mathrm{L}}\right|<2\left|p_0\right|<\bar{p}_{\mathrm{U}}+\bar{p}_{\mathrm{L}}\ , \tag{2.37}$$

where $\bar{p}_j$ is defined by Eq. (2.13a). For any given magnetic parameter $|p_0| < 1$, by choosing suitable values of the light intensities, it is possible to set the values of $\bar{p}_{\mathrm{U}}$ and $\bar{p}_{\mathrm{L}}$ such that they fulfill the conditions of Eq. (2.37). By conveniently tuning the light intensities, one can also set the values of $\bar{p}_{\mathrm{U}}$ and $\bar{p}_{\mathrm{L}}$ such that the inequalities in Eq. (2.37) are not satisfied. Hence, in the presence of the magnetic barrier, it is possible to switch the topological properties of the interface states by only modulating the light intensities. We note that the condition in Eq. (2.37) can be interpreted in terms of the WPPs arrangement. In particular, both inequalities of Eq. (2.37) are satisfied if the inner (outer) WPPs have identical chiralities, an example is shown in Fig. 2.5. In the previous section, we have verified that this type of arrangement of the WPPs is not reachable by exploiting only the light beams, and for this reason, the assistance of the local magnetic field is crucial.

Finally, we analyse the effects of a magnetic barrier which has a field component also along the x direction. The magnetic barrier can be written as

$$\boldsymbol{B}\left(\boldsymbol{r}\right) = \delta(z)\left(B_{0,x}\hat{x} + B_{0,y}\hat{y}\right) \tag{2.38}$$

which, after the Peierls substitution, leads for each half-space $j \in \{\mathrm{L}, \mathrm{U}\}$ to the FWSM Hamiltonian

$$\begin{aligned}\mathcal{H}_j\left(\boldsymbol{p}\right) = &\left\{\bar{p}_j^2 - \left[\left(p_x - \zeta_j p_{0,x}\right)^2 + \left(p_y - \zeta_j p_{0,y}\right)^2\right]\right\}\sigma_x \\ &+ \lambda_j\left(p_y - \zeta_j p_{0,y}\right)\sigma_y + u p_z \sigma_z,\end{aligned} \tag{2.39}$$

where $\left(p_{0,x}, p_{0,y}\right) = \left(-eB_{0,y}/(2b^2), eB_{0,x}/(2b^2)\right)$, $\zeta_U = +1$ and $\zeta_L = -1$, and $\bar{p}_j$ and λ_j are still given by Eqs. (2.13). Figures 2.6 (a) and 2.6 (b) show the energy dispersion and pseudo-spin texture, respectively, of the interface system, derived from the Hamiltonian of Eq. (2.39) when the x and y component of the magnetic barrier are equal in strengths, $p_{0,x} = p_{0,y}$. The meaning of lines and dots is the same as in Fig. 2.5. It can be seen from Fig. 2.6 (b) that the pseudo-spin texture is still non-trivial and all paths which enclose the origin of momenta will have a non vanishing winding number. For higher x components of the magnetic barrier, roughly for $p_{0,y} \gtrsim 2p_{0,x}$, the domain of existence of the interface states is no longer connected, and we cannot properly define its topology through the winding number of Eq. (2.29). The DOS of the interface system is also slightly

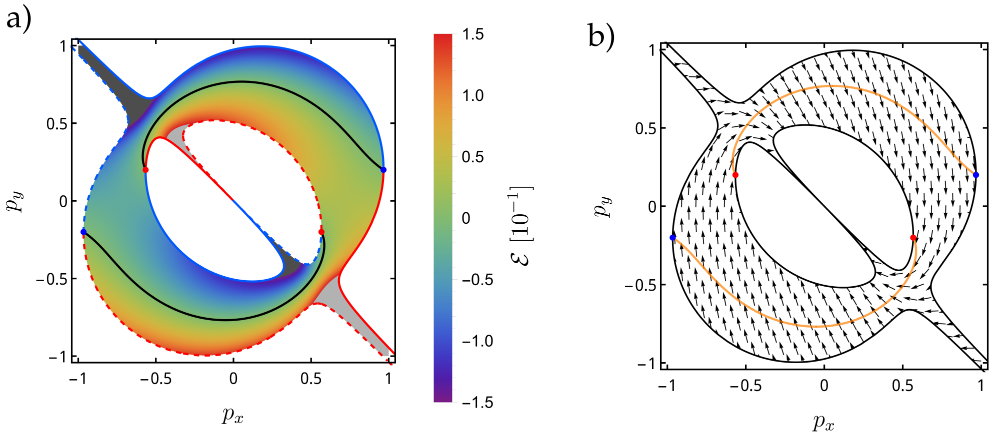

Figure 2.6: (a) Density plot of the energy dispersion, and (b) pseudospin texture plot of the interface states as a function of the momentum components p_x and p_y, with $\Lambda_{\mathrm{U}} = \Lambda_{\mathrm{L}}$ and in the presence of a delta-like magnetic field at $z = 0$ with components both along the x and y directions. In panel (a), the boundary solid (dashed) lines represent the merging of the interface states' band with the upper (lower) FWSM bulk eigenbands. The red (blue) lines describe the merging into the conduction (valence) band, and red and blue dots represent WPPs of positive and negative chirality, respectively. Positive (negative) out of range values are depicted as light (dark) gray areas, and the Fermi lines $\mathcal{E} = 0$ are shown in black in panel (a) and in orange in panel (b). The parameters used are: $u = 1, \Omega = 10$, $\Lambda_{\mathrm{U}} = \Lambda_{\mathrm{L}} = 3$, $\phi_{\mathrm{U}} = \pi$, $\phi_{\mathrm{L}} = 0$, and the magnetic parameters are set at $p_{0,x} = 1/5$ and $p_{0,y} = 1/5$.

affected. In particular, the Van Hove singularity at the Fermi energy is split into two energy symmetric ones. The energies of these new Van Hove singularities is numerically found to be linearly proportional to the strength of the x component of the magnetic field, $\mathcal{E}_{\mathrm{VHS}} \sim \pm p_{0,y}$ (up to a maximum value, with the given parameters, $p_{0,y} \gtrsim 3.5 p_{0,x}$, after which they no longer exist).

2.5 Conclusions

In this chapter, we analyzed the boundary states that emerge at the interface between two sides of an infinite NLSM that are illuminated by monochromatic light beams of opposite circular polarizations. In particular, we focused on the energy dispersion, DOS, and pseudo-spin texture.

Illuminating the system with lights of opposite polarization generates two FWSMs with opposite Chern numbers, and this topology mismatch leads to the appearance of topological interface states. We have shown that the topological properties of the interface states strictly depend to the relative arrangements of the WPPs of the two induced WSMs. The independent tunability of the light intensities represents a knob for modifying this relative arrangement. As such, by changing the intensities of the light beams one can modify the domain of existence of the interface states along the 2D reciprocal space, and the shape of the Fermi line. In particular, illuminating the system with two different light intensities induces a transition in the Fermi line with the creation of a Van Hove singularity in the DOS.

Moreover, we have added a further knob for modifying the interface states, namely we have introduced a magnetic barrier along the interface given, for instance, by localized doping with magnetic impurities. The presence of this local magnetic field together with the tunability of the light intensity allows to change the relative arrangement of WPPs at will. We have thus found that the y component of this magnetic barrier can lead to the creation of a novel non-trivial pseudo-spin pattern of the interface states. The x component, on the other hand, works against the non-trivial topology of the interface system; nonetheless, the system has a fair degree of robustness, roughly up to $B_x \lesssim 2B_y$ in the setup studied. In this work, we have classified the topology of the interface system in terms of the winding of the pseudo-spin around the origin of momenta, and we have shown that by modulating the light intensities it is possible to switch on/off the non-trivial topology.

Together with the presence of VHSs close to the Fermi level, the discovered tunable topological interface state could provide promising applications in the search for exotic correlated quantum phases of matter and for optoelectronics.

Chapter 3

Spin-Orbit Coupling effects in a Graphene Josephson Junction

In this chapter, we study the CPR through a ballistic GJJ, in which the central scattering region of graphene layer is subjected to the SOC interaction by proximity effect. We focus on the short and wide junction limits, in which the junction length is much smaller than the coherence length, ξ, of the superconductors. We employ an analytical approach and use a low-energy description of graphene based on the continuum Hamiltonian [191]. Using the transfer matrix formalism, we compute the transmission probabilities through the junction and directly link them to the CPR [173, 268–270, 306, 307]. The results focus on the critical current and skewness of the CPR as a function of the chemical potential, showing the effects of KM-SOC, VZ-SOC, and R-SOC, and the onsite scalar potential. We find that, depending on the modifications of the band structure, these different terms result in a wide range of effects on the CPR of the junction. Some of them, such as the on-site potential and the KM-SOC, drastically reduce both the critical current and the skewness. Others, such as the VZ-SOC act as a spin-valley-polarized chemical potential, increasing both the critical current and the skewness. Interestingly, the R-SOC, while having little effect on the critical current of the CPR, produces heavy swings in its skewness, allowing for a tunable harmonic content.

The results of this chapter are published by F. Bonasera, G. A. Falci, E. Paladino, and F. M. D. Pellegrino in *Current phase relation in a planar*

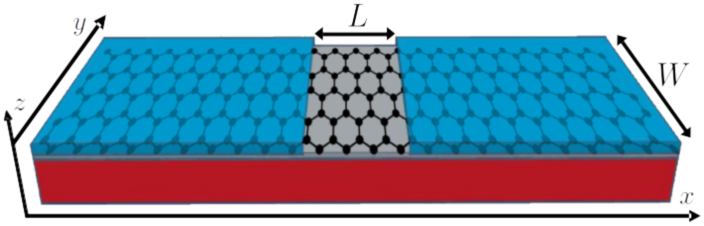

Figure 3.1: Schematic of the system. A GJJ consists of a graphene layer (gray) placed on top of a substrate (red) with superconducting leads (blue) covering the $|x| > L/2$ regions.

graphene Josephson junction with spin–orbit coupling, Eur. Phys. J. Spec. Top. (2025) [239].

This Chapter is organized as follows. In Sec. 3.1, we introduce the continuum Hamiltonian of the inner graphene region, it is the one we have already discussed in Sec. 1.5.3 with a slight rotation of the axis. We also introduce the transfer matrix formalism, which we use to compute the transmissions through the junction, together with the formulae that link them to the CPR of the system. In Sec. 3.2 we present the results of the study. First, we show the cases without R-SOC, which we were able to fully compute analytically; then, when also introducing the R-SOC, we resort to solving the problem numerically and show the results for some of the most experimentally relevant parameter values. Finally, a summary of the work and some final comments are included in Sec. 3.3.

3.1 Model

Figure 3.1 shows a diagram of the system: a gray graphene layer is placed on top of a red substrate, with blue superconducting leads that extend over the areas where $|x| > L/2$. The width of the junction in the y direction is treated as infinite, $W \to \infty$.

To describe the system, we use a step-like profile for the different regions of the junction. The Hamiltonian of the inner region of the junction includes the terms induced by the substrate on the graphene layer, the ones we have discussed in Sec. 1.5.3. When expanded to first order in the momentum $\boldsymbol{k}$ around the Dirac points is given by Eq. (1.56), which we rewrite here for simplicity[1]

$$\begin{aligned}\mathcal{H} = -i\hbar v\left[\tau_z\left(\partial_x\sigma_x\right)+\partial_y\sigma_y\right]-\mu_0+U_z\sigma_z\\ +s_z\tau_z\left(\lambda_{\mathrm{KM}}\sigma_z+\lambda_{\mathrm{VZ}}\right)-\lambda_{\mathrm{R}}\left(s_y\tau_z\sigma_x+s_x\sigma_y\right),\end{aligned} \tag{3.1}$$

it acts on an 8-dimensional spinorial space in which $\boldsymbol{\sigma}$, $\boldsymbol{\tau}$ and $\boldsymbol{s}$ are the three Pauli matrices that describe the sublattice (A, B), valley $(\boldsymbol{K}, -\boldsymbol{K})$ and spin z projection $(\uparrow, \downarrow)$ degrees of freedom, respectively. In Eq. (3.1), μ_0 is the Fermi level of the graphene layer, U_z represents the intensity of the staggered onsite scalar potential on the A, B sublattices, λ_{KM} denotes the intensity of the KM-SOC [4,19], λ_{VZ} refers to the strength of the VZ-SOC, and λ_{R} represents the magnitude of the R-SOC.

We focus on the short junction limit, $L \ll \xi \sim \hbar v/\Delta_0$, where ξ is the coherence length of the superconductors and Δ_0 is the superconducting gap parameter. As we have discussed in Sec. 1.6.3, in the short junction regime, the supercurrent is essentially carried by ABSs, at energies $\left|E_p\right| < \Delta_0$, which are localized in the inner region of the junction [173, 268, 269]. Since our setup is time-reversal symmetric, we can apply Eq. (1.84) in order to link the ABSs energy to the transmission probability, $\mathcal{T}_p$, of normal electrons passing through a ballistic graphene stripe. We can then use Eq. (1.81) to evaluate the CPR of the junction.

Based on Eq. (1.84), we calculate the normal-state transmission amplitude, $\mathcal{T}_p$, as a function of the SOC terms. For this aim, we start from the setup in Fig. 3.1 by considering lateral leads in the normal metallic limit and follow the same procedure as in Refs. [306, 307]. We solve the stationary Schrödinger equation in all three regions and ensure that the wave function is continuous throughout the device [308,309]. Specifically, we apply the transfer matrix method within the central region to enforce wave function matching. Using periodic boundary conditions along the y-direction, we write the generic eigenfunction, labeled by the wavevector k and the energy E, in the central region as

$$\psi_{k,E}\left(x,y\right) = e^{iky}T\left(k,E;x\right)\tilde{\psi}_{k,E}\left(-L/2\right)\ , \tag{3.2}$$

---

[1] This equation is not exactly the same as Eq. (1.56) because it describes a graphene sheet with a different alignment: it is rotated by $\pi/2$ with respect to the previous one.

where the evolution matrix T satisfies the equation below

$$\begin{aligned}\frac{dT\left(k,E;x\right)}{dx} &= \frac{\mathcal{A}}{\hbar v}T\left(k,E;x\right), \\ \mathcal{A} &\equiv i[\left(\mu_0+E\right)\tau_z-\lambda_{\mathrm{VZ}}s_z]\sigma_x-[\lambda_{\mathrm{KM}}s_z+U_z\tau_z]\sigma_y \\ &\quad+\lambda_{\mathrm{R}}\left(is_y-s_x\tau_z\sigma_z\right)+\hbar vk\tau_z\sigma_z, \end{aligned} \tag{3.3}$$

which, together with the condition $T\left(k,E,-L/2\right)=1$, has the formal solution

$$T\left(k,E;x\right)=\exp\left[\frac{\mathcal{A}}{\hbar v}\left(x+L/2\right)\right]. \tag{3.4}$$

In a GJJ, the typical energy scale for the ABSs is $E\sim\Delta_0$, and in the short junction regime $\Delta_0\ll L/(\hbar v)$, so we can focus on $\mathbb{T}\left(k;x\right)=T(k,0;x)$, as explained also in Sec. 1.6.3.

In the presence of metallic leads, the evolution matrix is related to the transfer matrix by [306,307]

$$M(k)=\mathcal{Q}^{-1}\mathbb{T}(k,L/2)\mathcal{Q}, \tag{3.5}$$

with $\mathcal{Q}=\frac{1}{\sqrt{2}}\left(\sigma_x+\sigma_z\right)$. Moreover, the elements of the transfer matrix are linked to those of the scattering matrix across the region as

$$M(k)=\begin{pmatrix}\left(t_{12}^{\dagger}\left(k\right)\right)^{-1} & r_{22}\left(k\right)\left(t_{21}\left(k\right)\right)^{-1} \\ -r_{11}\left(k\right)\left(t_{21}\left(k\right)\right)^{-1} & \left(t_{21}\left(k\right)\right)^{-1},\end{pmatrix}, \tag{3.6}$$

with $t_{ij}\left(k\right)$ $\left(r_{ii}\left(k\right)\right)$ the transmission (reflection) amplitude matrix from lead i to lead j (i). The transmission probabilities are then found as the eigenvalues of the Hermitian matrix $t_{12}^{\dagger}\left(k\right)t_{12}\left(k\right)$.

3.2 Bulk current-phase relation

In this Section we show the results for the supercurrent flowing through the GJJ.

Firstly, we neglect the R-SOC, setting $\lambda_{\mathrm{R}}=0$. This simplification allows us to handle the transfer matrix analytically, thereby clarifying the influence of the KM-SOC and VZ-SOC terms on the supercurrent. In the last part of this section, we incorporate the R-SOC and tackle the problem using numerical methods [310].

In the absence of λ_{R}, the spin z projection and the valley index are good quantum numbers. So, Eq. (3.3) can be expressed for the 4-dimensional spin-valley subspaces as

$$\frac{d\mathbb{T}_{s\tau}(k;x)}{dx} = \tau\left[i\alpha_{s\tau}\sigma_x - \gamma_{s\tau}\sigma_y + k\sigma_z\right]\mathbb{T}_{s\tau}(k;x), \tag{3.7}$$

where the s (τ) index takes on the values $s \in \{+,-\}$ ($\tau \in \{+,-\}$), corresponding to the spin z-component (valley) $\uparrow$ and $\downarrow$ ($\boldsymbol{K}$ and $\boldsymbol{K}'$), respectively. We also defined the following renormalized parameters

$$\alpha_{s\tau} = \frac{\mu_0 - s\tau\lambda_{\mathrm{VZ}}}{\hbar v}, \tag{3.8a}$$

$$\gamma_{s\tau} = \frac{U_{\mathrm{Z}} + s\tau\lambda_{\mathrm{KM}}}{\hbar v}, \tag{3.8b}$$

which depend on the s and τ indices by their product $s\tau$. For each couple of s and τ, we solve Eq. (3.7) in the following close analytical form

$$\begin{aligned}\mathbb{T}_{s\tau}(k;x) = {} & \cos\left[q_{s\tau}(x+L/2)\right] \\ & + \tau\frac{\sin\left[q_{s\tau}(x+L/2)\right]}{q_{s\tau}}\left(i\alpha_{s\tau}\sigma_x + i\gamma_{s\tau}\sigma_y + k\sigma_z\right),\end{aligned} \tag{3.9}$$

with

$$q_{s\tau} = \sqrt{\alpha_{s\tau}^2 - \gamma_{s\tau}^2 - k^2}. \tag{3.10}$$

Using Eqs. (3.6), we can then find the transmission probabilities as the eigenvalues of the Hermitian matrix $t_{12}(k)\,t_{12}^{\dagger}(k)$, which are expressed as

$$\mathcal{T}_{s\tau}(k) = \frac{\alpha_{s\tau}^2 - \left(k^2+\gamma_{s\tau}^2\right)}{\alpha_{s\tau}^2 - \left(k^2+\gamma_{s\tau}^2\right)\cos^2\left[L\sqrt{\alpha_{s\tau}^2 - \left(k^2+\gamma_{s\tau}^2\right)}\right]}, \tag{3.11}$$

Finally, using Eqs. (1.81) and (1.84), we obtain the supercurrent carried by the ABSs as

$$\begin{aligned} I(\phi) &= \frac{2e\Delta_0}{\hbar}\sum_{k,s,\tau}\frac{\mathcal{T}_{s\tau}(k)\sin\phi}{4\sqrt{1-\mathcal{T}_{s\tau}(k)\sin^2(\phi/2)}} \\ &= \frac{2e\Delta_0}{h}W\sum_{s,\tau=\pm}\int dk\frac{\mathcal{T}_{s\tau}(k)\sin\phi}{4\sqrt{1-\mathcal{T}_{s\tau}(k)\sin^2(\phi/2)}},\end{aligned} \tag{3.12}$$

where in the last line we have considered the wide junction limit ($W \to \infty$), namely the sum over k is replaced by an integral $\sum_k \to W/2\pi \int dk$.

The results shown in Eqs.(3.11) and (3.12) are formally equivalent to those found for a short JJ based on intrinsic graphene [308,311], provided the following replacements

$$\frac{\mu_0}{\hbar v} \to \alpha_{s\tau}, \tag{3.13a}$$

$$k^2 \to k^2 + \gamma_{s\tau}^2. \tag{3.13b}$$

In particular, λ_{VZ} determines the parameter $\alpha_{s\tau}$, which works as an effective Fermi level for the spin-valley interaction. Moreover, λ_{KM} and U_z determine the $\gamma_{s\tau}$ parameter, which creates an effective spin-valley gap. A non-zero value of $\gamma_{s\tau}$ disrupts Klein tunneling at $k = 0$ [173,312] and can significantly decrease the total supercurrent passing through the junction for small values of $|\mu_0|$. In particular, both U_z and λ_{KM} independently open the same size gap in graphene and have the same effect on the transmission probability of Eq. (3.11), which depends quadratically on $\gamma_{s\tau}$. The difference between the two terms is that λ_{KM} opens an inverted (topological) gap, meaning that the conduction band has a different A, B sublattice polarization at the two Dirac points; see Eq. (3.1) and the discussions in Sec. 1.5.3 [4,19,131,191]. For this reason, when they are both present, their effect is enhanced in one spin-valley subspace, while it is decreased in the other one, as can be seen from the expression of $\gamma_{s\tau}$ in Eq. (3.8a). The competition between these two terms is not trivial, and it was also recently used in bilayer graphene (where U_z comes from the difference between the chemical potentials of the upper and lower layers) to probe its topological state [313].

To characterize the equilibrium supercurrent, $I(\phi)$, flowing through the junction, we use the critical current, defined as its maximal value

$$I_{\mathrm{c}} = \max_{\phi} I(\phi). \tag{3.14}$$

For any given set of microscopic parameters, from the definition above, we call $\phi_{\max}$ the corresponding phase difference that maximizes the supercurrent, and we define the supercurrent skewness as

$$S \equiv \frac{2\phi_{\max} - \pi}{\pi}, \tag{3.15}$$

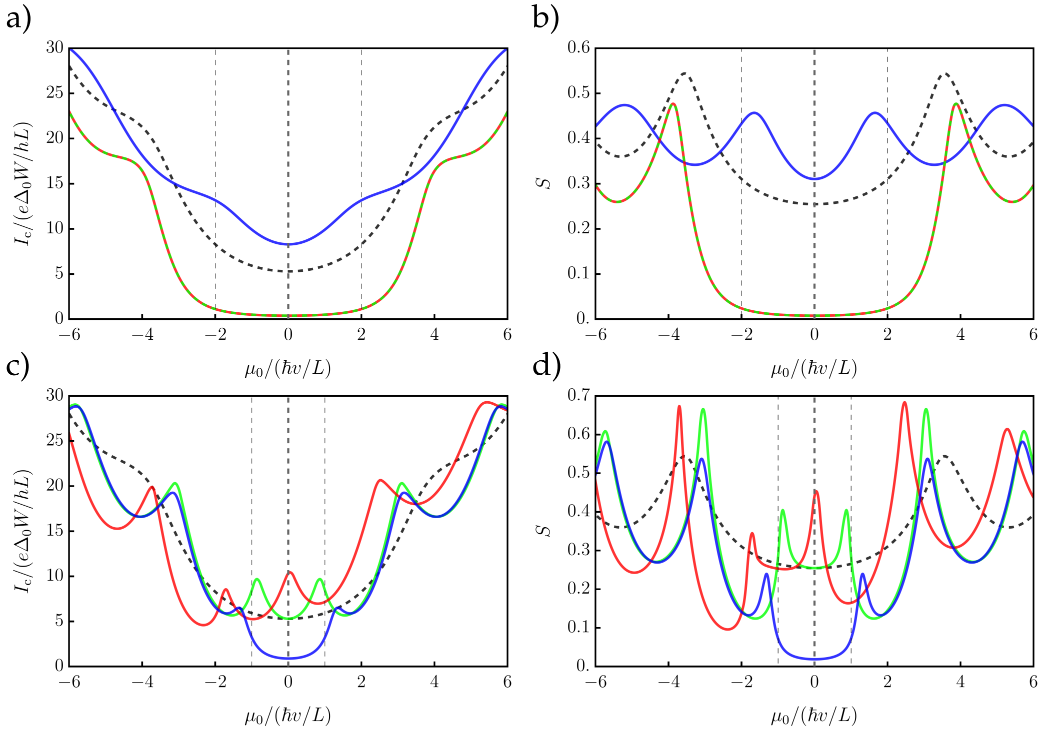

Figure 3.2: a) critical current I_c and b) skewness S, as a function of the chemical potential μ_0 for each substrate-induced term independently, when $\lambda_R = 0$. For reference, dashed black refers to the intrinsic case (substrate-independent terms). Solid lines consider the effect of the VZ-SOC $\lambda_{VZ} = 2\hbar v/L$ (blue), and of the KM-SOC $\lambda_{KM} = 2\hbar v/L$ (red). The dashed green line denotes the case with the staggered onsite potential $U_z = 2\hbar v/L$. c) critical current I_c and d) skewness S, as a function of the chemical potential μ_0 for different parameter sets given a non-zero λ_R. Again, the dashed black line denotes the intrinsic case for reference, the solid green line denotes the effect of a high R-SOC, $\lambda_R = 5\hbar v/L$, the solid blue one the case with a strong Rashba and a smaller VZ-SOC, $\lambda_R = 5\hbar v/L, \lambda_{VZ} = \hbar v/L$, and the solid red one that with a strong R-SOC and a smaller KM-SOC, $\lambda_R = 5\hbar v/L, \lambda_{KM} = \hbar v/L$. All the energy parameters are scaled in units of $\hbar v/L$ and the critical current is in units of $e\Delta_0 W/(hL)$.

which quantifies the deviation from a sinusoidal CPR.

To keep the junction dimensions general, in the following, the inverse length $1/L$ is used to scale the wavenumber k, $\hbar v/L$ is used as the energy scale unit, while the critical current, I_c, is considered in units of $(e\Delta_0 W/hL)$. Fig. 3.2 shows the results for a) the critical current I_c and b) the skewness S, as a function of the chemical potential μ_0, when $\lambda_R = 0$. The dashed black line represents intrinsic graphene, where all substrate-induced parameters are set to zero. The other lines refer to the case with a single non-zero substrate-induced parameter: for the solid blue line, we set $\lambda_{VZ} = 2\hbar v/L$, for the solid red one $\lambda_{KM} = 2\hbar v/L$, and, finally, for the dashed green one $U_z = 2\hbar v/L$. In particular, Figs. 3.2 a) and b) clearly show that the gap opening due to the terms U_z and λ_K, in the $|\mu_0| \leq |\lambda_{KM}|, |U_z|$ region indicated by the vertical dashed lines, drastically reduces both the critical current and, by eliminating the transparent modes due to Klein tunneling at $k = 0$, also the skewness of the CPR. In addition, a nonzero λ_{VZ} term enhances the critical current when the chemical potential is close to $\mu_0 \approx 0$. Also, because of the form of $\alpha_{s\tau}$ in Eq. (3.8a), the critical current stays approximately constant for $|\mu_0| \lesssim |\lambda_{VZ}|$.

In the second part of this Section, we include a nonzero Rashba SOC, $\lambda_R \neq 0$. Here, the spin z-projection is no longer a good quantum number and is involved in the dynamics. For this reason, with a finite Rashba SOC, we numerically solve Eq. (3.3) for some specific sets of parameters. Recent works suggest that in a graphene monolayer proximitized by a substrate with a large SOC, the R-SOC term is typically the dominant one [137, 138, 226]: the SOCs values are estimated to be $\lambda_R \approx 10 - 15$ meV, $\lambda_{VZ} \approx 1 - 3$ meV and negligible $\lambda_{KM} \approx 0$. Thus, among all the possible combinations of SOC parameters, from now on we focus on a high R-SOC, λ_R, combined with a smaller secondary one of the KM-SOC kind, λ_{KM}, or VZ-SOC one, λ_{VZ}. Figure 3.2 shows c) the critical current and d) the skewness of the supercurrent flowing through the junction with a high Rashba SOC, $\lambda_R = 5\hbar v/L$. In both Figs. 3.2 c) and d), the dashed black line illustrates the scenario for pristine graphene, where all parameters induced by the substrate are zero. The green solid line indicates the setup with only R-SOC $\lambda_R = 5\hbar v/L$, the blue solid line refers to the case with $\lambda_R = 5\hbar v/L$ and a smaller VZ-SOC $\lambda_{VZ} = \hbar v/L$, and the red solid line represents the condition with $\lambda_R = 5\hbar v/L$ and a smaller KM-SOC $\lambda_{KM} = \hbar v/L$. With a typical short junction length of

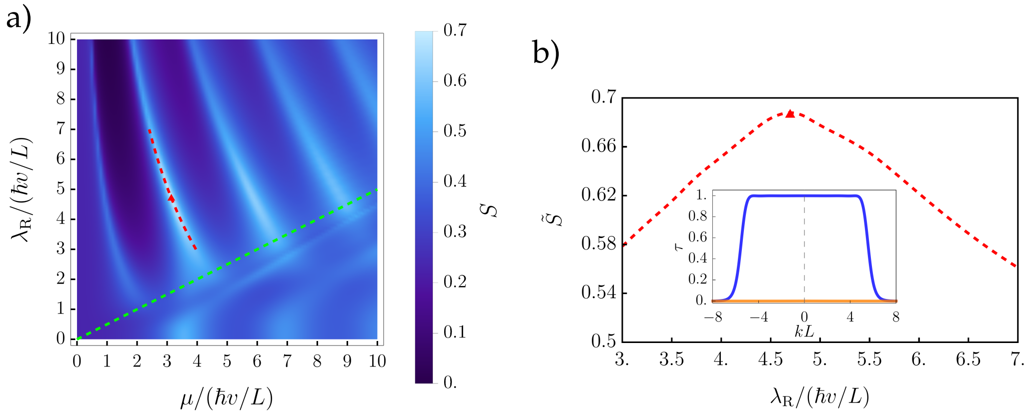

Figure 3.3: a) color map of $S(\lambda_{\mathrm{R}}, \mu_0)$. Here, the green dotted line refers to the condition $\mu_0 = 2\lambda_{\mathrm{R}}$, where the Fermi level coincides with the bottom of the graphene upper band. The red dashed line represents the maximum of the skewness, $\tilde{S}(\lambda_{\mathrm{R}})$, within the range of the R-SOC $\lambda_{\mathrm{R}} \in [3,7]\hbar v/L$. b) maximum skewness, $\tilde{S}(\lambda_{\mathrm{R}})$, as a function of λ_{R}; the global maximum (red triangle) is well visible for the optimal value of $\lambda_{\mathrm{R}\blacktriangle} \approx 4.7\hbar v/L$. The inset shows the peculiar, nearly step-like transmission probability as a function of k occurring at $\lambda_{\mathrm{R}\blacktriangle}$. All energies are scaled in units of $\hbar v/L$ and the wavenumber k is represented in units of $1/L$.

around 100 nm [140], the parameter values used here are thus of the same order of magnitude as what can be expected experimentally. Again, the main features of the critical current stem from the proximitized graphene band structure. A R-SOC term alone modifies the linear band structure of graphene as $E_{\mathrm{G},\eta\eta'} = \eta\lambda_{\mathrm{R}} + \eta'\hbar v\sqrt{k_x^2 + k_y^2 + \lambda_{\mathrm{R}}^2}$, with $\eta, \eta' \in \{+,-\}$, introducing a parabolic dispersion close to the charge neutrality point, with the effect of moving and sharpening the Fabry-Perot resonances, as can be seen from the green line in both Figs. 3.2 c) and d). Including a smaller λ_{VZ} (blue solid line) opens a gap of magnitude $2|\lambda_{\mathrm{VZ}}|$ in the band structure; while including a smaller λ_{KM} shifts the charge neutrality point of graphene at $-\lambda_{\mathrm{KM}}$, as can be seen from the asymmetry of the critical current as a function of μ_0 (red solid line in Fig. 3.2 c)). Note that the splitting of the Dirac points due to the Rashba interaction is a second-order effect in the ratio λ_{R}/t [225], where $t \sim 2.8$ eV is the graphene hopping parameter. For the values of λ_{R}/t that we are considering here, this effect can be safely neglected, even at short junction lengths.

It is noteworthy that the R-SOC, despite not significantly impacting the critical current, produces noticeable swings, compared to the intrinsic case, in the skewness of the supercurrent at low chemical potentials. In particular, it can considerably increase the number of transparent modes, with $\mathcal{T} \approx 1$, within the junction. From Eq. (3.12) we see that, in general, a single mode of low transmission, $\mathcal{T} \ll 1$, contributes to the supercurrent as $I_{\mathcal{T}}(\phi) \propto \mathcal{T} \sin(\phi)$ with vanishing skewness, $S \approx 0$, while a transparent mode, $\mathcal{T} \approx 1$, contributes as $I_{\mathcal{T}}(\phi) \propto \sin(\phi/2)$ with maximum skewness, $S \approx 1$. For a strong R-SOC, this leads to highly pronounced peaks in the skewness of the supercurrent, as illustrated in Fig. 3.2 d). Figure 3.3 a) shows $S(\lambda_{\mathrm{R}}, \mu_0)$ as a function of R-SOC and the chemical potential. Here, the dotted green line represents $\mu_0 = 2\lambda_{\mathrm{R}}$; when the chemical potential μ_0 exceeds $2\lambda_{\mathrm{R}}$, the upper graphene band is involved in conduction, disrupting the distinct resonances typical of the region with lower chemical potentials. Moreover, we define the function $\tilde{S}(\lambda_{\mathrm{R}}) = \max_{\mu_0} S(\mu_0, \lambda_{\mathrm{R}})$, which corresponds to the maximum value of skewness as a function of the chemical potential μ_0 for a fixed value of λ_{R}. In Figure 3.3 a), the red dotted line denotes $\tilde{S}(\lambda_{\mathrm{R}})$ as a function of λ_{R} in the range $[3, 7]\hbar v/L$. In the main plot of Fig. 3.3 b), $\tilde{S}(\lambda_{\mathrm{R}})$ is reproduced within the range $\lambda_{\mathrm{R}} \in [3, 7]\hbar v/L$, and there is a global maximum around $\lambda_{\mathrm{R}\blacktriangle} \approx 4.7\hbar v/L$. The inset of Fig. 3.3 b) shows the nearly step-like transmission probabilities as a function of the momentum k at the value of the chemical potential μ_0 which maximizes the skewness for $\lambda_{\mathrm{R}} = \lambda_{\mathrm{R}\blacktriangle}$. Thus, by influencing λ_{R}, such as through the application of a transverse electric field [135,189,193,194], one can potentially enhance the higher harmonics into the CPR of a wide and ballistic GJJ by increasing its skewness.

3.3 Conclusions

In this Chapter, we studied the current-phase relation in a ballistic GJJ in which the inner graphene layer is subjected to different spin-orbit coupling interactions because of the proximity effect with a substrate. We focused on the short and wide limits, at zero temperature. We found an explicit analytical expression for the combined effects of the onsite scalar potential, Kane-Mele, and valley-Zeeman spin-orbit couplings. This expression for the transmission probabilities can be written in the same form as the intrinsic case with a suitable renormalization of the two parameters $\alpha_{s\tau}$ and $\gamma_{s\tau}$. In particular, the valley-Zeeman term combines with the chemical potential to produce an effective spin-valley Fermi level. Instead, the Kane-Mele interaction combines with the onsite scalar potential to make a spin-valley-dependent gap, which lowers the supercurrent transport for small chemical potential values.

The effects of a Rashba spin-orbit coupling were studied numerically for experimentally relevant cases that include a high Rashba interaction with a smaller secondary one. Again, most of the results about the supercurrent phase relation stem from band structure modifications of the proximitized graphene; a small valley-Zeeman term opens a gap, while a small Kane-Mele term shifts the charge-neutrality point of graphene. Interestingly, we found that the Rashba interaction can sensibly boost the number of transparent modes through the junction, producing heavy swings in the skewness of the current-phase relation, which could have applications for devices needing tunable harmonic content.

Chapter 4

Finite-width effect in a graphene Josephson junction with spin-orbit coupling

In this Chapter, we extend the analysis of the previous Chapter by considering finite-width effects in a GJJ subjected to proximity-induced SOC. We still retain the short junction and Andreev approximation limits while still considering the zero temperature case. Given the complexity of the transport problem, which now includes the contribution from the edge states described in Sec. 1.5.3, we rely on numerical tight-binding simulations based on the KWANT Python package [314]. Due to its richer edge behavior, thanks to the presence of both pseudohelical and valley edge states, we are mainly going to address the gapped QVSHS phase. In particular, we focus mostly on the parameter values we have already explored in the previous section, namely, $\lambda_{\mathrm{R}} \approx 5\ \hbar v/L$ and $\lambda_{\mathrm{V}} \approx \hbar v/L$, which seem to be experimentally relevant [137,138,226]. At first, as done previously, we compute the transmission probabilities through a non-supeconducting junction and then use Eqs. (1.84,1.85) to calculate the supercurrent flow. Using this framework, we also investigate the robustness of the edge contribution to the supercurrent against scalar disorder in the form of edge imperfections. The results show a sizable supercurrent edge contribution which exhibits heavy Fabry-Perot resonances in the non-disordered case, especially for terminations with a high zigzag content, and which is fairly robust against small and high edge disorder. We then follow with an analysis of the magnetic interference pattern of the junction, for which we use the more general formulation of the scattering problem of Eqs. (1.80,1.81), since the system will no longer be time-reversal invariant. We find a high residual critical current at strong magnetic field values, which is consistent with the fact that most of the supercurrent is carried via the edges of the sample. We also find that the inversion-breaking SOC interactions, that generate the QVSHS phase, together with a perpendicular magnetic field, break the reciprocity of the supercurrent, producing a strong SDE in the junction.

This Chapter is organized as follows. In Sec. 4.1, we begin by introducing some numerical aspects of the simulations, such as the validity of the scaling procedure, together with the notation for the different edge terminations; we then proceed to show the results for the critical supercurrent against the chemical potential, for both the clean and disordered cases, where we investigate the relative contribution of the edge channels. In Sec. 4.2 we introduce a perpendicular magnetic field threading the junction and study the interference magnetic pattern of the critical current. We first analyze behavior of the critical current at high magnetic fluxes, which is an indicator of localized (edge) transport in the junction. Afterwards, we study the interference pattern at low magnetic field, and investigate the origin of the non-reciprocity of the supercurrent, producing, eventually, a simple analytical model to describe the resulting SDE.

4.1 Edge states contribution

In the scattering region of the junction we numerically implement the tight-binding Hamiltonian for graphene on a substrate that was introduced earlier in Eq. (1.55). For clarity purposes, we rewrite it here, already neglecting the U_z and λ_{PIA} terms

$$\begin{aligned}\mathcal{H} = -t \sum_{\langle i,j\rangle,s} c^{\dagger}_{is} c_{js} - \mu \sum_{i,s} c^{\dagger}_{is} c_{is} + \frac{2i\lambda_{\mathrm{R}}}{3} \sum_{\langle i,j\rangle,s,s'} \left[\left(\hat{\boldsymbol{s}} \times \boldsymbol{d}_{ij} \right)_z \right]_{ss'} c^{\dagger}_{is} c_{js'} \\ + \frac{i}{3\sqrt{3}} \sum_{\langle\langle i,j\rangle\rangle,s,s'} \lambda^{i}_{\mathrm{I}} \nu_{ij} \left[\hat{\boldsymbol{s}}_z \right]_{ss'} c^{\dagger}_{is} c_{js'},\end{aligned} \tag{4.1}$$

where t is the graphene hopping parameter, μ is he Fermi level, λ_{R} is the intensity of the R-SOC, and $\lambda_{\mathrm{I}}^{i} = \{\lambda_{\mathrm{I}}^{A}, \lambda_{\mathrm{I}}^{B}\}$ denote the intrinsic next nearest neighbor hoppings for the two sublattices, which combine to make the KM-SOC, $\lambda_{\mathrm{KM}} = (\lambda_{\mathrm{I}}^{A} + \lambda_{\mathrm{I}}^{B})/2$, and VZ-SOC, $\lambda_{\mathrm{VZ}} = (\lambda_{\mathrm{I}}^{A} - \lambda_{\mathrm{I}}^{B})/2$. We aim is to simulate a GJJ with a length of around $100 - 200$ nm. In recent transport measurements for graphene on transition metal dichalcogenides, in particular on WS_2, junctions of this length were found to still behave ballistically [140]. To reduce the computational resources needed, we use a scaling procedure that simulates the junction using a larger lattice constant as_{f}, where s_{f} is the scaling factor, with a renormalized hopping parameter t/s_{f} to make sure that the intrinsic graphene energy spectrum, given by $E_0 = (\sqrt{3}/2)at|\boldsymbol{k}|$, is unchanged [315]. The validity criterion for the scaling procedure is given by $s_{\mathrm{f}} \ll 3t\pi/|E_{\mathrm{max}}|$, where $|E_{\mathrm{max}}|$ is the maximum energy of interest that needs to be investigated [315]. So, taking a $\lambda_{\mathrm{R}} \approx 15$ meV, the validity criterion in our case becomes $s_{\mathrm{f}} \ll \frac{3t\pi}{\lambda_{\mathrm{R}}} = \frac{3 \cdot 2.8 \cdot \pi}{15 \cdot 10^{-3}} \approx 1760$. For our simulations, we take $s_{\mathrm{f}} \approx 13$. As in the previous Chapter, the leads are considered to be made of pristine graphene in the high doping limit. Numerically we set the Fermi level in both leads to $\mu_L = 0.2t$, in such a way as to be much higher than the energy scales used in the scattering region of the junction, but still in the linear regime of the graphene Dirac cones without trigonal warping effects [164]. In this section, we are also going to address different edge terminations which we label using two values (m, n) based on how many zigzag sections, m, and armchair sections, n, are present in the vector that defines the periodicity of the edge. More details on this are present in the Appendix B.

A plot of the band structure of a zigzag terminated graphene ribbon with $\lambda_{\mathrm{R}} = 5\,\hbar v/L$ and $\lambda_{\mathrm{VZ}} = \hbar v/L$ and a width of $W = 295a$ is shown in Fig.4.1a. As we have already discussed in Sec. 1.5.3 the system is in the QVSHS with a bulk gap of $2\min(\lambda_{\mathrm{R}}, \lambda_{\mathrm{VZ}}) = 2\lambda_{\mathrm{VZ}} = 2\hbar v/L$, highlighted from the grayed region in Fig. 4.1a. It hosts a pair of pseudohelical and valley edge modes. The pseudohelical ones cross $E = 0$ around $k = \pi$ and they are both spin and sublattice polarized, with spin up states moving in one direction (but on different edges) and spin down ones moving in the opposite. Instead, the valley edge states cross $E = 0$ close to the Dirac points and are neither spin nor sublattice polarized, since they originate

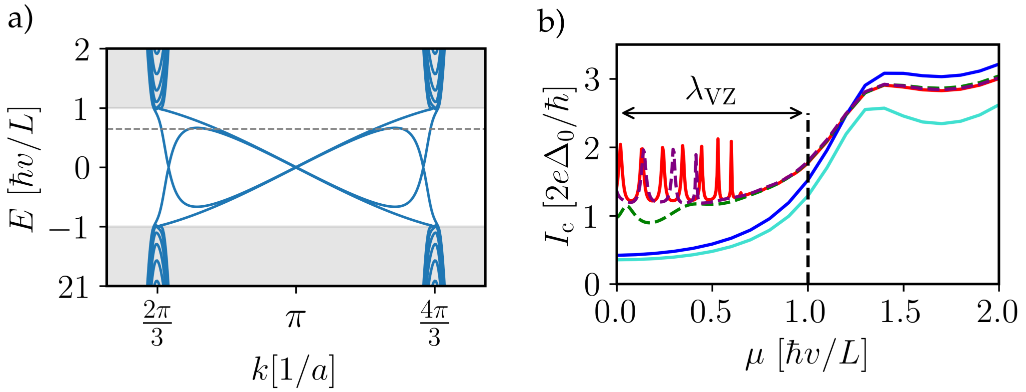

Figure 4.1: (a) band stucture of a zigzag terminated graphene ribbon with $\lambda_{\rm R} = 5\,\hbar v/L$ meV and $\lambda_{\rm VZ} = \hbar v/L$ and a width of around $295a$; the grayed out region defines the bulk band gap of $2\min(\lambda_{\rm R}, \lambda_{\rm VZ}) = 2\lambda_{\rm VZ} = 2\hbar v/L$. The ribbon hosts a pair of pseudohelical edge states that cross the gap at $k = \pi$ and a pair of valley edge modes that cross the gap around the Dirac points. The dashed horizontal line is the energy at which the Fabry-Perot resonance shown in (b) vanishes. (b) critical current of a GJJ for chemical potentials around the gapped region of the graphene layer; the parameters used are $\lambda_{\rm R} = 5\,\hbar v/L$, $\lambda_{\rm VZ} = \hbar v/L$ and a junction length and width of $L = 59a$, $W = 5L$. In red the results for a pure zigzag ribbon with $(m, n) = (1, 0)$, in purple (green) those for a $(m, n) = (2, 1)$ ($(m, n) = (1, 2)$) termination. In blue we show the results for a pure armchair ribbon, $(m, n) = (0, 1)$ and, as reference, in cyan we show the results computed in the previous section for a bulk system.

from the R-SOC interaction between states of opposite spin and sublattice.

In Fig. 4.1b we show the critical current for values of the chemical potential close to the gap: in red the results for a pure zigzag edge, in purple those for a mostly zigzag, $(m, n) = (2, 1)$, termination, in green those for a mostly armchair, $(m, n) = (1, 2)$, one; these results are compared to those of a pure armchair edge, in blue, that does not host edge modes, see Sec. 1.5.3, and to the previously computed bulk ones in cyan. We can make a few observations about the supercurrent in Fig. 4.1b. First, we see that, as we expected, the critical current for the proper armchair termination, in blue, closely follows the one we computed in the previous section, for a value of $W/L = 5$, originating only from bulk states, shown in cyan. The slight deviation over the gap is due to finite size effects that depend on the divisibility by 3 of the number or rows in the armchair tight-binding simulation [169], and it reduces with increasing chemical potential (not shown in the image). Second, we see that for non true armchair terminations, the contribution of the edge states is evident. Moreover, we can divide it into two parts. From Eq. (1.85) we know that every transmission channel with unit transmission probability, $\mathcal{T}_p \approx 1$, contributes to the supercurrent a factor of $\frac{2e\Delta_0}{2\hbar}$. The first part of the edge contribution comes from 2 channels with unit transmission probability: we attribute it to the pseudohelical edge modes, since it was already proven in previous works that they are insensitive to backscattering in time-reversal invariant systems [131]. The second part of the edge contribution comes, instead, from 2 other channels with non-unit transmission probabilities that undergo resonant tunneling with increasing chemical potential. We attribute it to the valley edge modes. This is corroborated by the fact that the Fabry-Perot resonances vanish before reaching the bulk gap, which is in line with the effective energy range of the valley edge modes, as highlighted by the dashed horizontal line in Fig. 4.1a. Moreover, we see that the resonant tunneling effect is more pronounced the more zigzag content there is in the edge termination: it barely shows for a mostly armchair edge with $(m, n) = (1, 2)$ (green), and it becomes extremely frequent for a pure zigzag one $(m, n) = (1, 0)$ (red). Notably, the pseudohelical contribution to the supercurrent seems, instead, to be insensitive to the edge termination, as long as there is a small zigzag content. This is in line with previous works on the general boundary conditions for honeycomb lattices [174].

We now analyze the robustness of the edge contribution against disorder in the form of edge roughness. We first consider the case of small disorder for the $(m, n) = \{(1, 0), (2, 1), (1, 2), (0, 1)\}$ terminations and of heavy disorder for the $(m, n) = \{(1, 0), (0, 1)\}$ ones. For the former, when building the graphene layer, we introduce a 0.2 probability that an edge atom, defined as having less than 3 nearest-neighbor atoms, gets removed; after this process the edge is cleaned of dangling atoms[1], also

---

[1] Atoms with less than two nearest-neighbor hopping atoms [314].

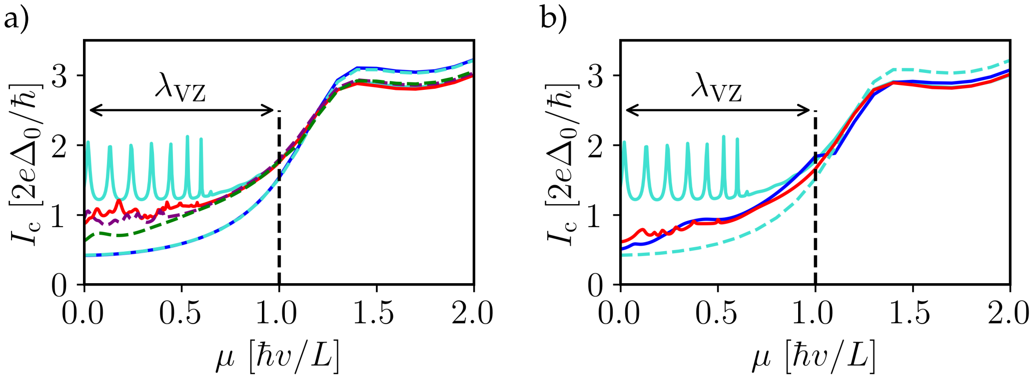

Figure 4.2: (a) critical current of a GJJ with small edge disorder (1 layer) for chemical potentials around the gapped region of the graphene layer; the parameters used are $\lambda_{\mathrm{R}} = 5\ \hbar v/L$, $\lambda_{\mathrm{VZ}} = \hbar v/L$ and a junction length and width of $L = 59a$, $W = 5L$. In red the results for a zigzag ribbon with $(m,n) = (1,0)$, in purple (green) those for a $(m,n) = (2,1)$ ($(m,n) = (1,2)$) termination. In blue we show the results for an armchair ribbon, $(m,n) = (0,1)$. (b) same as (a) but with heavy edge disorder (3 layers). In red the results for a zigzag ribbon with $(m,n) = (1,0)$ and in blue those for an armchair ribbon, $(m,n) = (0,1)$. In both images, as reference, in solid (dashed) cyan we show the results for a zigzag (armchair) non-disordered ribbon, showed in Fig. 4.1.

known as Klein defects [316]. For the latter, we repeat the previous process 6 times, which, on average, produces a maximum damage of depth 3-4 a on the edge, which is slightly more than 1% of the width of the junction. We then calculate the $I_{\mathrm{c}}(\mu)$ plots for 10 different realizations of disorder for every edge type considered and average the results. The computed averages are shown in Fig. 4.2a for the small disorder cases and in Fig. 4.2b for the high disorder ones. In both figures we show, as reference, the zigzag (armchair) clean edge case in solid (dashed) cyan. From Fig. 4.2a we see that the edge contribution is only slightly reduced for the edge types considered that have a zigzag content[2]. In contrast, the armchair termination seems to be completely insensitive to small dis-

---

[2] We also note that, independently, for each realization of disorder, the junction shows supercurrent peaks due to resonant tunneling, as we saw for the clean edge case. However, the intensities of these peaks are drastically reduced by the averaging procedure.

order. The situation changes when we consider heavy disorder. In this case, the edge contribution to the supercurrent for both disordered zigzag and armchair terminations tends to roughly the same value, as can be seen from Fig. 4.2b. For the armchair termination, this is an example of disorder-induced transport. Indeed, as we saw previously, a clean armchair sample does not host edge modes in the QVSHS phase of graphene. Therefore, introducing zigzag defects increases transport along the edges of the sample.

4.2 Magnetic interference pattern

We study the interference pattern of the supercurrent when the GJJ is threaded by a perpendicular magnetic field. As we said at the beginning of the previous section, we are modeling a GJJ with a total surface area of around $A_0 = 0.05 - 0.2\ \mu\text{m}^2$. The interference pattern arises with magnetic fields of the order of $B_{\Phi_0} = \Phi_0/A_0 \approx 10 - 40$ mT, and the Zeeman splitting energy for these magnetic fields is far below any other energy scale we have considered, $E_\text{Z} \approx 2\mu_\text{B} B_{\Phi_0} \approx 0.6 - 2.3\ \mu\text{eV}$. For this reason, we will include only the orbital effects of the magnetic field in the tight-binding simulations while neglecting the Zeeman coupling. In particular, the orbital effects are included in the tight-binding simulations via the Peierls substitution, which changes the hopping from site i to site j as

$$t_{ij} \longrightarrow t_{ij} \exp\left\{-i\frac{e}{\hbar}\int_i^j \boldsymbol{A}\cdot d\boldsymbol{l}\right\}. \tag{4.2}$$

In our simulations, the junction is oriented so that its width spans the x direction and its length the y one. We can thus use the Landau gauge

$$\boldsymbol{A} = (0, -B_z x, 0) \tag{4.3}$$

to describe a perpendicular magnetic field $\boldsymbol{B} = (0, 0, B_z)$, which substituted into Eq. (4.2) gives us

$$t_{ij} \longrightarrow t_{ij} \exp\left\{i\pi\frac{\Phi}{\Phi_0}\frac{x_j + x_i}{2}(y_j - y_i)\right\}, \tag{4.4}$$

where $\Phi_0 = h/2e$ is the superconducting magnetic flux quantum, $\Phi = B_z(LW) = B_z A_0$ is the magnetic flux threading the junction and x (y) is measured in units of W (L). Using the gauge of Eq. (4.3), we can consider a constant superconducting phase for each superconducting leads, allowing us to use the scattering matrix formalism introduced in Sec. 1.6.3 leading to Eq. (1.79) for the ABS energy. Moreover, according to Ref. [315], the scaling parameter now also has to satisfy $s_\mathrm{f} \ll l_B/a \approx 5700/\sqrt{B_z[\mathrm{mT}]}$, where $l_B = \sqrt{\hbar/eB_z}$ is the magnetic length. Even for high magnetic fluxes of $\Phi = 30\Phi_0$ we are a full order of magnitude within the validity of the scaling, $s_\mathrm{f} \approx 13 \ll 190$, which gets much better for smaller magnetic fluxes.

4.2.1 Supercurrent robustness at high magnetic fluxes

In this section, we analyze the robustness of the supercurrent in a proximitized GJJ against a magnetic flux threading the junction. From an analytical perspective, for the evaluation of the supercurrent one can implement the effects of a magnetic field by considering the gauge-invariant phase difference across the junction $\delta\phi = \delta\varphi - (2\pi/\Phi_0)\int \boldsymbol{A} \cdot d\boldsymbol{r}$, where $\delta\varphi = \varphi_2 - \phi_1$ is the superconducting phase difference between the superconductors [234]. Using the gauge of Eq. (4.3) we can then write the gauge-invariant phase picked by a Cooper pair moving along the vertical path $x \in [-W/2, W/2]$ across the junction as

$$\delta\phi(x) = \delta\varphi + \frac{2\pi\Phi}{\Phi_0}\frac{x}{W}. \tag{4.5}$$

Therefore, from a semiclassical point of view, we can imagine the vertical trajectories of the supercurrent effectively experiencing an evolving phase difference from one edge of the junction to the other, due to the presence of the magnetic field. In general, superconducting transport in a JJ can be composed of delocalized contributions, which are spread along the width of the junction, and more localized ones, which are instead highly spatially confined. In the former case, the supercurrent contribution is sensitive to the spatial variations of the gauge-invariant phase difference of Eq. (4.5), resulting in a contribution that averages out for high magnetic fluxes. An example of this is the typical Fraunhofer pattern in the critical

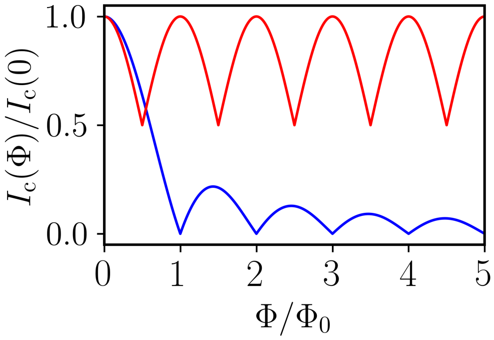

Figure 4.3: Critical current in function of the magnetic flux. In blue the Fraunhofer pattern, typical of tunnel junctions where most of the supercurrent is carried by low-transmission bulk channels. In red the periodic, non dampened behavior of two δ-localized edge modes of unit transmission.

current of tunnel junctions, $I_c(\Phi) = I_c(0)|\sin(\pi\Phi/\Phi_0)/(\pi\Phi/\Phi_0)|$, arising from low-transmission bulk contributions. An example of the latter is that of two δ-localized contributions of unit transmission at the edges of the junction; because of the extreme localization, these are insensitive to the gauge-invariant phase variation and produce a periodic critical current as

$$I_c(\Phi) = (I_c(0)/2)(1 + |\cos(\pi\Phi/\Phi_0)|), \tag{4.6}$$

which persists indefinitely in the magnetic field strength [317]. An example of both behaviors is shown in Fig. 4.3. Therefore, the persistence of the critical current at high magnetic fields is an indicator of the supercurrent degree of localization[3].

As already stated at the beginning of the Chapter, in the setup we

---

[3] In the simpler case of low-transparencies, one can apply the Dynes and Fulton description [318] to write the total supercurrent as

$$I(\Phi, \varphi) = \int_{-W/2}^{W/2} dx j(x) \sin\left(\varphi + \frac{2\pi\Phi}{\Phi_0}\frac{x}{W}\right), \tag{4.7}$$

from which it is possible to Fourier transform to directly obtain the supercurrent density profile of the JJ, $j(x)$. Unfortunately, it is not possible to apply this formalism when the junction has channels with high transmission probabilities.

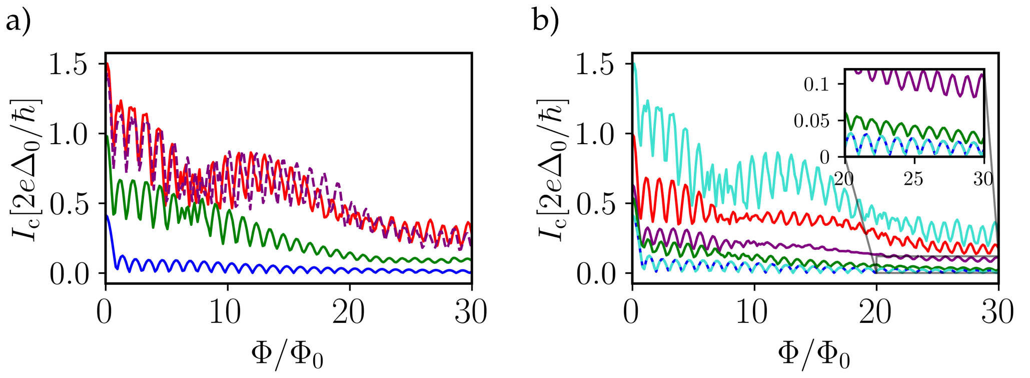

Figure 4.4: Critical supercurrent in function of the perpendicular magnetic field threading the junction. The parameters used are $\lambda_\mathrm{R} = 5\ \hbar v/L$, $\lambda_\mathrm{VZ} = \hbar v/L$ and a junction length and width of $L = 59a$, $W = 5L$. In (a) we show the clean edge case with different edge terminations; in red the results for a pure zigzag ribbon with $(m, n) = (1, 0)$, in purple (green) those for a $(m, n) = (2, 1)$ ($(m, n) = (1, 2)$) termination, and in blue the ones for a pure armchair ribbon, $(m, n) = (0, 1)$. In (b) we show the same plot as in (a) but for junction with disordered edges; in particular, in red (blue) we show the results for a zigzag (armchair) edge with small disorder, in purple (green) those for a zigzag (armchair) edge with heavy disorder, in solid (dashed) cyan we plot the clean zigzag (armchair) case for reference. The inset in (b) shows a zoom in the high field regions of the heavy disordered edges results.

are studying here, a proximitized GJJ in the QVSHS phase, the transport behavior is quite complex. In particular, when the Fermi level resides inside the gap, we have in general contributions from both evanescent bulk states with vanishing transparencies (similar to the tunnel junction case) and from edge states with different localizations and different transmission probabilities, as we have seen in Sec. 4.1. For this reason, we calculate the magnetic interference pattern numerically. Specifically, after defining a tight-binding system with scaled dimensions, as highlighted in Sec. 4.2, we use the KWANT Python package to compute the scattering matrix of a non-superconducting junction, from which, using the formalism leading to Eqs. (1.80,1.81), we eventually arrive at the CPR of the GJJ [266, 314]. The resulting interference pattern for the critical supercurrent, defined as $I_\mathrm{c} = \max_\varphi |I(\varphi)|$[4], computed at zero Fermi energy for various edge terminations is shown in Fig. 4.4a. The SOC parameters are the same as those used in Sec. 4.1, namely, $\lambda_\mathrm{R} = 5\,\hbar v/L$, $\lambda_\mathrm{VZ} = \hbar v/L$ and a junction length and width of $L = 59a$, $W = 5L$. In blue we plot the results for an armchair termination with $(m,n) = (0,1)$, in red those for a zigzag one, $(m,n) = (0,1)$, and in purple (green) those for a mostly zigzag (armchair) one with $(m,n) = (2,1)$ ($(m,n) = (1,2)$). From Fig. 4.4a we can make a few observations. First, we confirm that, due to the absence of edge states and thus localized currents, the residual critical current at high magnetic field is vanishing for an armchair termination, which is consistent with the QVSHS model introduced in Sec. 1.5.3 and with our previous findings of Sec. 4.1. All other terminations analyzed show, instead, a non-vanishing residual critical current, a sign of localized edge transport. Another feature we observe is that all non-armchair edge terminations show a beat around $\Phi/\Phi_0 \approx 7$. This is the result of two oscillating patterns of the kind we saw in Eq. (4.6) with slightly different frequencies. Our interpretation is that one frequency is due to the pseudohelical edge states that, being extremely localized at the edges of the sample width, experience the whole magnetic flux threading the junction, while the second frequency is due to the valley edge states that, being more delocalized [131], experience a lower effective flux compared to the total one. With increasing magnetic flux, the contribution to the total critical current of the valley edge states averages off, and for $\Phi/\Phi_0 \gtrsim 20$ most of the remaining critical current is due only to the pseudohelical edge states. Lastly, we observe that with increasing armchair content in the edge termination, the residual critical current diminishes, which is again consistent with the less localized nature of the edge states [174].

We also study the magnetic interference pattern for disordered edge terminations. We again distinguish small and heavy disorder, which are implemented in the same way as described in Sec. 4.1. The results are shown in Fig. 4.4b. In solid (dashed) cyan we plot the same results as in (a) for a clean zigzag (armchair) termination as reference. In red (blue)

---

[4] This is a slightly different definition from the one in Eq. (3.14) that we used in Chapter 3. The reason is that, as we will see in Sec. 4.2.2, with the introduction of a perpendicular magnetic field, the GJJ under study shows non-reciprocity of the supercurrent for which in general we can have $\max_\varphi |I(\varphi)| \neq \max_\varphi I(\varphi)$.

we show the results for small disorder in a zigzag (armchair) edge, and in purple (green) the same ones for heavy disorder. We find that for light disorder the interference pattern is quite robust for the zigzag case; indeed, it shows the same features we discussed about the clean case, with only a slight reduction in the residual critical current, which is due to an increase in the localization length of the edge states involved in the transport. For the armchair termination, small disorder has virtually no effect, in accordance with our previous results of Sec. 4.1. For heavy disorder we find that the zigzag termination follows the same trend: it exhibits the same features as before but with a further lowering of the residual critical current, again, we attribute this to an increased localization length of the edge states contributing to the transport. For the armchair termination, instead, the situation is the opposite. We find that heavy disorder actually increases both the supercurrent at low magnetic fluxes and the residual critical current at high magnetic fluxes, as can be seen by the inset of Fig. 4.4b. This means that, because of the edge disorder, more of the transport occurs in a localized fashion near the edges of the sample: this is an instance of disordered induced transport. The disorder along the armchair edge creates zigzag defects that, because the graphene layer is in the QVSHS phase, can locally host edge states. This is in line with previous results on bilayer graphene, where the authors find an asymptotic behavior of the Anderson localization length with increasing edge disorder, independently of the starting edge termination [319].

4.2.2 Superconducting Diode Effect

In the previous section, we have analyzed the behavior at high magnetic fluxes of the critical current of the junction, defined as $I_c = \max_\varphi |I(\varphi)|$. The reason for which we have defined I_c from the absolute value of $I(\varphi)$ is because our system shows a degree of non-reciprocity for transport in opposite directions. In particular, when we introduce a perpendicular magnetic field threading the junction, we obtain $\max_\varphi I(\varphi) \neq -\min_\varphi I(\varphi)$. In this section, we explore this feature of our setup in more detail.

The non-reciprocity of the supercurrent is known as Superconducting Diode Effect (SDE) [320], in analogy with the non-reciprocal transport, the diode effect, in a p-n semiconducting junction. The two main quantities that are used to characterize the SDE are the *non-reciprocal supercurrent*, ΔI_c, defined as the difference between the supercurrents flowing in the opposite directions, and the *diode efficiency*, η, which characterizes the relative asymmetry of the superconducting diode. In a JJ, they can be expressed in terms of the critical currents as [321–324]

$$\Delta I_\mathrm{c} = \max_{\varphi} I(\varphi) + \min_{\varphi} I(\varphi), \tag{4.8}$$

$$\eta = \frac{\Delta I_\mathrm{c}}{\max_{\varphi} I(\varphi) - \min_{\varphi} I(\varphi)}. \tag{4.9}$$

In Fig. 4.5 we show the results for the efficiency and the non-reciprocal supercurrent for a GJJ in the QVSHS phase with zigzag edge terminations. We find that the junction reaches a maximum efficiencies close to $\eta \approx 0.6$, while maintaining a non-reciprocal supercurrent comparable with the values of the critical current at zero magnetic fluxes, as can be seen by comparing with the right panel of Fig. 4.5. We also find that most of the SDE behavior occurs in a Fermi level region close to the gap, for $\mu \lesssim 1.25\ \hbar v/L$. Moreover, we obtain that there are certain Fermi level values for which the system does not exhibit any sizable non-reciprocal behavior (the white strips in the lower half of the plots); by comparing with the right panel, one can see that these values of the Fermi level correspond to those at which the Fabry-Perot resonances, due to the edge states and discussed in Sec. 4.1, occur. Given the aforementioned features, together with the fact that the same junction with armchair terminations does not show non-reciprocal behavior, we conclude that the observed SDE is a consequence of the edge transport in the junction. In particular, as we will see shortly, it is caused by an asymmetric transport between the two edges of the junction. This is in contrast to other SDEs observed in literature in planar JJ with R-SOC coupling [323–326]. In fact, in those systems, the SDE is observed when the system is coupled with a Zeeman splitting due to a magnetic field parallel to the junction. In our system, instead, this behavior originates purely from the orbital effect of the magnetic field, as we have neglected any Zeeman coupling in the junction, as explained at the beginning of Sec. 4.2.

We now further explore the edge transport asymmetry of our system. In order to do so, we analyze a simpler junction composed only of two

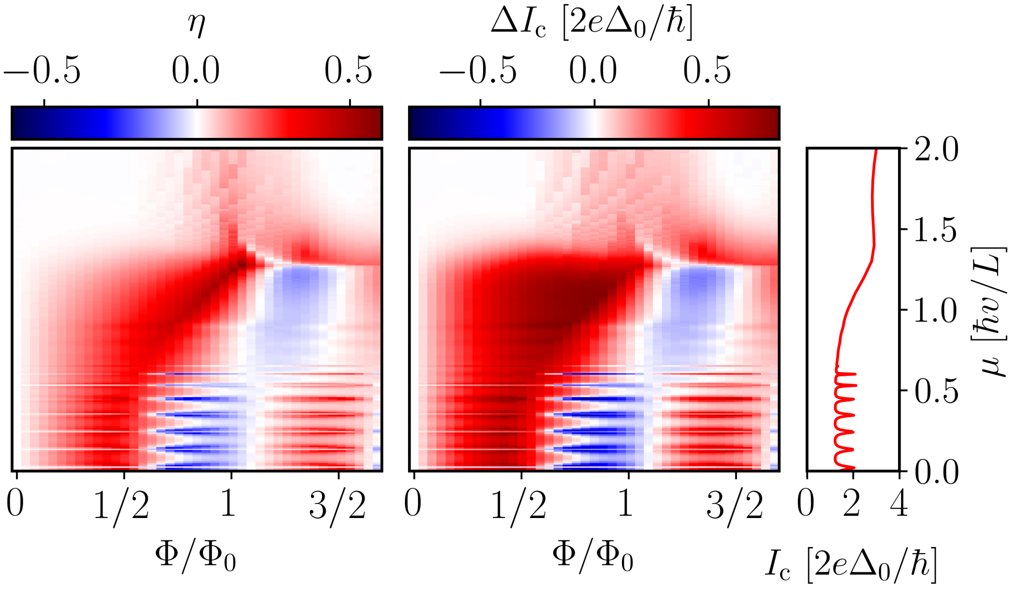

Figure 4.5: Efficiency, η, (left panel) and non-reciprocal supercurrent, ΔI_c, (middle panel) for a GJJ in the QVSHS phase with zigzag edge terminations, in function of the Fermi level of the graphene layer (vertical axis) and the magnetic flux threading the junction (horizontal axis). As reference, the right panel shows the critical current (horizontal axis) as a function of the Fermi level (vertical axis) for a junction with zigzag edges at zero magnetic flux, the same result shown in Fig. 4.1b. The SOC parameters used are the same as in the previous sections: $\lambda_{\mathrm{R}} = 5\ \hbar v/L$, $\lambda_{\mathrm{VZ}} = \hbar v/L$ with a junction length and width of $L = 59a$, $W = 5L$.

leads, the left one made of a zigzag graphene ribbon in the QVSHS phase and the right one made of pristine graphene with Fermi level $\mu_L = 0.2t$. A schematics of the junction is shown in Fig. 4.6. In the left panel of Fig. 4.7 we show the band structure of the left lead for Fermi values μ around the gap region. This is the same band structure we showed in Fig. 4.1a, but we have highlighted here the edge localization of the edge modes inside the gap: in blue (red) the states are localized on the bottom (top) edge of the ribbon. We note that because of the strong R-SOC interaction, this lead naturally shows a degree of asymmetry between the two edges. For example, we see that for any given value of Fermi level

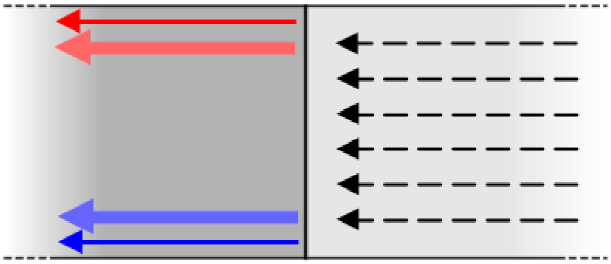

Figure 4.6: Schematics of the simpler two leads junction. The left lead is made of zigzag graphene in the QVSHS phase with SOC parameters $\lambda_{\mathrm{R}} = 5\,\hbar v/L$, $\lambda_{\mathrm{VZ}} = \hbar v/L$ with a ribbon width of $W = 295a$, while the right lead is made of pristine graphene with Fermi level $\mu_L = 0.2t$. The current is injected from the right lead and pictorially represented by black dashed arrows. For values of the Fermi level inside the energy gap, the left lead hosts four edge states, two on the top edge (in red) and two on the bottom one (in blue), compare to the band structure of Fig. 4.7.

different than $\mu = 0$ the velocities of the left moving states on the two edges are different. This asymmetry becomes extremely evident close to the bulk energy gap where all the edge modes are localized only on one edge of the ribbon, see the regions between the gray and black dashed horizontal lines in the left panel of Fig. 4.7. In the right panel of Fig. 4.7 we show the Landauer-Büttiker conductance obtained from injecting current from the right lead of the junction. The conductance is resolved into two contributions corresponding to outgoing current flowing on the opposite edges of the left lead, and they are color coded accordingly to the left panel. The edge resolved conductance is calculated in the following way. Solving the scattering problem returns us the transmission matrix $t_{\mathrm{LR}}(\mu)$ from the right to the left lead at a given Fermi level μ. From t_{LR} we can compute the transmission probabilities, τ, by solving the eigenvalue problem

$$t_{\mathrm{LR}} t_{\mathrm{LR}}^{\dagger} \begin{bmatrix} \psi^{\mathrm{T}} \\ \psi^{\mathrm{B}} \end{bmatrix}_{\tau} = \tau \begin{bmatrix} \psi^{\mathrm{T}} \\ \psi^{\mathrm{B}} \end{bmatrix}_{\tau} \tag{4.10}$$

where ψ^i is the component of the i-th left moving propagating state in the left lead, at energy μ, as explained in Sec. 1.6.3; T and B are collective

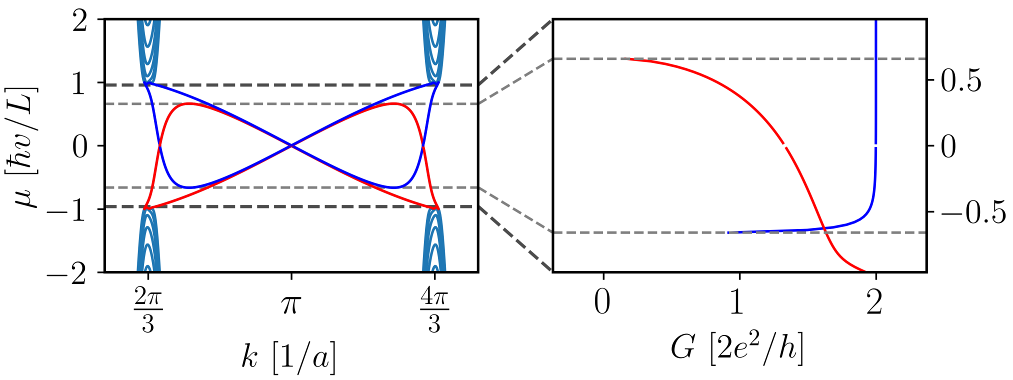

Figure 4.7: The left panel shows the band structure of a graphene zigzag ribbon in the QVSHS phase with SOC parameters $\lambda_{\mathrm{R}} = 5\ \hbar v/L$, $\lambda_{\mathrm{VZ}} = \hbar v/L$ with a ribbon width of $W = 295a$; the edge states inside the gap are highlighted in blue (red) if they are localized on the bottom (top) edge of the ribbon. The right panel shows the conductance computed for transport simulations where the current is injected from the right pristine lead of the junction with Fermi level $\mu_L = 0.2t$; the total conductance is split into two contributions, each referring to the conduction channels with corresponding colors in the left panel. In both panels the horizontal dashed black lines define the bulk energy gap and the area between black and gray horizontal lines represent the energy regions where the edge states are localized only on one edge of the ribbon.

indices for the top edge localized (in red) and bottom edge localized (in blue) propagating states in the band structure of Fig. 4.7. Having solved the eigenvalue problem of Eq. (4.10) we define the edge resolved conductance as

$$G = \begin{pmatrix} G^{\mathrm{T}} \\ G^{\mathrm{B}} \end{pmatrix} = \frac{2e^2}{h} \sum_{\tau} \tau \begin{pmatrix} |\psi_{\tau}^{\mathrm{T}}|^2 \\ |\psi_{\tau}^{\mathrm{B}}|^2 \end{pmatrix} . \tag{4.11}$$

G^{T} (G^{B}) corresponds to the red (blue) line in the right panel of Fig. 4.7, and the sum extends to all transmission eigenvalues. A strikingly odd feature of the computed conductance is that it does not respect the lead band structure symmetry between positive and negative values of Fermi level. In particular, we find that, for all the energy region between the dashed lines, the computed outgoing current in the left lead clearly prefers one edge of the ribbon to the other one.

To get a better understanding of the problem, we further simplify the setup and consider a left lead made of graphene in the QSHS phase with $\lambda_{\mathrm{KM}} = \hbar v/L$, while maintaining unchanged the right lead. As we described in Sec. 1.5.3, the edges in a QSHS graphene ribbon are symmetric, each hosting two helical edge states with opposite spins and moving in opposite directions. This is pictorially represented by the dashed red and blue edge states that cross the band gap in the band structure plot of Fig. 4.8a, where the color coding is the same as in Fig. 4.7. In this case, while the edge resolved conductance, as computed using Eq. (4.11), results in a symmetric split between the two edges, we find a clear asymmetry in the valley polarization of the incoming current. The incoming current polarization is computed in a similar way as the edge resolved conductance. In particular, we solve the transposed eigenvalue problem to Eq. (4.10)

$$t_{\mathrm{LR}}^{\dagger} t_{\mathrm{LR}} \begin{bmatrix} \psi^{\boldsymbol{K}} \\ \psi^{\boldsymbol{K}'} \end{bmatrix}_{\tau} = \tau \begin{bmatrix} \psi^{\boldsymbol{K}} \\ \psi^{\boldsymbol{K}'} \end{bmatrix}_{\tau}, \tag{4.12}$$

so that now ψ^i is the component of the i-th left moving propagating state in the *right* lead, at energy $\mu_L = 0.2t$, and the superscripts $\boldsymbol{K}$ ($\boldsymbol{K}'$) collectively indicates all the propagating modes of the $\boldsymbol{K} = 2\pi/3$ ($\boldsymbol{K}' = 4\pi/3$) valley. The $\boldsymbol{K}$ valley polarization of the incoming current, which is plotted in the right panels of Fig. 4.8, is then computed as $(\sum_\tau |\psi_\tau^{\boldsymbol{K}}|^2)/(\sum_\tau |\psi_\tau^{\boldsymbol{K}}|^2 + |\psi_\tau^{\boldsymbol{K}'}|^2)$ [5]. We see that, in the QSHS case, the incoming current is entirely polarized in the $\boldsymbol{K}$ valley for almost all Fermi level values inside the energy gap. Our explanation for this behavior is the following. Consider the left moving edge states in the QSHS band structure of Fig. 4.8a. We can see that, for different values of the Fermi level, μ, these edge states span the subspace of valence holes in the $\boldsymbol{K}'$ valley, close to the bottom of the energy gap, and of conduction electrons in the $\boldsymbol{K}$ valley, close to the top of the energy gap. While electron from the $\boldsymbol{K}'$ valley and holes from the $\boldsymbol{K}$ one are prerogative of the right moving edge states. For this reason, when injecting valley unpolarized current from the conduction band at $\mu_L = 0.2t$ from the right lead, the wavefunction matching condition at the

---

[5] Similarly, the $\boldsymbol{K}'$ valley polarization of the incoming current is going to be $1 - (\sum_\tau |\psi_\tau^{\boldsymbol{K}}|^2)/(\sum_\tau |\psi_\tau^{\boldsymbol{K}}|^2 + |\psi_\tau^{\boldsymbol{K}'}|^2)$.

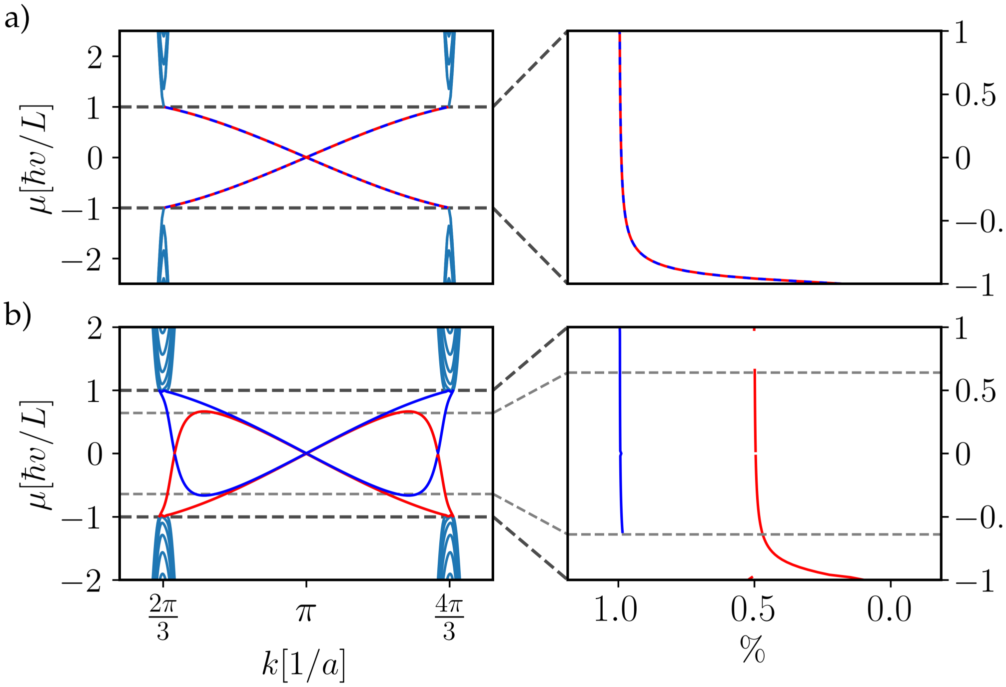

Figure 4.8: On the left the band structures of a zigzag graphene ribbon in the QSHS, with $\lambda_{\mathrm{KM}} = \hbar v/L$, in (a) and in the QVSHS, with $\lambda_{\mathrm{R}} = 5\ \hbar v/L$ and $\lambda_{\mathrm{VZ}} = \hbar v/L$, in (b). On the right the valley polarization of the incoming current, as defined in the main text, for Fermi level values inside the energy gap. The Fermi level of the pristine lead is $\mu_L = 0.2t$ and the color coding is the same as in Fig. 4.7.

interface heavy favors electrons from the $\boldsymbol{K}$ valley as opposed to electrons from the other valley. This holds true until, eventually, at the bottom of the energy gap, the valley degree of freedom takes dominance in the matching condition compared to the electron/hole one. We then extend this reasoning to the pseudohelical edge states of the QVSHS in Fig. 4.8b. Now, the induced $\boldsymbol{K}$ valley polarization of the incoming current, due to the pseudohelical edge states, lends itself to a better matching condition for the valley edge states of the $\boldsymbol{K}$ valley, which are localized on the bottom edge (blue color), more than for the ones of the $\boldsymbol{K}'$ valley, which are localized on the top edge (red color). A plot of the valley polarization of the incoming current for the QVSHS case is shown on the right panel of

Fig. 4.8b, which has to be compared with the edge resolved conductance previously shown in Fig. 4.7.

Finally, we return to the original junction composed of zigzag graphene in the QVSHS as scattering region and pristine graphene with $\mu_L = 0.2t$ in the leads. The picture we unveiled is that, overall, there are four edge channels contributing to the transport across the junction: two of these, a pseudohelical and a valley edge state, are localized on one edge of the junction and contribute to transport with a high transmission probability, for almost all values of the Fermi level; while the other two are localized on the opposite edge of the junction, they have a lower baseline transmission and undergo resonant tunneling with varying the Fermi level value, see, for example the right panel Fig. 4.5. At this point, we can introduce the magnetic field as outlined in Sec. 4.2.1 and build a minimal model as

$$I(\varphi, \Phi) = I_{\mathrm{B}} \frac{\sin(\pi\Phi/\Phi_0)}{\pi\Phi/\Phi_0} \sin(\varphi) + \frac{2e\Delta_0}{\hbar} \left[\frac{\tau_{\mathrm{T}} \sin(\varphi + \pi\Phi/\Phi_0)}{2\sqrt{1 - \tau_{\mathrm{T}} \sin^2((\varphi + \pi\Phi/\Phi_0)/2)}} \right. \\ \left. + \frac{\tau_{\mathrm{B}} \sin(\varphi - \pi\Phi/\Phi_0)}{2\sqrt{1 - \tau_{\mathrm{B}} \sin^2((\varphi - \pi\Phi/\Phi_0)/2)}} \right] \tag{4.13}$$

where the first term accounts for the delocalized bulk contribution [234, 327] and the other two for the localized ones from the top and bottom edges; the general formula for the supercurrent due to a single mode with transmission τ is the same as the one shown in Eq. (1.85). Clearly, Eq. (4.13) only holds for small magnetic fluxes for which the spatial extension of the edge states can be neglected. For what we said before, we have $\tau_{\mathrm{B}} \approx 1$, while τ_{T} ranges from as low as 0.25 to 1 depending on the resonance condition. When τ_{T} is in an off resonance condition, the edge contribution of Eq. (4.13) mixes two harmonics in the CPR of the junction as

$$\sim \frac{2e\Delta_0}{\hbar} \left[\frac{1}{2} \sin\left(\frac{\varphi - \pi\Phi/\Phi_0}{2} \right) + \frac{\tau_{\mathrm{T}}}{4} \sin(\varphi + \pi\Phi/\Phi_0) \right], \tag{4.14}$$

which was recently proposed in literature as a general way to generate non-reciprocal supercurrent in Josephson interferometers [113]. In our

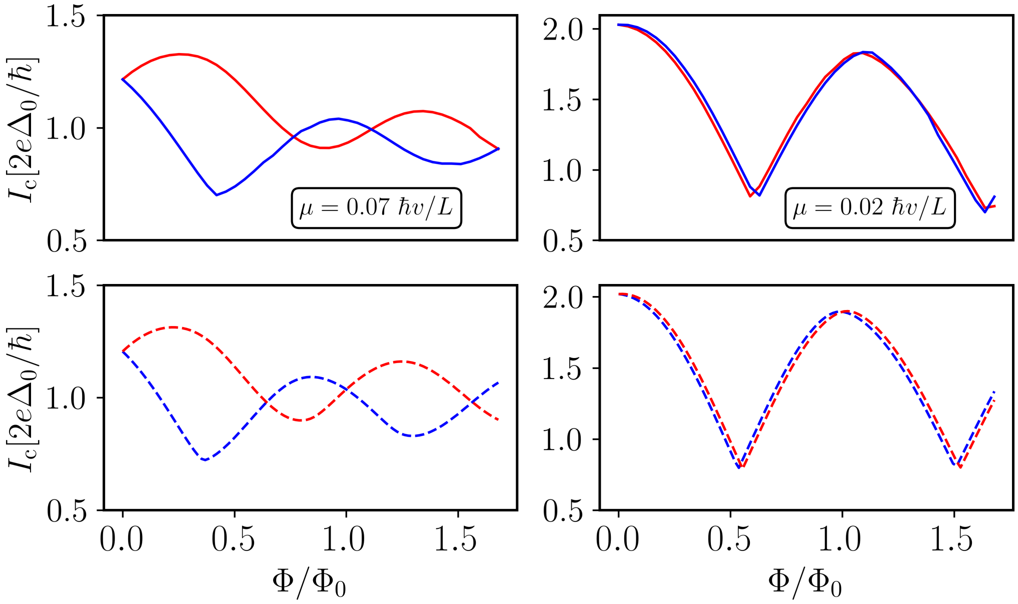

Figure 4.9: Solid (dashed) lines represent the results from the numerical simulation (minimal analytical model) and in red (blue) $\max_\varphi I(\varphi)$ ($\min_\varphi I(\varphi)$), on the left (right) the off (on) resonant case.

system this is realized in a single device. When τ_T is, instead, in an resonant condition the edge contribution reverts back to the periodical one of Eq. (4.6). In Fig. 4.9 we compare the minimal model of Eq. (4.13) with the numerical simulated results shown in Fig. 4.5 for the two just outlined cases. Specifically, we plot in solid (dashed) the results from the numerical simulation (minimal analytical model) and in red (blue) $\max_\varphi I(\varphi)$ ($\min_\varphi I(\varphi)$), on the left (right) the off (on) resonant case. The transmissions of the edges, $\tau_{T,B}$, and the value of I_B used in the minimal model are taken by solving the scattering problem for a non-superconducting junction at zero magnetic flux. We can see that the model reproduces quite well the simulated results, corroborating the result that the observed SDE originates from an asymmetry in the edge transport of the junction.

4.3 Conclusions

In this Chapter, we have studied the finite-width effects on the superconducting transport of a ballistic GJJ in which the inner graphene layer is in the QVSHS phase due to the interaction with a substrate. We still focused on the short junction limit at zero temperature. Using numerical tight-binding simulations, performed using the KWANT Python package, we were able to account for the edge contribution to the supercurrent and analyze it for different edge terminations and various implementations of disorder. We found that the edge contribution is composed of four channels, two with high transparency and two with low transparency; these last ones undergo resonant behavior when varying the Fermi level inside the energy gap, which produces heavy Fabry-Perot oscillations in the critical current of the junction. These features are highly evident for a pure zigzag termination and become less visible the more the armchair content of the edge. Eventually, as expected from the literature, a pure armchair termination has no contribution from the edge states. We also confirmed that the edge contribution is quite robust to scalar disorder in the form of edge roughness. Interestingly, disordering a pure armchair edge introduces zigzag defects which actually increase the edge transport in the junction, an example of disorder induced transport.

We then studied the magnetic interference pattern of the critical current in the junction. The persistence at high magnetic fields of the critical current is an indicator of localized transport, as the one occurring along the edges of the sample. We found that the interference pattern is characterized by beating due to the difference localization properties of the edge states present in the QVSHS graphene phase, and we found a residual critical current that is consistent with the results at zero magnetic field. Finally, we discovered that the system under study exhibits a strong nonreciprocity of the supercurrent, which leads to a SDE with a maximum efficiency close to 60%. The root cause of this behavior was established to lie in an asymmetric transport between the edges of the junction.

Conclusions

In this thesis, we have analyzed tunable properties of Dirac materials. In particular, in the first part of the thesis, we have studied Floquet-engineered interface states that emerge when two regions of a NLSM are irradiated with circularly polarized light of opposite polarization. Indeed, the light polarization mismatch generates interface states that display a rich structure due to the tunability provided by the external drive. We have focused on the band structure and pseudo-spin texture properties of the system. Our analysis revealed that the relative positioning of the WPs across the interface crucially determines the dispersion and topology of these boundary modes. We found that by varying the intensity of the incident light beams, it is possible to modify the Fermi line geometry and, in particular, to induce van Hove singularities in the interface density of states. The presence of such singularities near the Fermi level is of great significance, as it enhances correlation effects and can trigger electronic instabilities leading to exotic ordered phases, such as unconventional superconductivity or charge density waves. Moreover, we showed that additional control can be achieved by incorporating a magnetic barrier at the interface. Specifically, we have discovered that a topological non-trivial phase of the interface system itself can be determined and switched on/off by the external drive parameters. Taken together, these results provide promising platforms for optoelectronic applications and for the controlled realization of correlated quantum phases.

The second part of this thesis shifted the focus to superconducting transport in a GJJ, with particular attention to the modifications induced by substrate-engineered SOC. In this context, we studied how different types of SOC interactions influence the CPR of ballistic GJJ in the short and wide limits and at zero temperature. We developed a fully analytical treatment for the combined effects of onsite scalar potentials, KM-SOC, and VZ-SOC terms. We found that the transmission probabilities across the junction can be expressed in a compact form, identical in form to its pristine graphene counterpart, by introducing renormalized parameters that encapsulate the spin-valley-dependent modifications to the band structure. In particular, we found that the VZ-SOC term acts as a spin-valley-dependent chemical potential, effectively shifting the Fermi level, and enhancing, at low chemical potentials, both the critical current and the skewness of the junction CPR. Instead, the KM-SOC term combines with the scalar potential to open spin-valley-dependent gaps that suppress superconducting transport near the charge neutrality. We have also analyzed numerically the effects of a high R-SOC combined with a smaller secondary SOC interaction, a situation that seems experimentally relevant. Numerical analysis revealed that R-SOC coupling enhances the number of highly transmitting channels and induces pronounced oscillations in the skewness of the CPR, thus providing a knob for engineering junctions with tunable higher harmonics. Such control could be relevant for applications in multiterminal superconducting devices, superconducting diodes, and qubit implementations that rely on non-sinusoidal CPRs.

In the last part of the thesis, we extended the analysis of proximitized GJJ to include finite-width effects, focusing on the short junction limit at zero temperature. Using numerical tight-binding simulations with the KWANT Python package, we were able to resolve the edge contribution to the supercurrent for different edge terminations and disorder configurations. Our analysis revealed that the edge contribution consists of four channels: two with high transparency and two with low transparency. The low-transparency channels exhibit resonant behavior when tuning the Fermi level within the energy gap, producing pronounced Fabry–Perot oscillations in the critical current. These features are most prominent for pure zigzag edges and progressively diminish as the armchair content increases, vanishing entirely for pure armchair terminations. Interestingly, we observed that the introduction of edge disorder in armchair edges can create zigzag-like defects, enhancing edge transport, an example of disorder induced transport. We also investigated the magnetic interference pattern of the critical current. Its persistence at high magnetic fields confirms the localized nature of edge transport in

QVSHS graphene. The interference pattern exhibits a beating structure due to the differing localization properties of the edge channels, with a residual critical current consistent with the zero-field results. Finally, we uncovered a strong non-reciprocity in the supercurrent, giving rise to a SDE with an efficiency approaching 60%, which we traced to asymmetric transport between the two edges of the junction.

Appendices

Appendix A

Interface System between Floquet-Weyl semimetals

A.1 Numerical results

In this appendix, we present the numerical results for the energy dispersion and the pseudo-spin texture of the interface system obtained from a two bands continuous model of the NLSM by including the quadratic momentum contribution along all directions. We obtain qualitative agreement with the findings of the main text, where we found analytical results by instead neglecting the quadratic term in p_z. In particular, we show that the neglected term has no impact on the topological characterization of the interface system. We describe the electronic system with the following Hamiltonian

$$\mathcal{H}\left(\boldsymbol{p}\right)=\left[1-\left(p_x^2+p_y^2+p_z^2\right)\right]\sigma_x+up_z\sigma_z. \tag{A.1.1}$$

Similarly to Sec. 1.4.3 of the first chapter, we illuminate two regions of a NLSM with two beams of light, where each one is characterized by a vector potential of the form expressed in Eq. (2.1). Each side of the NLSM can be effectively described, in the high frequency regime, by the Floquet Hamiltonian [85]

$$\mathcal{H}_j(\boldsymbol{p})=\left[\bar{p}_j^2-\left(p_x^2+p_y^2+p_z^2\right)\right]\sigma_x+\lambda_j p_y\sigma_y+up_z\sigma_z, \tag{A.1.2}$$

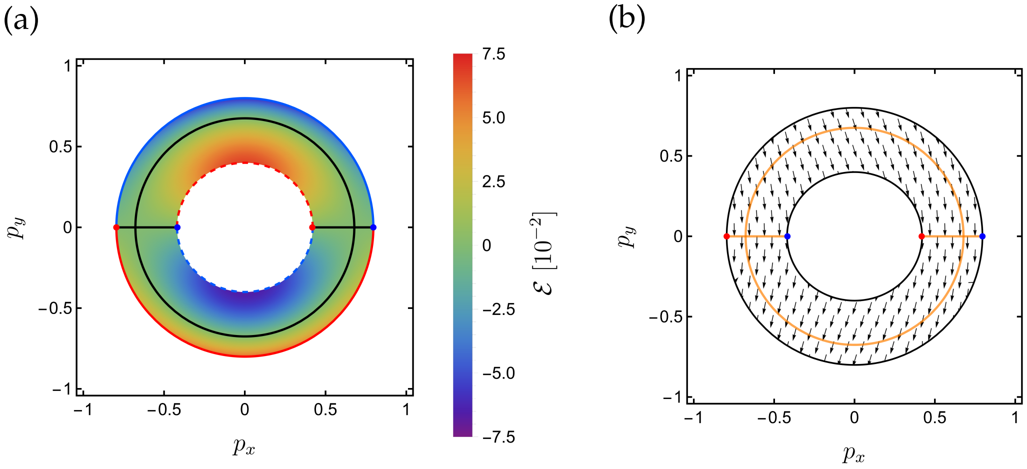

Figure A.1.1: (a) Density plot of the energy dispersion, and (b) pseudospin texture plot of the interface states as a function of the momentum components p_x and p_y in the asymmetric case ($\Lambda_{\mathrm{U}} < \Lambda_{\mathrm{L}}$), by holding the quadratic term in p_z in the Hamiltonian (A.1.1) which describes the NLSM. In panel (a) the boundary solid (dashed) lines represent the merging of the interface states' band with the upper (lower) FWSM bulk eigenbands. The red (blue) lines describe the merging into the conduction (valence) band, and red and blue dots represent WPPs of positive and negative chirality, respectively. The Fermi line $\mathcal{E} = 0$ is shown in black in panel (a) and in orange line in panel (b). The parameters used are: $u = 1, \Omega = 10$, $\Lambda_{\mathrm{U}} = 2$, $\Lambda_{\mathrm{L}} = 3$, $\phi_{\mathrm{U}} = \pi$, $\phi_{\mathrm{L}} = 0$.

where

$$\bar{p}_j = \sqrt{1 - e^2\Lambda_j^2}, \tag{A.1.3a}$$

$$\lambda_j = -2e^2\Lambda_j^2 u \cos\left(\phi_j\right)/\Omega, \tag{A.1.3b}$$

$$\Lambda_j = \frac{A_j}{b}, \tag{A.1.3c}$$

with $j \in \{\mathrm{L}, \mathrm{U}\}$ and $b = \sqrt{m/B}$. A quantitative difference with the model used in the main text is visible in the definition of the term $\bar{p}_j$, in fact in Eq. (2.13a) of the main text one has $\bar{p}_j = \sqrt{1 - e^2\Lambda_j^2/2}$. We follow the algebraic procedure used in Sec. 2.3. Firstly, we solve the eigenvalue problem for each half-space by using the ansatz shown in Eq. (2.15). Af-

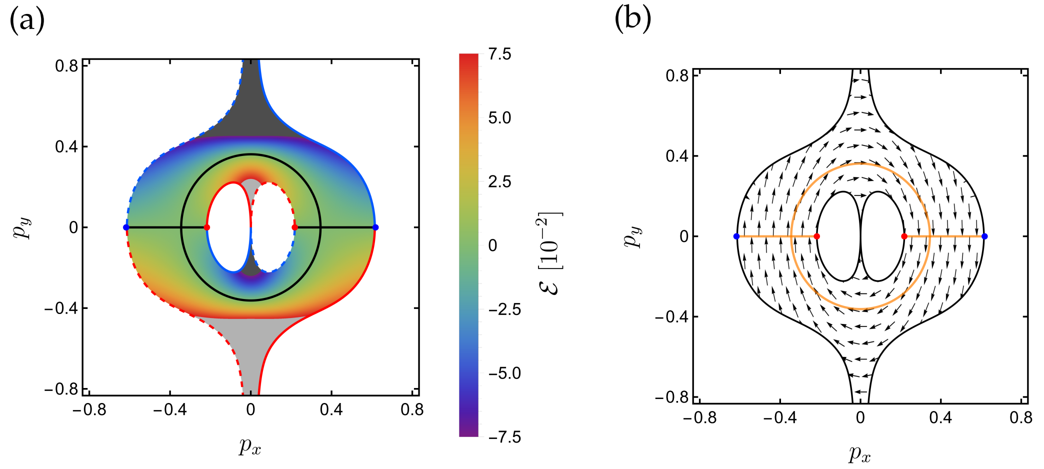

Figure A.1.2: (a) Density plot of the energy dispersion, and (b) pseudospin texture plot of the interface states as a function of the momentum components p_x and p_y, with $\Lambda_\mathrm{U} = \Lambda_\mathrm{L}$ and in the presence of a delta-like magnetic field along the interface $z = 0$, by holding the quadratic term in p_z in the Hamiltonian (A.1.1) which describes the NLSM. In panel (a) the boundary solid (dashed) lines represent the merging of the interface states' band with the lower (upper) FWSM bulk eigenbands. The red (blue) lines describe the merging into the conduction (valence) band, and red and blue dots represent WPPs of positive and negative chirality, respectively. Positive (negative) out of range values are depicted as light (dark) gray areas, and the Fermi line $\mathcal{E} = 0$ is shown in black in panel (a) and in orange line in panel (b). The parameters used are: $u = 1, \Omega = 10$, $\Lambda_\mathrm{U} = \Lambda_\mathrm{L} = 3$, $\phi_\mathrm{U} = \pi$, $\phi_\mathrm{L} = 0$, and the magnetic parameter is set at $p_0 = 1/5$.

terwards, we impose the continuity of the wavefunction and of its derivative at the interface $z = 0$. Finally, we force the normalizability of the wavefunction in the entire space. These conditions lead to a problem similar to that shown in Sec. 2.3, but here the matrix $\mathcal{M}$ becomes four-dimensional. The doubling of the dimension of the matrix $\mathcal{M}$ makes the problem hard for an analytical approach, then we face it with a numerical approach [310].

In the symmetric case ($\Lambda_\mathrm{U} = \Lambda_\mathrm{L}$), the energy dispersion of the interface electron system has the same features of the analytical expression shown in Fig. 2.2 (a). Here, the interface states are defined in the whole 2D momentum space with the exception of the $p_y = 0$ axis, where the interface band merges with the bulk bands, and the Fermi line at $\mathcal{E} = 0$ is composed by two semicircumferences that meet at the WPPs. Moreover, by using the definition of the pseudo-spin $\langle \sigma \rangle_{\boldsymbol{p}_\perp}$ in Eq. (2.28), one finds that the pseudo-spin has a trivial pattern, in particular, it is parallel (antiparallel) to the $\hat{x}$ axis for $p_y > 0$ ($p_y < 0$).

We now consider the interface system obtained in the asymmetric case, namely the intensities of the light beam are different ($\Lambda_{\mathrm{U}} < \Lambda_{\mathrm{L}}$). Figure A.1.1 shows the energy dispersion, panel (a), and the pseudo-spin texture, panel (b), of the interface states. We have chosen the same values of the parameters $u, \Omega, \Lambda_j, \phi_j$ used in Sec 2.3.1 of the main text. In Fig. A.1.1 (a) the interface states are defined in a region of the 2D momentum space delimited by the solid (dashed) lines which represent a merging of the interface band with the FWSM bulk bands delocalized along the upper region $z > 0$ (lower region $z < 0$). Moreover, red (blue) lines represent a merging of the interface band with a conduction (valence) band, while red (blue) dots are WPPs of positive (negative) chirality. The pseudo-spin texture of Fig. A.1.1 (b) shows a trivial pattern in terms of the winding number defined in Eq. (2.29). Apart from quantitative differences, mainly given by the modifications of the WPPs, both the energy dispersion and the pseudo-spin texture are qualitatively unaffected by the presence of the quadratic p_z term in the Hamiltonian (A.1.1).

To conclude, we introduce the delta-like magnetic barrier at the interface $z = 0$ described by Eq. (2.31). Figure A.1.2 (a) is the density plot of the energy dispersion of the interface states, while Fig. A.1.2 (b) represents the pseudo-spin texture, the parameters are set at the same values used in Sec 2.4. Here, we obtain that both the energy dispersion relation and the pseudo-spin texture are qualitatively in agreement with the analytical analysis of the main text. In particular, the non-vanishing winding number of the pseudo-spin texture defined in Eq. (2.29) occurs exactly like in the main text.

A.2 Solution of the continuity problem

We need to solve the following equation

$$\begin{aligned} \det\begin{pmatrix} \psi^{\mathrm{U}}_{1,-} & -\psi^{L}_{1,+} \\ \psi^{\mathrm{U}}_{2,-} & -\psi^{\mathrm{L}}_{2,+} \end{pmatrix} &= \left(-iu\bar{\mu}_{\mathrm{U}} + \mathcal{E}\right)\left(\alpha_{\mathrm{L}} - i\lambda_{\mathrm{L}} p_y\right) \\ &\quad - \left(iu\bar{\mu}_{\mathrm{L}} + \mathcal{E}\right)\left(\alpha_{\mathrm{U}} - i\lambda_{\mathrm{U}} p_y\right) = 0, \end{aligned} \tag{A.2.1}$$

where $\alpha_j = \bar{p}_j^2 - \left(p_x^2 + p_y^2\right)$. Moving the second term of Eq. (A.2.1) to the right hand side, dividing by $(iu\bar{\mu}_L + \mathcal{E})(\alpha_L + i\lambda_L p_y)$[1] and rationalizing, we obtain

$$\frac{(\mathcal{E} - iu\bar{\mu}_U)(\mathcal{E} - iu\bar{\mu}_L)}{\mathcal{E}^2 + (u\bar{\mu}_L)^2} = \frac{(\alpha_U - i\lambda_U p_y)(\alpha_L - i\lambda_L p_y)}{\alpha_L^2 + (\lambda_L p_y)^2}, \tag{A.2.2}$$

which can be simplified by noting that

$$\alpha_L^2 + (\lambda_L p_y)^2 = \mathcal{E}^2 + (v_L \bar{\mu}_L)^2. \tag{A.2.3}$$

Hence, equating the real and imaginary parts of Eq. (A.2.2) we are left with the following two equations

$$\mathcal{E}^2 - (u^2 \bar{\mu}_U \bar{\mu}_L) = \alpha_U \alpha_L - \lambda_U \lambda_L p_y^2, \tag{A.2.4a}$$

$$\mathcal{E} u(\bar{\mu}_U + \bar{\mu}_L) = p_y(\lambda_U \alpha_L + \lambda_L \alpha_U). \tag{A.2.4b}$$

Squaring the first hand side of the second of these equations and using both Eq. (A.2.3) and Eq. (A.2.4a) we obtain

$$\begin{aligned} &\mathcal{E}^2[(u\eta_U)^2 + (u\bar{\mu}_L)^2 + 2u^2\bar{\mu}_U\bar{\mu}_L] = \\ &= \mathcal{E}^2[\alpha_U^2 + \alpha_L^2 + (\lambda_U p_y^2) + (\lambda_L p_y^2) - 2(\mathcal{E}^2 - u^2\bar{\mu}_U\bar{\mu}_L)] = \\ &= \mathcal{E}^2[(\alpha_U - \alpha_L)^2 + (\lambda_U + \lambda_L)^2 p_y^2]. \end{aligned} \tag{A.2.5}$$

---

[1] Indeed, this quantity is always non vanishing: $\{\alpha_L, p_y\}$ can both be zero only at the WPs, but we are studying a region inside of them; and $\{\bar{\mu}_L, \mathcal{E}\}$ cannot simultaneously be zero because at Fermi energy the interface state cannot be fully delocalized inside of the semimetals, otherwise it would be a bulk state.

Therefore, using Eq. (A.2.4b) we get

$$\begin{aligned}\mathcal{E}^2 &= \frac{p_y^2(\lambda_U\alpha_L+\lambda_L\alpha_U)^2}{(\alpha_U-\alpha_L)^2+(\lambda_U+\lambda_L)^2p_y^2} \\ &= \frac{p_y^2\left\{\left[1-\left(p_x^2+p_y^2\right)\right]\left(\Lambda_{\mathrm{L}}^2\cos\phi_{\mathrm{L}}-\Lambda_{\mathrm{U}}^2\cos\phi_{\mathrm{U}}\right)-\frac{e^2}{2}\Lambda_{\mathrm{U}}^2\Lambda_{\mathrm{L}}^2\left(\cos\phi_{\mathrm{L}}-\cos\phi_{\mathrm{U}}\right)\right\}^2}{\left(\frac{\Omega}{4u}\right)^2\left(\Lambda_{\mathrm{U}}^2-\Lambda_{\mathrm{L}}^2\right)^2+\left(\Lambda_{\mathrm{U}}^2\cos\phi_{\mathrm{U}}-\Lambda_{\mathrm{L}}^2\cos\phi_{\mathrm{L}}\right)^2p_y^2}.\end{aligned} \tag{A.2.6}$$

where we have substituted Eqs. (2.13). Computing the square root of Eq. (A.2.6) gives us two solutions, which have to be combined in order to satisfy Eq. (A.2.4b). Doing so leads us to the final solution for the energy of the interface state, Eq. (2.24) of the main text.

A.3 Winding number and pseudo-spin texture

In the main text we characterize the topology of the interface system through the winding number of Eq. (2.29) as

$$\nu\left(\Gamma\right)=\frac{1}{2\pi}\int_0^1\left(\left\langle\sigma\right\rangle_{\boldsymbol{p}_\perp}\left(\tau\right)\times\frac{d}{d\tau}\left\langle\sigma\right\rangle_{\boldsymbol{p}_\perp}\left(\tau\right)\right)_z d\tau, \tag{A.3.1}$$

where $\tau\in\{0,1\}$ parametrizes a closed path Γ in momentum space that surrounds the origin of momenta. Equation (A.3.1) is intuitive in that it simply keeps track of whether the pseudo-spin is rotating clockwise or counterclockwise during its evolution in τ. Mathematically, since the pseudo-spin is a normalized quantity we can write it as $\left\langle\sigma\right\rangle_{\boldsymbol{p}_\perp}\left(\tau\right)=\left(\cos\theta\left(\tau\right),\sin\theta\left(\tau\right)\right)$ (neglecting the irrelevant z component), where $\theta\left(\tau\right)$ defines the direction of the pseudo-spin in the $x-y$ plane. Substituting this expression in Eq. (A.3.1) we obtain

$$\begin{aligned}\nu\left(\Gamma\right)=&\frac{1}{2\pi}\int_0^1\frac{d\theta}{d\tau}\left(\cos\theta\left(\tau\right),\sin\theta\left(\tau\right)\right)\times\\ &\times\left(-\sin\theta\left(\tau\right),\cos\theta\left(\tau\right)\right)d\tau\\ =&\frac{1}{2\pi}\left[\theta\left(1\right)-\theta\left(0\right)\right]=\nu,\end{aligned}$$

where in the last line we have used the fact that Γ is a closed curve and as such $\theta(1) - \theta(0) = 2\pi\nu$.

The pseudo-spin vector is defined through Eq. (2.28):

$$\begin{aligned}\langle \boldsymbol{\sigma} \rangle_{\boldsymbol{p}_\perp} &= \int d\boldsymbol{r} \Psi^\dagger_{\boldsymbol{p}_\perp}(\boldsymbol{r}) \boldsymbol{\sigma} \Psi_{\boldsymbol{p}_\perp}(\boldsymbol{r}) \\ &= \mathcal{N}_0 \begin{pmatrix} \psi^U_{1,-} & \psi^U_{2,-} \end{pmatrix}^* \boldsymbol{\sigma} \begin{pmatrix} \psi^U_{1,-} \\ \psi^U_{2,-} \end{pmatrix} \\ &= 2\mathcal{N}_0 \left(\mathrm{Re}\left(\psi^{U*}_{1,-} \psi^U_{2,-} \right), \mathrm{Im}\left(\psi^{U*}_{1,-} \psi^U_{2,-} \right) \right), \end{aligned} \tag{A.3.2}$$

where $\mathcal{N}_0 = \begin{pmatrix} \psi^U_{1,-} & \psi^U_{2,-} \end{pmatrix}^* \begin{pmatrix} \psi^U_{1,-} & \psi^U_{2,-} \end{pmatrix}^T$, $\boldsymbol{\sigma} = (\sigma_1, \sigma_2)$ (as said before, we neglect the z component), and where we could use only the upper space spinor because of the continuity condition at the interface. For the asymmetric case of Sec. 2.3.2, substituting Eq. (2.18) into Eq. (A.3.2) and calculating the result along the circumference at zero energy shown in Fig. 2.4 and parametrized by $(p_x, p_y) = R(\cos(\theta), \sin(\theta))$, where $R = \sqrt{\left(\lambda_U \bar{p}_L^2 - \lambda_L \bar{p}_U^2\right) / \left(\lambda_U - \lambda_L\right)}$, we get

$$\langle \sigma \rangle_{\boldsymbol{p}_\perp} = \frac{1}{\sqrt{\left(\lambda_U R \sin\theta\right)^2 + \left(R^2 - \bar{p}_U^2\right)^2}} \left(\lambda_U R \sin\theta, R^2 - \bar{p}_U^2 \right), \tag{A.3.3}$$

which is the normalized version of Eq. (2.30); λ_j and $\bar{p}_j$ are defined in Eqs. (2.13). Finally, inserting Eq. (A.3.3) into Eq. (A.3.1), the resulting winding number is vanishing

$$\nu = -\frac{R^2 - \bar{p}_U^2}{2\pi} \int_0^{2\pi} \frac{\lambda_U R \cos\theta}{\left(\lambda_U R \sin\theta\right)^2 + \left(R^2 - \bar{p}_U^2\right)^2} d\theta = 0. \tag{A.3.4}$$

On the contrary, performing the same calculations for the magnetic case of Sec. 2.4 along the circumference at zero energy shown in Fig 2.5 (b), which is parametrized by $(p_x, p_y) = \bar{R}(\cos(\theta), \sin(\theta))$, where $\bar{R} = \sqrt{\bar{p}^2 - p_0^2}$, we obtain

$$\langle \sigma \rangle_{\boldsymbol{p}_\perp} = \frac{1}{\left(\lambda_U \sin\theta\right)^2 + \left(2p_o \cos\theta\right)^2} \left(\lambda_U \sin\theta, -2p_0 \cos\theta \right) \tag{A.3.5}$$

for the pseudo-spin vector, and

$$\nu = \frac{\lambda_U p_0}{\pi} \int_0^{2\pi} \frac{1}{\left(\lambda_U \sin\theta\right)^2 + \left(2p_0 \cos\theta\right)^2} d\theta = +1 \tag{A.3.6}$$

for the winding number.

A.4 Non-triviality condition

In Sec. 2.4 of the main text, we mainly focused on the setup with a magnetic barrier between two FWSMs which are illuminated by light beams with opposite polarizations and same intensities. If we also allow for the intensities to be different on the two FWSMs then the energy dispersion of the interface system will be expressed as

$$\mathcal{E}\left(\boldsymbol{p}_\perp\right) = p_y \frac{\lambda_U \bar{p}_L^2 - \lambda_L \bar{p}_U^2 - \left[\left(p_x^2 + p_y^2 + p_0^2\right)\left(\lambda_U - \lambda_L\right) + 2p_0 p_x \left(\lambda_U + \lambda_L\right)\right]}{\sqrt{\left(\bar{p}_U^2 - \bar{p}_L^2 + 4p_0 p_x\right)^2 + \left[p_y\left(\lambda_U - \lambda_L\right)\right]^2}}, \tag{A.4.1}$$

which has to be compared with Eqs. (2.24) and (2.34). Similarly to the main text, see Fig. 2.5, the circumference at zero energy, $\mathcal{E}\left(\boldsymbol{p}_\perp\right) = 0$, is now given by:

$$\begin{aligned} p_x &= p_c + \tilde{R}\cos\theta, \\ p_y &= \tilde{R}\sin\theta, \end{aligned} \tag{A.4.2}$$

with

$$p_c = -p_0 \frac{\lambda_U + \lambda_L}{\lambda_U - \lambda_L}, \tag{A.4.3a}$$

$$\tilde{R}^2 = \frac{\lambda_U \bar{p}_L^2 - \lambda_L \bar{p}_U^2}{\lambda_U - \lambda_L} + \frac{4\lambda_U \lambda_L}{\left(\lambda_U - \lambda_L\right)^2} p_0^2. \tag{A.4.3b}$$

Performing the same calculations as in Appendix A.3, the pseudo-spin vector along this curcumference can be expressed as

$$\begin{aligned} \langle \boldsymbol{\sigma} \rangle_{\boldsymbol{p}_\perp} = &\frac{1}{\sqrt{\left(\lambda_U \tilde{R}\sin\theta\right)^2 + \left(\tilde{R}^2 + p_c^2 - \bar{p}_U^2 - 2Rp_c\cos\theta\right)^2}} \times \\ &\times \left(\lambda_U \tilde{R}\sin\theta, \tilde{R}^2 + p_c^2 - \bar{p}_U^2 - 2\tilde{R}p_c\cos\theta\right). \end{aligned} \tag{A.4.4}$$

Hence, the non-triviality condition of the pseudo-spin pattern is given by the "rotation" of the second component of the pseudo-spin vector in Eq. (A.4.4), namely:

$$\left|\tilde{R}^2 + p_c^2 - \bar{p}_U^2\right| < \left|2\tilde{R}p_c\right| . \tag{A.4.5}$$

It can then be numerically checked that Eq. (A.4.5) is satisfied when:

$$\left|\bar{p}_{\mathrm{U}} - \bar{p}_{\mathrm{L}}\right| < 2\left|p_0\right| < \bar{p}_{\mathrm{U}} + \bar{p}_{\mathrm{L}} , \tag{A.4.6}$$

which is Eq. (2.37).

Appendix B

Spin-Orbit Coupling effects in a Graphene Josephson Junction

B.1 Edge states localization with spin-orbit coupling

In Sec. 1.5.3 we have seen that the combination of R-SOC and VZ-SOC can create a topologically trivial graphene phase in combination with the existence of metallic time-reversal symmetry protected edge states, dubbed pseudohelical. In this section, we give a brief description of the localization properties of these pseudohelical edge states as a function of the strength of the underlying SOC interaction.

The degree of localization of edge states is characterized by the penetration depth, l_{p}, defined via the exponential decay of the electron density away from the edge $\rho(y) \propto e^{-y/l_{\mathrm{p}}}$. For graphene ribbons of a given width, W, the states at the opposite edges may overlap and hybridize to produce a finite splitting in the band structure which is related to the penetration depth as $\Delta_{\mathrm{W}} \propto e^{-W/l_{\mathrm{p}}}$ [328]. Except for a true zigzag termination, it was found that increasing the KM-SOC, λ_{KM}, enhances the localization of the helical edge modes by decreasing their penetration depth, l_{p} [151, 328]. Contrary to the KM-SOC case, and despite being necessary to have dispersive edge modes, we find that increasing λ_{VZ} actually increases the penetration depth of the edge modes and, as such, delocalizes them. A similar but greater effect occurs with increasing λ_{R}, which we expected since, eventually, a very strong λ_{R} opens a real gap in the edge states, which are no longer zero-energy modes, breaking both the QSHS and the QVSHS [131].

To this end, we consider a combination of SOCs with a given norm λ, $(\lambda_{\mathrm{VZ}}, \lambda_{\mathrm{R}}) = \lambda(\cos\theta, \sin\theta)$. In Fig.B.1.1b) we show the value of λ, as a function of the angle θ, at which the pseudohelical modes split over a given energy threshold. We plot the results for various edge terminations. Figure B.1.1a) shows the periodicity vectors that define the edge terminations we considered. Every edge termination is characterized by two numbers (m, n) where m (n) indicates the number of zigzag (armchair) sections in the periodicity vector. In Fig. B.1.1a), from blue to purple, the edge termination has increasing armchair content, in order: $(m, n) = (3, 1), (2, 1), (1, 1), (1, 2), (1, 3)$.

From Fig. B.1.1b) we can make a few observations. First, we see that the degree of armchair content in the edge termination has a drastic effect. In particular, at a given width W, the higher the armchair content, the less overall SOC, λ, is needed to produce a given energy splitting in the edge states. This is consistent with the fact that, eventually, a true armchair termination cannot host edge states with only the λ_{VZ} and λ_{R} SOC interactions [131], as we have already discussed more deeply in Sec. 1.5.3. Second, as anticipated above, the R-SOC, λ_{R}, has the greatest impact on the energy splitting of the edge states. Indeed, with increasing R-SOC content, for higher θ, the value of λ needed to produce the given threshold energy splitting is generally less. However, interestingly, this behavior is not monotonic. In particular, for zigzag-like terminations (see in Fig. B.1.1b) the blue and orange lines corresponding to the $(m, n) = (3, 1), (2, 1)$ terminations), there is a region in θ where increasing the proportion of λ_{R} actually reduces the finite width gap, Δ_{W}. This means that, in this parameter region, λ_{R} has a localizing effect on the edge states. To make this more clear we plot in Fig. B.1.1c) (in solid black) the splitting energy $\Delta_{\mathrm{S}}(\theta)$, between the pseudohelical edge states at zero energy for the $(m, n) = (3, 1)$ termination, along the blue dashed cut of Fig. B.1.1b). We observe that, when increasing the λ_{R} content around the $(0, \pi/8)$ region, the splitting $\Delta_{\mathrm{S}}(\theta)$ is reduced by several orders of magnitude to then increase suddenly after a critical value. This non monotonic behavior can be compared to that of a mostly armchair termination, $(m, n) = (1, 2)$, in Fig.B.1.1d), which follows the red dashed cut in Fig.B.1.1a). In this case, we do not observe the localizing effect of λ_R, but we also see a sudden increase of the splitting after a certain θ value. We associate the energy splitting Δ_S prior to these sudden jumps with finite-size effects, depending on the localization length of the edge states, hence $\Delta_S = \Delta_W$; while after these jumps the intensity of λ_R is already high enough to open a real gap between the edge modes, which no longer cross zero energy. To confirm this, in Fig. B.1.1c)-d) we plot, in blue, $\Delta_S(\theta)$ for a ribbon of smaller width $W' \approx 0.7W$, compared to the solid black case. Before the sudden jump, $\Delta_S(\theta)$ increases consistently with the reduction of width, while after the jump, $\Delta_S(\theta)$ is independent on the size and close, in order of magnitude, to the bulk gap $\Delta_B(\theta)$, shown in dashed black. This proves that, contrary to what one would expect, before breaking the QVSHS of graphene, λ_R has a strong localizing effect on the edge states of a ribbon with zigzag-like terminations.

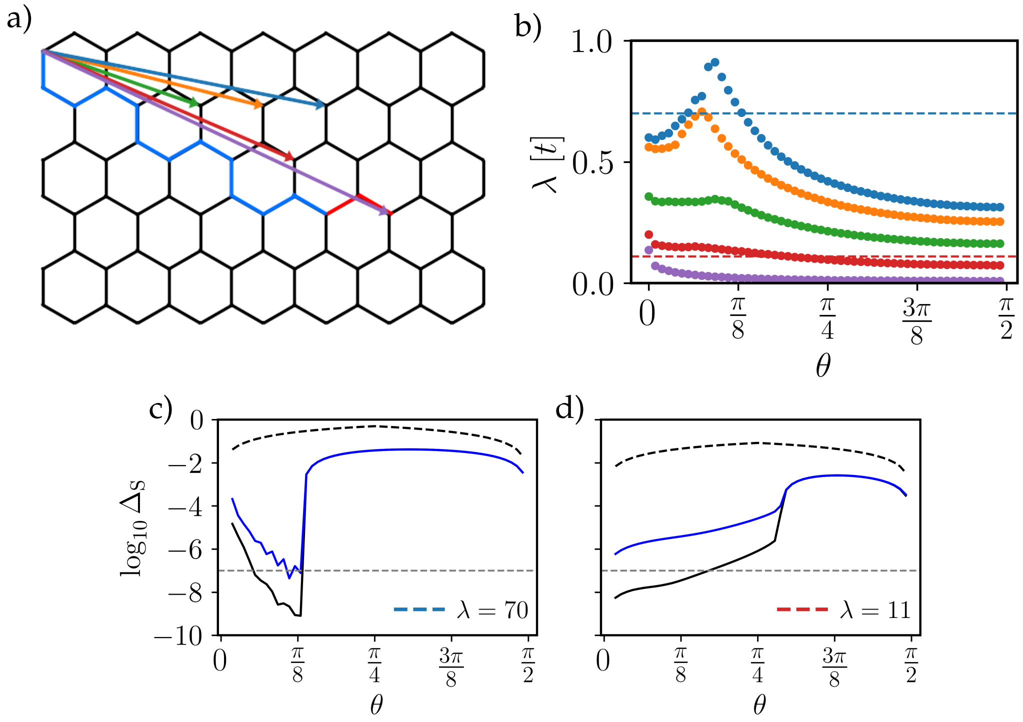

Figure B.1.1: a) graphene lattice on top of which we plot the vectors that define the periodicity of a given edge termination. From blue to purple the edge termination has increasing armchair content, in order: $(m, n) = (3, 1), (2, 1), (1, 1), (1, 2), (1, 3)$, where the first (second) value indicates the number of zigzag (armchair) sections in the periodicity vector. The colors are consistent with the other plots. A specific boundary cell is shown for the $(m, n) = (1, 3)$ edge, where in light blue (bright red) we plot the armchair (zigzag) sections. b) intensity λ of the combined SOC at which the pseudohelical edge states split over a given energy threshold. To compute it we performed tight-binding simulations using a ribbon of width $W = 85a$ and a threshold value of the energy of $10^{-7}\ [t]$. The different colors denote different edge termination with increasing armchair content from top (blue) to bottom (purple), as in a). c-d) in solid black we show the evolution energy splitting, Δ_S (in units of t), between the pseudohelical edge modes, along the cuts shown in b); the threshold energy value used in b) is shown in dashed gray. In particular, c) and d) refer to the $(m, n) = (3, 1)$ edge case and d) to the $(m, n) = (1, 2)$ one. In blue we plot the same metric but using a ribbon of width $W' = 0.7W$, in order to differentiate between the finite size effects and the R-SOC induced separation in the energy dispersion of the edge modes. In dashed black we plot the value of the bulk bandgap, $\Delta_B = 2\min(\lambda_R, \lambda_{VZ})$.

Acknowledgements

I would like to express my deepest gratitude to my supervisors, Prof. F.M.D. Pellegrino and Prof. E. Paladino, for their support, the fruitful discussions, and the guidance during my years as PhD student.

I am especially grateful to Prof. Pellegrino, who has been my mentor since my Master's thesis and is the main reason I decided to pursue a PhD in the first place. He has always treated me with respect and trust while teaching me what it means to be a researcher, from tackling physics problems to approaching life in academia. Beyond academia, he never hesitated to be a friend, and I am thankful for the conversations about life we shared, which have helped me grow not only as a scientist but also as a person.

I would also like to thank all my colleagues and friends from our research group for creating a stimulating and supportive environment, for the fruitful collaborations, and for the many moments of laughter and encouragement that made the challenging times easier to face. I am particularly grateful to the head of our group, Prof. G. A. Falci, for his wise guidance and leadership, which have fostered a spirit of collaboration and scientific curiosity that made working in the group both inspiring and rewarding.

A heartfelt thanks goes to my family for their unwavering love, patience, and belief in me throughout this long journey, their support has been the foundation on which I could always rely.

Finally, I owe my uttermost gratitude to my girlfriend, Francesca, my brother, Emanuele, and my truest friend, Enrico. Without them, I would not have been able to overcome the difficulties of this journey.

Bibliography

[1] K. v. Klitzing, G. Dorda, and M. Pepper, Phys. Rev. Lett. **45**, 494 (1980).

[2] R. B. Laughlin, Phys. Rev. B **23**, 5632 (1981).

[3] D. J. Thouless, M. Kohmoto, M. P. Nightingale, and M. den Nijs, Phys. Rev. Lett. **49**, 405 (1982).

[4] C. L. Kane and E. J. Mele, Phys. Rev. Lett. **95**, 146802 (2005).

[5] D. Thouless, Topological Quantum Numbers In Nonrelativistic Physics (World Scientific Publishing Company, Hackensack, NJ, 1998).

[6] M. Z. Hasan and C. L. Kane, Rev. Mod. Phys. **82**, 3045 (2010).

[7] Xiao-Liang Qi and Shou-Cheng Zhang, Rev. Mod. Phys. **83**, 1057 (2011).

[8] N. P. Armitage, E. J. Mele, and Ashvin Vishwanath, Rev. Mod. Phys. **90**, 015001 (2018).

[9] Chen Fang, Hongming Weng, Xi Dai, and Zhong Fang, Chinese Physics B **25**, 117106 (2016).

[10] Ching-Kai Chiu, Jeffrey C. Y. Teo, Andreas P. Schnyder, and Shinsei Ryu, Rev. Mod. Phys. **88**, 035005 (2016).

[11] Mahito Kohmoto, Annals of Physics **160**, 343 (1985).

[12] B. Andrei Bernevig, Taylor L. Hughes, and Shou-Cheng Zhang, Science **314**, 1757 (2006).

[13] Y. Tanaka, Zhi Ren, T. Sato, K. Nakayama, S. Souma, T. Takahashi, Kouji Segawa, and Yoichi Ando, Nature Physics **8**, 800 (2012).

[14] Masatoshi Sato and Yoichi Ando, Reports on Progress in Physics **80**, 076501 (2017).

[15] Manasi Mandal, Nathan C. Drucker, Phum Siriviboon, Thanh Nguyen, Artittaya Boonkird, Tej Nath Lamichhane, Ryotaro Okabe, Abhijatmedhi Chotrattanapituk, and Mingda Li, Chemistry of Materials **35**, 6184 (2023).

[16] Wei Chen and J. L. Lado, Physical Review Letters **122**, (2019).

[17] B. Q. Lv, T. Qian, and H. Ding, Rev. Mod. Phys. **93**, 025002 (2021).

[18] Yasuhiro Hatsugai, Phys. Rev. Lett. **71**, 3697 (1993).

[19] C. L. Kane and E. J. Mele, Phys. Rev. Lett. **95**, 226801 (2005).

[20] Markus König, Steffen Wiedmann, Christoph Brüne, Andreas Roth, Hartmut Buhmann, Laurens W. Molenkamp, Xiao-Liang Qi, and Shou-Cheng Zhang, Science **318**, 766 (2007).

[21] Andreas Roth, Christoph Brüne, Hartmut Buhmann, Laurens W. Molenkamp, Joseph Maciejko, Xiao-Liang Qi, and Shou-Cheng Zhang, Science **325**, 294 (2009).

[22] A. A. Burkov, M. D. Hook, and Leon Balents, Phys. Rev. B **84**, 235126 (2011).

[23] Lilia S. Xie, Leslie M. Schoop, Elizabeth M. Seibel, Quinn D. Gibson, Weiwei Xie, and Robert J. Cava, APL Materials **3**, 083602 (2015).

[24] Chen Fang, Yige Chen, Hae-Young Kee, and Liang Fu, Phys. Rev. B **92**, 081201 (2015).

[25] Youngkuk Kim, Benjamin J. Wieder, C. L. Kane, and Andrew M. Rappe, Phys. Rev. Lett. **115**, 036806 (2015).

[26] Guang Bian, Tay-Rong Chang, Raman Sankar, Su-Yang Xu, Hao Zheng, Titus Neupert, Ching-Kai Chiu, Shin-Ming Huang, Guoqing Chang, Ilya Belopolski, Daniel S. Sanchez, Madhab Neupane, Nasser Alidoust, Chang Liu, BaoKai Wang, Chi-Cheng Lee, Horng-Tay Jeng, Chenglong Zhang, Zhujun Yuan, Shuang Jia, Arun Bansil, Fangcheng Chou, Hsin Lin, and M. Zahid Hasan, Nature Communications **7**, 10556 (2016).

[27] Guang Bian, Tay-Rong Chang, Hao Zheng, Saavanth Velury, Su-Yang Xu, Titus Neupert, Ching-Kai Chiu, Shin-Ming Huang, Daniel S. Sanchez, Ilya Belopolski, Nasser Alidoust, Peng-Jen Chen, Guoqing Chang, Arun Bansil, Horng-Tay Jeng, Hsin Lin, and M. Zahid Hasan, Phys. Rev. B **93**, 121113 (2016).

[28] Y.-H. Chan, Ching-Kai Chiu, M. Y. Chou, and Andreas P. Schnyder, Phys. Rev. B **93**, 205132 (2016).

[29] Rui Yu, Hongming Weng, Zhong Fang, Xi Dai, and Xiao Hu, Phys. Rev. Lett. **115**, 036807 (2015).

[30] Rui Yu, Zhong Fang, Xi Dai, and Hongming Weng, Frontiers of Physics **12**, 127202 (2017).

[31] H.B. Nielsen and Masao Ninomiya, Physics Letters B **130**, 389 (1983).

[32] A. A. Burkov and Leon Balents, Phys. Rev. Lett. **107**, 127205 (2011).

[33] Xiangang Wan, Ari M. Turner, Ashvin Vishwanath, and Sergey Y. Savrasov, Phys. Rev. B **83**, 205101 (2011).

[34] B. Q. Lv, H. M. Weng, B. B. Fu, X. P. Wang, H. Miao, J. Ma, P. Richard, X. C. Huang, L. X. Zhao, G. F. Chen, Z. Fang, X. Dai, T. Qian, and H. Ding, Phys. Rev. X **5**, 031013 (2015).

[35] Shin-Ming Huang, Su-Yang Xu, Ilya Belopolski, Chi-Cheng Lee, Guoqing Chang, BaoKai Wang, Nasser Alidoust, Guang Bian, Madhab Neupane, Chenglong Zhang, Shuang Jia, Arun Bansil, Hsin Lin, and M. Zahid Hasan, Nature Communications **6**, 7373 (2015).

[36] Su-Yang Xu, Ilya Belopolski, Nasser Alidoust, Madhab Neupane, Guang Bian, Chenglong Zhang, Raman Sankar, Guoqing Chang, Zhujun Yuan, Chi-Cheng Lee, Shin-Ming Huang, Hao Zheng, Jie Ma, Daniel S. Sanchez, BaoKai Wang, Arun Bansil, Fangcheng Chou, Pavel P. Shibayev, Hsin Lin, Shuang Jia, and M. Zahid Hasan, Science **349**, 613 (2015).

[37] Sumathi Rao, (2016), arXiv:1603.02821.

[38] Binghai Yan and Claudia Felser, Annual Review of Condensed Matter Physics **8**, 337 (2017).

[39] Francesco M. D. Pellegrino, Mikhail I. Katsnelson, and Marco Polini, Phys. Rev. B **92**, 201407 (2015).

[40] Gian Marcello Andolina, Francesco M. D. Pellegrino, Frank H. L. Koppens, and Marco Polini, Phys. Rev. B **97**, 125431 (2018).

[41] Shuichi Murakami, New Journal of Physics **9**, 356 (2007).

[42] S. M. Young, S. Zaheer, J. C. Y. Teo, C. L. Kane, E. J. Mele, and A. M. Rappe, Phys. Rev. Lett. **108**, 140405 (2012).

[43] Z. K. Liu, B. Zhou, Y. Zhang, Z. J. Wang, H. M. Weng, D. Prabhakaran, S.-K. Mo, Z. X. Shen, Z. Fang, X. Dai, Z. Hussain, and Y. L. Chen, Science **343**, 864 (2014).

[44] Madhab Neupane, Su-Yang Xu, Raman Sankar, Nasser Alidoust, Guang Bian, Chang Liu, Ilya Belopolski, Tay-Rong Chang, Horng-Tay Jeng, Hsin Lin, Arun Bansil, Fangcheng Chou, and M. Zahid Hasan, Nature Communications **5**, 3786 (2014).

[45] Sergey Borisenko, Quinn Gibson, Danil Evtushinsky, Volodymyr Zabolotnyy, Bernd Büchner, and Robert J. Cava, Phys. Rev. Lett. **113**, 027603 (2014).

[46] A.Yu. Kitaev, Annals of Physics **303**, 2–30 (2003).

[47] A Yu Kitaev, Physics-Uspekhi **44**, 131 (2001).

[48] Chetan Nayak, Steven H. Simon, Ady Stern, Michael Freedman, and Sankar Das Sarma, Rev. Mod. Phys. **80**, 1083 (2008).

[49] Joel E. Moore, Nature **464**, 194 (2010).

[50] C.W.J. Beenakker, Annual Review of Condensed Matter Physics **4**, 113–136 (2013).

[51] Sankar Das Sarma, Michael Freedman, and Chetan Nayak, npj Quantum Information **1**, 15001 (2015).

[52] Biao Lian, Xiao-Qi Sun, Abolhassan Vaezi, Xiao-Liang Qi, and Shou-Cheng Zhang, Proceedings of the National Academy of Sciences **115**, 10938 (2018).

[53] Wenqin Chen, Jiachen Wang, Yijia Wu, Junjie Qi, Jie Liu, and X. C. Xie, Phys. Rev. B **105**, 054507 (2022).

[54] Morteza Aghaee, Alejandro Alcaraz Ramirez, Zulfi Alam, Rizwan Ali, Mariusz Andrzejczuk, Andrey Antipov, Mikhail Astafev, Amin Barzegar, Bela Bauer, Jonathan Becker, Umesh Kumar Bhaskar, Alex Bocharov, Srini Boddapati, David Bohn, Jouri Bommer, Leo Bourdet, Arnaud Bousquet, Samuel Boutin, Lucas Casparis, Benjamin J. Chapman, Sohail Chatoor, Anna Wulff Christensen, Cassandra Chua, Patrick Codd, William Cole, Paul Cooper, Fabiano Corsetti, Ajuan Cui, Paolo Dalpasso, Juan Pablo Dehollain, Gijs de Lange, Michiel de Moor, Andreas Ekefjärd, Tareq El Dandachi, Juan Carlos Estrada Saldaña, Saeed Fallahi, Luca Galletti, Geoff Gardner, Deshan Govender, Flavio Griggio, Ruben Grigoryan, Sebastian Grijalva, Sergei Gronin, Jan Gukelberger, Marzie Hamdast, Firas Hamze, Esben Bork Hansen, Sebastian Heedt, Zahra Heidarnia, Jesús Herranz Zamorano, Samantha Ho, Laurens Holgaard, John Hornibrook, Jinnapat Indrapiromkul, Henrik Ingerslev, Lovro Ivancevic, Thomas Jensen, Jaspreet Jhoja, Jeffrey Jones, Konstantin V. Kalashnikov, Ray Kallaher, Rachpon Kalra, Farhad Karimi, Torsten Karzig, Evelyn King, Maren Elisabeth Kloster, Christina Knapp, Dariusz Kocon, Jonne V. Koski,

Pasi Kostamo, Mahesh Kumar, Tom Laeven, Thorvald Larsen, Jason Lee, Kyunghoon Lee, Grant Leum, Kongyi Li, Tyler Lindemann, Matthew Looij, Julie Love, Marijn Lucas, Roman Lutchyn, Morten Hannibal Madsen, Nash Madulid, Albert Malmros, Michael Manfra, Devashish Mantri, Signe Brynold Markussen, Esteban Martinez, Marco Mattila, Robert McNeil, Antonio B. Mei, Ryan V. Mishmash, Gopakumar Mohandas, Christian Mollgaard, Trevor Morgan, George Moussa, Chetan Nayak, Jens Hedegaard Nielsen, Jens Munk Nielsen, William Hvidtfelt Padkar Nielsen, Bas Nijholt, Mike Nystrom, Eoin O'Farrell, Thomas Ohki, Keita Otani, Brian Paquelet Wütz, Sebastian Pauka, Karl Petersson, Luca Petit, Dima Pikulin, Guen Prawiroatmodjo, Frank Preiss, Eduardo Puchol Morejon, Mohana Rajpalke, Craig Ranta, Katrine Rasmussen, David Razmadze, Outi Reentila, David J. Reilly, Yuan Ren, Ken Reneris, Richard Rouse, Ivan Sadovskyy, Lauri Sainiemi, Irene Sanlorenzo, Emma Schmidgall, Cristina Sfiligoj, Mustafeez Bashir Shah, Kevin Simoes, Shilpi Singh, Sarat Sinha, Thomas Soerensen, Patrick Sohr, Tomas Stankevic, Lieuwe Stek, Eric Stuppard, Henri Suominen, Judith Suter, Sam Teicher, Nivetha Thiyagarajah, Raj Tholapi, Mason Thomas, Emily Toomey, Josh Tracy, Michelle Turley, Shivendra Upadhyay, Ivan Urban, Kevin Van Hoogdalem, David J. Van Woerkom, Dmitrii V. Viazmitinov, Dominik Vogel, John Watson, Alex Webster, Joseph Weston, Georg W. Winkler, Di Xu, Chung Kai Yang, Emrah Yucelen, Roland Zeisel, Guoji Zheng, Justin Zilke, and Microsoft Azure Quantum, Nature **638**, 651 (2025).

[55] Netanel H. Lindner, Gil Refael, and Victor Galitski, Nature Physics **7**, 490–495 (2011).

[56] Takuya Kitagawa, Erez Berg, Mark Rudner, and Eugene Demler, Phys. Rev. B **82**, 235114 (2010).

[57] Takashi Oka and Hideo Aoki, Phys. Rev. B **79**, 081406 (2009).

[58] Jun-ichi Inoue and Akihiro Tanaka, Phys. Rev. Lett. **105**, 017401 (2010).

[59] Zhenghao Gu, H. A. Fertig, Daniel P. Arovas, and Assa Auerbach, Phys. Rev. Lett. **107**, 216601 (2011).

[60] Takuya Kitagawa, Takashi Oka, Arne Brataas, Liang Fu, and Eugene Demler, Phys. Rev. B **84**, 235108 (2011).

[61] Mark S. Rudner, Netanel H. Lindner, Erez Berg, and Michael Levin, Phys. Rev. X **3**, 031005 (2013).

[62] Rui Wang, Baigeng Wang, Rui Shen, L. Sheng, and D. Y. Xing, EPL (Europhysics Letters) **105**, 17004 (2014).

[63] Hannes Hübener, Michael A. Sentef, Umberto De Giovannini, Alexander F. Kemper, and Angel Rubio, Nature Communications **8**, 13940 (2017).

[64] Ching-Kit Chan, Patrick A. Lee, Kenneth S. Burch, Jung Hoon Han, and Ying Ran, Phys. Rev. Lett. **116**, 026805 (2016).

[65] Liang Jiang, Takuya Kitagawa, Jason Alicea, A. R. Akhmerov, David Pekker, Gil Refael, J. Ignacio Cirac, Eugene Demler, Mikhail D. Lukin, and Peter Zoller, Phys. Rev. Lett. **106**, 220402 (2011).

[66] Fahad Mahmood, Ching-Kit Chan, Zhanybek Alpichshev, Dillon Gardner, Young Lee, Patrick A. Lee, and Nuh Gedik, Nature Physics **12**, 306–310 (2016).

[67] Netanel H. Lindner, Doron L. Bergman, Gil Refael, and Victor Galitski, Phys. Rev. B **87**, 235131 (2013).

[68] A. Gómez-León and G. Platero, Phys. Rev. Lett. **110**, 200403 (2013).

[69] Pierre Delplace, Álvaro Gómez-León, and Gloria Platero, Phys. Rev. B **88**, 245422 (2013).

[70] Takashi Oka and Sota Kitamura, Annual Review of Condensed Matter Physics **10**, 387–408 (2019).

[71] David Carpentier, Pierre Delplace, Michel Fruchart, and Krzysztof Gawędzki, Phys. Rev. Lett. **114**, 106806 (2015).

[72] Fenner Harper, Rahul Roy, Mark S. Rudner, and S.L. Sondhi, Annual Review of Condensed Matter Physics **11**, 345 (2020).

[73] Vedika Khemani, Achilleas Lazarides, Roderich Moessner, and S. L. Sondhi, Phys. Rev. Lett. **116**, 250401 (2016).

[74] Dominic V. Else, Bela Bauer, and Chetan Nayak, Phys. Rev. Lett. **117**, 090402 (2016).

[75] Rahul Roy and Fenner Harper, Phys. Rev. B **96**, 155118 (2017).

[76] Andrew C. Potter, Takahiro Morimoto, and Ashvin Vishwanath, Phys. Rev. X **6**, 041001 (2016).

[77] Dominic V. Else and Chetan Nayak, Phys. Rev. B **93**, 201103 (2016).

[78] C. W. von Keyserlingk, Vedika Khemani, and S. L. Sondhi, Phys. Rev. B **94**, 085112 (2016).

[79] Lukasz Fidkowski, Hoi Chun Po, Andrew C. Potter, and Ashvin Vishwanath, Phys. Rev. B **99**, 085115 (2019).

[80] Rahul Roy and Fenner Harper, Phys. Rev. B **95**, 195128 (2017).

[81] Xiao-Xiao Zhang, Tze Tzen Ong, and Naoto Nagaosa, Phys. Rev. B **94**, 235137 (2016).

[82] Rui Chen, Bin Zhou, and Dong-Hui Xu, Phys. Rev. B **97**, 155152 (2018).

[83] Zhongbo Yan and Zhong Wang, Phys. Rev. B **96**, 041206 (2017).

[84] Ching-Kit Chan, Yun-Tak Oh, Jung Hoon Han, and Patrick A. Lee, Phys. Rev. B **94**, 121106 (2016).

[85] Zhongbo Yan and Zhong Wang, Phys. Rev. Lett. **117**, 087402 (2016).

[86] Katsuhisa Taguchi, Dong-Hui Xu, Ai Yamakage, and K. T. Law, Phys. Rev. B **94**, 155206 (2016).

[87] Awadhesh Narayan, Phys. Rev. B **94**, 041409 (2016).

[88] Ryo Okugawa and Shuichi Murakami, Phys. Rev. B **96**, 115201 (2017).

[89] Y. H. Wang, H. Steinberg, P. Jarillo-Herrero, and N. Gedik, Science **342**, 453 (2013).

[90] Hongbin Zhang, Jiandong Yao, Jianmei Shao, Hai Li, Shuwei Li, Dinghua Bao, Chengxin Wang, and Guowei Yang, Scientific Reports **4**, 5876 (2014).

[91] Mark S. Rudner and Netanel H. Lindner, Nature Reviews Physics **2**, 229 (2020).

[92] André Eckardt, Rev. Mod. Phys. **89**, 011004 (2017).

[93] Karen Wintersperger, Christoph Braun, F. Nur Ünal, André Eckardt, Marco Di Liberto, Nathan Goldman, Immanuel Bloch, and Monika Aidelsburger, Nature Physics **16**, 1058 (2020).

[94] Alberto de la Torre, Dante M. Kennes, Martin Claassen, Simon Gerber, James W. McIver, and Michael A. Sentef, Rev. Mod. Phys. **93**, 041002 (2021).

[95] Ceren B. Dag and Aditi Mitra, Phys. Rev. B **105**, 245136 (2022).

[96] Jé rôme Cayssol, Balázs Dóra, Ferenc Simon, and Roderich Moessner, physica status solidi (RRL) - Rapid Research Letters **7**, 101 (2013).

[97] Arijit Kundu, H. A. Fertig, and Babak Seradjeh, Phys. Rev. Lett. **113**, 236803 (2014).

[98] A. S. Kazakov, A. V. Galeeva, A. I. Artamkin, A. V. Ikonnikov, L. I. Ryabova, S. A. Dvoretsky, N. N. Mikhailov, M. I. Bannikov, S. N. Danilov, and D. R. Khokhlov, Scientific Reports **11**, 11638 (2021).

[99] Wenliang Zhu, Yiyan Wang, Jing Li, Yifei Huang, Qingxin Dong, Xingyuan Hou, Lingxiao Zhao, Shuai Zhang, Huaixin Yang, Zhian Ren, Lei Shan, and Genfu Chen, Advanced Quantum Technologies **3**, 2000020 (2020).

[100] Haopeng Zhang, Xiaoming Zhang, Tingli He, Xuefang Dai, Ying Liu, Guodong Liu, Liying Wang, and Ying Zhang, Phys. Rev. B **102**, 155116 (2020).

[101] Nathalie P. de Leon, Kohei M. Itoh, Dohun Kim, Karan K. Mehta, Tracy E. Northup, Hanhee Paik, B. S. Palmer, N. Samarth, Sorawis Sangtawesin, and D. W. Steuerman, Science **372**, eabb2823 (2021).

[102] T. W. Larsen, K. D. Petersson, F. Kuemmeth, T. S. Jespersen, P. Krogstrup, J. Nygård, and C. M. Marcus, Phys. Rev. Lett. **115**, 127001 (2015).

[103] A. Kringhøj, L. Casparis, M. Hell, T. W. Larsen, F. Kuemmeth, M. Leijnse, K. Flensberg, P. Krogstrup, J. Nygård, K. D. Petersson, and C. M. Marcus, Phys. Rev. B **97**, 060508 (2018).

[104] Kan-Heng Lee, Srivatsan Chakram, Shi En Kim, Fauzia Mujid, Ariana Ray, Hui Gao, Chibeom Park, Yu Zhong, David A. Muller, David I. Schuster, and Jiwoong Park, Nano Letters **19**, 8287 (2019), pMID: 31661615.

[105] Abhinandan Antony, Martin V. Gustafsson, Guilhem J. Ribeill, Matthew Ware, Anjaly Rajendran, Luke C. G. Govia, Thomas A. Ohki, Takashi Taniguchi, Kenji Watanabe, James Hone, and Kin Chung Fong, Nano Letters **21**, 10122 (2021), pMID: 34792368.

[106] Oliver Sagi, Alessandro Crippa, Marco Valentini, Marian Janik, Levon Baghumyan, Giorgio Fabris, Lucky Kapoor, Farid Hassani, Johannes Fink, Stefano Calcaterra, Daniel Chrastina, Giovanni Isella, and Georgios Katsaros, Nature Communications **15**, 6400 (2024).

[107] J. G. Kroll, W. Uilhoorn, K. L. van der Enden, D. de Jong, K. Watanabe, T. Taniguchi, S. Goswami, M. C. Cassidy, and L. P. Kouwenhoven, Nature Communications **9**, 4615 (2018).

[108] C. W. J. Beenakker, Phys. Rev. Lett. **67**, 3836 (1991).

[109] Eric M. Spanton, Mingtang Deng, Saulius Vaitiekėnas, Peter Krogstrup, Jesper Nygård, Charles M. Marcus, and Kathryn A. Moler, Nature Physics **13**, 1177 (2017).

[110] B. van Heck, S. Mi, and A. R. Akhmerov, Phys. Rev. B **90**, 155450 (2014).

[111] Roman-Pascal Riwar, Manuel Houzet, Julia S. Meyer, and Yuli V. Nazarov, Nature Communications **7**, 11167 (2016).

[112] Falko Pientka, Anna Keselman, Erez Berg, Amir Yacoby, Ady Stern, and Bertrand I. Halperin, Phys. Rev. X **7**, 021032 (2017).

[113] Rubén Seoane Souto, Martin Leijnse, and Constantin Schrade, Phys. Rev. Lett. **129**, 267702 (2022).

[114] Marco Valentini, Oliver Sagi, Levon Baghumyan, Thijs de Gijsel, Jason Jung, Stefano Calcaterra, Andrea Ballabio, Juan Aguilera Servin, Kushagra Aggarwal, Marian Janik, Thomas Adletzberger, Rubén Seoane Souto, Martin Leijnse, Jeroen Danon, Constantin Schrade, Erik Bakkers, Daniel Chrastina, Giovanni Isella, and Georgios Katsaros, Nature Communications **15**, 169 (2024).

[115] T. W. Larsen, M. E. Gershenson, L. Casparis, A. Kringhøj, N. J. Pearson, R. P. G. McNeil, F. Kuemmeth, P. Krogstrup, K. D. Petersson, and C. M. Marcus, Phys. Rev. Lett. **125**, 056801 (2020).

[116] András Gyenis, Pranav S. Mundada, Agustin Di Paolo, Thomas M. Hazard, Xinyuan You, David I. Schuster, Jens Koch, Alexandre Blais, and Andrew A. Houck, PRX Quantum **2**, 010339 (2021).

[117] C. R. Dean, A. F. Young, I. Meric, C. Lee, L. Wang, S. Sorgenfrei, K. Watanabe, T. Taniguchi, P. Kim, K. L. Shepard, and J. Hone, Nature Nanotechnology **5**, 722 (2010).

[118] Alexander S. Mayorov, Roman V. Gorbachev, Sergey V. Morozov, Liam Britnell, Rashid Jalil, Leonid A. Ponomarenko, Peter Blake, Kostya S. Novoselov, Kenji Watanabe, Takashi Taniguchi, and A. K. Geim, Nano Letters **11**, 2396 (2011), pMID: 21574627.

[119] L. Wang, I. Meric, P. Y. Huang, Q. Gao, Y. Gao, H. Tran, T. Taniguchi, K. Watanabe, L. M. Campos, D. A. Muller, J. Guo, P. Kim, J. Hone, K. L. Shepard, and C. R. Dean, Science **342**, 614 (2013).

[120] V. E. Calado, S. Goswami, G. Nanda, M. Diez, A. R. Akhmerov, K. Watanabe, T. Taniguchi, T. M. Klapwijk, and L. M. K. Vandersypen, Nature Nanotechnology **10**, 761 (2015).

[121] M. Ben Shalom, M. J. Zhu, V. I. Fal'ko, A. Mishchenko, A. V. Kretinin, K. S. Novoselov, C. R. Woods, K. Watanabe, T. Taniguchi, A. K. Geim, and J. R. Prance, Nature Physics **12**, 318 (2016).

[122] I. V. Borzenets, F. Amet, C. T. Ke, A. W. Draelos, M. T. Wei, A. Seredinski, K. Watanabe, T. Taniguchi, Y. Bomze, M. Yamamoto, S. Tarucha, and G. Finkelstein, Phys. Rev. Lett. **117**, 237002 (2016).

[123] C. D. English, D. R. Hamilton, C. Chialvo, I. C. Moraru, N. Mason, and D. J. Van Harlingen, Phys. Rev. B **94**, 115435 (2016).

[124] G. Nanda, J. L. Aguilera-Servin, P. Rakyta, A. Kormányos, R. Kleiner, D. Koelle, K. Watanabe, T. Taniguchi, L. M. K. Vandersypen, and S. Goswami, Nano Letters **17**, 3396 (2017), pMID: 28474892.

[125] Monica T. Allen, Oles Shtanko, Ion C. Fulga, Joel I.-J. Wang, Daniyar Nurgaliev, Kenji Watanabe, Takashi Taniguchi, Anton R. Akhmerov, Pablo Jarillo-Herrero, Leonid S. Levitov, and Amir Yacoby, Nano Letters **17**, 7380 (2017), pMID: 29045153.

[126] Francesco M. D. Pellegrino, Giuseppe Falci, and Elisabetta Paladino, Communications Physics **3**, 6 (2020).

[127] Annica M. Black-Schaffer and Sebastian Doniach, Phys. Rev. B **78**, 024504 (2008).

[128] Annica M. Black-Schaffer and Jacob Linder, Phys. Rev. B **82**, 184522 (2010).

[129] Di Xiao, Wang Yao, and Qian Niu, Phys. Rev. Lett. **99**, 236809 (2007).

[130] G. W. Semenoff, V. Semenoff, and Fei Zhou, Phys. Rev. Lett. **101**, 087204 (2008).

[131] T. Frank, P. Högl, M. Gmitra, D. Kochan, and J. Fabian, Phys. Rev. Lett. **120**, 156402 (2018).

[132] J. Sichau, M. Prada, T. Anlauf, T. J. Lyon, B. Bosnjak, L. Tiemann, and R. H. Blick, Phys. Rev. Lett. **122**, 046403 (2019).

[133] A. Avsar, J. Y. Tan, T. Taychatanapat, J. Balakrishnan, G. K. W. Koon, Y. Yeo, J. Lahiri, A. Carvalho, A. S. Rodin, E. C. T. O'Farrell, G. Eda, A. H. Castro Neto, and B. Özyilmaz, Nature Communications **5**, 4875 (2014).

[134] J. B. S. Mendes, O. Alves Santos, L. M. Meireles, R. G. Lacerda, L. H. Vilela-Leão, F. L. A. Machado, R. L. Rodríguez-Suárez, A. Azevedo, and S. M. Rezende, Phys. Rev. Lett. **115**, 226601 (2015).

[135] Martin Gmitra and Jaroslav Fabian, Phys. Rev. B **92**, 155403 (2015).

[136] Zhe Wang, Dong-Keun Ki, Hua Chen, Helmuth Berger, Allan H. MacDonald, and Alberto F. Morpurgo, Nature Communications **6**, 8339 (2015).

[137] T. Wakamura, F. Reale, P. Palczynski, S. Guéron, C. Mattevi, and H. Bouchiat, Phys. Rev. Lett. **120**, 106802 (2018).

[138] L. Sun, L. Rademaker, D. Mauro, A. Scarfato, Á. Pásztor, I. Gutiérrez-Lezama, Z. Wang, J. Martinez-Castro, A. F. Morpurgo, and C. Renner, Nature Communications **14**, 3771 (2023).

[139] Klaus Zollner and Jaroslav Fabian, 2D Materials **12**, 013004 (2024).

[140] T. Wakamura, N. J. Wu, A. D. Chepelianskii, S. Guéron, M. Och, M. Ferrier, T. Taniguchi, K. Watanabe, C. Mattevi, and H. Bouchiat, Phys. Rev. Lett. **125**, 266801 (2020).

[141] Shun-Qing Shen, Wen-Yu Shan, and Hai-Zhou Lu, SPIN **01**, 33–44 (2011).

[142] Di Xiao, Ming-Che Chang, and Qian Niu, Rev. Mod. Phys. **82**, 1959 (2010).

[143] David Vanderbilt, Berry Phases in Electronic Structure Theory: Electric Polarization, Orbital Magnetization and Topological Insulators (Cambridge University Press, Cambridge, 2018).

[144] H.B. Nielsen and M. Ninomiya, Physics Letters B **105**, 219 (1981).

[145] Ching-Kai Chiu and Andreas P. Schnyder, Phys. Rev. B **90**, 205136 (2014).

[146] Su-Yang Xu, Nasser Alidoust, Ilya Belopolski, Zhujun Yuan, Guang Bian, Tay-Rong Chang, Hao Zheng, Vladimir N. Strocov, Daniel S. Sanchez, Guoqing Chang, Chenglong Zhang, Daixiang Mou, Yun Wu, Lunan Huang, Chi-Cheng Lee, Shin-Ming Huang, BaoKai Wang, Arun Bansil, Horng-Tay Jeng, Titus Neupert, Adam Kaminski, Hsin Lin, Shuang Jia, and M. Zahid Hasan, Nature Physics **11**, 748 (2015).

[147] N. Xu, H. M. Weng, B. Q. Lv, C. E. Matt, J. Park, F. Bisti, V. N. Strocov, D. Gawryluk, E. Pomjakushina, K. Conder, N. C. Plumb, M. Radovic, G. Autès, O. V. Yazyev, Z. Fang, X. Dai, T. Qian, J. Mesot, H. Ding, and M. Shi, Nature Communications **7**, 11006 (2016).

[148] Su-Yang Xu, Ilya Belopolski, Daniel S. Sanchez, Chenglong Zhang, Guoqing Chang, Cheng Guo, Guang Bian, Zhujun Yuan, Hong Lu, Tay-Rong Chang, Pavel P. Shibayev, Mykhailo L. Prokopovych, Nasser Alidoust, Hao Zheng, Chi-Cheng Lee, Shin-Ming Huang, Raman Sankar, Fangcheng Chou, Chuang-Han Hsu, Horng-Tay Jeng, Arun Bansil, Titus Neupert, Vladimir N. Strocov, Hsin Lin, Shuang Jia, and M. Zahid Hasan, Science Advances **1**, e1501092 (2015).

[149] Shuang Jia, Su-Yang Xu, and M. Zahid Hasan, Nature Materials **15**, 1140–1144 (2016).

[150] Z. K. Liu, L. X. Yang, Y. Sun, T. Zhang, H. Peng, H. F. Yang, C. Chen, Y. Zhang, Y. F. Guo, D. Prabhakaran, M. Schmidt, Z. Hussain, S.-K. Mo, C. Felser, B. Yan, and Y. L. Chen, Nature Materials **15**, 27 (2016).

[151] N. Xu, G. Autès, C. E. Matt, B. Q. Lv, M. Y. Yao, F. Bisti, V. N. Strocov, D. Gawryluk, E. Pomjakushina, K. Conder, N. C. Plumb, M. Radovic, T. Qian, O. V. Yazyev, J. Mesot, H. Ding, and M. Shi, Phys. Rev. Lett. **118**, 106406 (2017).

[152] Evan O'Leary, Zhuoqi Li, Lin-Lin Wang, Benjamin Schrunk, Andrew Eaton, Paul C. Canfield, and Adam Kaminski, Phys. Rev. B (2025).

[153] Kai-Yu Yang, Yuan-Ming Lu, and Ying Ran, Phys. Rev. B **84**, 075129 (2011).

[154] A A Burkov, Journal of Physics: Condensed Matter **27**, 113201 (2015).

[155] Qiunan Xu, Rui Yu, Zhong Fang, Xi Dai, and Hongming Weng, Physical Review B **95**, (2017).

[156] Lukas Muechler, Andreas Topp, Raquel Queiroz, Maxim Krivenkov, Andrei Varykhalov, Jennifer Cano, Christian R. Ast, and Leslie M. Schoop, Phys. Rev. X **10**, 011026 (2020).

[157] Tomáš Bzdušek, QuanSheng Wu, Andreas Rüegg, Manfred Sigrist, and Alexey A. Soluyanov, Nature **538**, 75 (2016).

[158] Jinling Lian, Lixian Yu, Qi-Feng Liang, Jian Zhou, Rui Yu, and Hongming Weng, npj Computational Materials **5**, 10 (2019).

[159] Ilya Belopolski, Guoqing Chang, Tyler A. Cochran, Zi-Jia Cheng, Xian P. Yang, Cole Hugelmeyer, Kaustuv Manna, Jia-Xin Yin, Guangming Cheng, Daniel Multer, Maksim Litskevich, Nana Shumiya, Songtian S. Zhang, Chandra Shekhar, Niels B. M. Schröter, Alla Chikina, Craig Polley, Balasubramanian Thiagarajan, Mats Leandersson, Johan Adell, Shin-Ming Huang, Nan Yao, Vladimir N. Strocov, Claudia Felser, and M. Zahid Hasan, Nature **604**, 647 (2022).

[160] Junyan Liu, Yibo Wang, Xuebin Dong, Jinying Yang, Shen Zhang, Meng Lyu, Binbin Wang, Hongxiang Wei, Shouguo Wang, Enke Liu, and Baogen Shen, Phys. Rev. B **109**, 235144 (2024).

[161] Po-Yao Chang, Nodal-line semimetals and their variance, 2025, arXiv:2507.02329.

[162] André Eckardt and Egidijus Anisimovas, New Journal of Physics **17**, 093039 (2015).

[163] K. S. Novoselov, A. K. Geim, S. V. Morozov, D. Jiang, M. I. Katsnelson, I. V. Grigorieva, S. V. Dubonos, and A. A. Firsov, Nature **438**, 197 (2005).

[164] A. H. Castro Neto, F. Guinea, N. M. R. Peres, K. S. Novoselov, and A. K. Geim, Rev. Mod. Phys. **81**, 109 (2009).

[165] Congcong Le, Zhesen Yang, Fan Cui, A. P. Schnyder, and Ching-Kai Chiu, Phys. Rev. B **106**, 045126 (2022).

[166] M. I. Katsnelson, K. S. Novoselov, and A. K. Geim, Nature Physics **2**, 620 (2006).

[167] János K. Asbóth, László Oroszlány, and András Pályi, A Short Course on Topological Insulators (Springer International Publishing, Cham, 2016).

[168] Junyeong Ahn, Sungjoon Park, and Bohm-Jung Yang, Phys. Rev. X **9**, 021013 (2019).

[169] L. Brey and H. A. Fertig, Phys. Rev. B **73**, 235411 (2006).

[170] Wang Yao, Shengyuan A. Yang, and Qian Niu, Phys. Rev. Lett. **102**, 096801 (2009).

[171] P. Delplace, D. Ullmo, and G. Montambaux, Phys. Rev. B **84**, 195452 (2011).

[172] Roger S. K. Mong and Vasudha Shivamoggi, Phys. Rev. B **83**, 125109 (2011).

[173] C. W. J. Beenakker, Rev. Mod. Phys. **80**, 1337 (2008).

[174] A. R. Akhmerov and C. W. J. Beenakker, Phys. Rev. B **77**, 085423 (2008).

[175] Yousuke Kobayashi, Ken-ichi Fukui, Toshiaki Enoki, Koichi Kusakabe, and Yutaka Kaburagi, Phys. Rev. B **71**, 193406 (2005).

[176] W. Jaskólski, A. Ayuela, M. Pelc, H. Santos, and L. Chico, Phys. Rev. B **83**, 235424 (2011).

[177] W. L. McMillan, Phys. Rev. **175**, 537 (1968).

[178] J. J. Hauser, Phys. Rev. **187**, 580 (1969).

[179] A. I. Buzdin, Rev. Mod. Phys. **77**, 935 (2005).

[180] P.K. Manna and S.M. Yusuf, Physics Reports **535**, 61 (2014), two interface effects: Exchange bias and magnetic proximity.

[181] Igor Žutić, Alex Matos-Abiague, Benedikt Scharf, Hanan Dery, and Kirill Belashchenko, Materials Today **22**, 85 (2019).

[182] Juan F. Sierra, Jaroslav Fabian, Roland K. Kawakami, Stephan Roche, and Sergio O. Valenzuela, Nature Nanotechnology **16**, 856 (2021).

[183] T. Wakamura, F. Reale, P. Palczynski, M. Q. Zhao, A. T. C. Johnson, S. Guéron, C. Mattevi, A. Ouerghi, and H. Bouchiat, Phys. Rev. B **99**, 245402 (2019).

[184] Dongying Wang, Mohammed Karaki, Nicholas Mazzucca, Haidong Tian, Guixin Cao, ChunNing Lau, Yuan-Ming Lu, Marc Bockrath, Kenji Watanabe, and Takashi Taniguchi, Phys. Rev. B **104**, L201301 (2021).

[185] Priya Tiwari, Mohit Kumar Jat, Adithi Udupa, Deepa S. Narang, Kenji Watanabe, Takashi Taniguchi, Diptiman Sen, and Aveek Bid, npj 2D Materials and Applications **6**, 68 (2022).

[186] Qing Rao, Wun-Hao Kang, Hongxia Xue, Ziqing Ye, Xuemeng Feng, Kenji Watanabe, Takashi Taniguchi, Ning Wang, Ming-Hao Liu, and Dong-Keun Ki, Nature Communications **14**, 6124 (2023).

[187] Manuel Offidani, Mirco Milletarì, Roberto Raimondi, and Aires Ferreira, Phys. Rev. Lett. **119**, 196801 (2017).

[188] Jose H. Garcia, Marc Vila, Aron W. Cummings, and Stephan Roche, Chem. Soc. Rev. **47**, 3359 (2018).

[189] S. Omar and B. J. van Wees, Phys. Rev. B **97**, 045414 (2018).

[190] Adel Belayadi and Panagiotis Vasilopoulos, Nanotechnology **34**, 085704 (2022).

[191] D. Kochan, S. Irmer, and J. Fabian, Phys. Rev. B **95**, 165415 (2017).

[192] Martin Gmitra, Denis Kochan, Petra Högl, and Jaroslav Fabian, Phys. Rev. B **93**, 155104 (2016).

[193] Hongki Min, J. E. Hill, N. A. Sinitsyn, B. R. Sahu, Leonard Kleinman, and A. H. MacDonald, Phys. Rev. B **74**, 165310 (2006).

[194] M. Gmitra, S. Konschuh, C. Ertler, C. Ambrosch-Draxl, and J. Fabian, Phys. Rev. B **80**, 235431 (2009).

[195] Gianluca Giovannetti, Petr A. Khomyakov, Geert Brocks, Paul J. Kelly, and Jeroen van den Brink, Phys. Rev. B **76**, 073103 (2007).

[196] Jeil Jung, Ashley M. DaSilva, Allan H. MacDonald, and Shaffique Adam, Nature Communications **6**, 6308 (2015).

[197] Wang Yao, Di Xiao, and Qian Niu, Phys. Rev. B **77**, 235406 (2008).

[198] Motohiko Ezawa, Phys. Rev. B **83**, 100408 (2011).

[199] A. J. Niemi and G. W. Semenoff, Phys. Rev. Lett. **51**, 2077 (1983).

[200] Yuanbo Zhang, Yan-Wen Tan, Horst L. Stormer, and Philip Kim, Nature **438**, 201 (2005).

[201] A. K. Geim and K. S. Novoselov, Nature Materials **6**, 183 (2007).

[202] Haruki Watanabe, Yasuhiro Hatsugai, and Hideo Aoki, Phys. Rev. B **82**, 241403 (2010).

[203] R. V. Gorbachev, J. C. W. Song, G. L. Yu, A. V. Kretinin, F. Withers, Y. Cao, A. Mishchenko, I. V. Grigorieva, K. S. Novoselov, L. S. Levitov, and A. K. Geim, Science **346**, 448 (2014).

[204] Yuri D. Lensky, Justin C. W. Song, Polnop Samutpraphoot, and Leonid S. Levitov, Phys. Rev. Lett. **114**, 256601 (2015).

[205] A. F. Morpurgo and F. Guinea, Phys. Rev. Lett. **97**, 196804 (2006).

[206] A. Rycerz, J. Tworzydło, and C. W. J. Beenakker, Nature Physics **3**, 172 (2007).

[207] J. L. Garcia-Pomar, A. Cortijo, and M. Nieto-Vesperinas, Phys. Rev. Lett. **100**, 236801 (2008).

[208] Mikkel Settnes, Stephen R. Power, Mads Brandbyge, and Antti-Pekka Jauho, Phys. Rev. Lett. **117**, 276801 (2016).

[209] Steven A. Vitale, Daniel Nezich, Joseph O. Varghese, Philip Kim, Nuh Gedik, Pablo Jarillo-Herrero, Di Xiao, and Mordechai Rothschild, Small **14**, 1801483 (2018).

[210] Zhenhua Qiao, Shengyuan A. Yang, Bin Wang, Yugui Yao, and Qian Niu, Phys. Rev. B **84**, 035431 (2011).

[211] M. Zarenia, O. Leenaerts, B. Partoens, and F. M. Peeters, Phys. Rev. B **86**, 085451 (2012).

[212] Yafei Ren, Zhenhua Qiao, and Qian Niu, Reports on Progress in Physics **79**, 066501 (2016).

[213] J. R. Anglin and A. Schulz, Phys. Rev. B **95**, 045430 (2017).

[214] Zibo Wang, Shuguang Cheng, Xiao Liu, and Hua Jiang, Nanotechnology **32**, 402001 (2021).

[215] Long Ju, Zhiwen Shi, Nityan Nair, Yinchuan Lv, Chenhao Jin, Jairo Velasco, Claudia Ojeda-Aristizabal, Hans A. Bechtel, Michael C. Martin, Alex Zettl, James Analytis, and Feng Wang, Nature **520**, 650 (2015).

[216] Shu-guang Cheng, Jiaojiao Zhou, Hua Jiang, and Qing-Feng Sun, New Journal of Physics **18**, 103024 (2016).

[217] Jing Li, Ke Wang, Kenton J. McFaul, Zachary Zern, Yafei Ren, Kenji Watanabe, Takashi Taniguchi, Zhenhua Qiao, and Jun Zhu, Nature Nanotechnology **11**, 1060 (2016).

[218] Shu-guang Cheng, Haiwen Liu, Hua Jiang, Qing-Feng Sun, and X. C. Xie, Phys. Rev. Lett. **121**, 156801 (2018).

[219] F. D. M. Haldane, Phys. Rev. Lett. **61**, 2015 (1988).

[220] Sergej Konschuh, Martin Gmitra, and Jaroslav Fabian, Phys. Rev. B **82**, 245412 (2010).

[221] Klaus Zollner, Aron W. Cummings, Stephan Roche, and Jaroslav Fabian, Phys. Rev. B **103**, 075129 (2021).

[222] Yunyou Yang, Zhong Xu, L. Sheng, Baigeng Wang, D. Y. Xing, and D. N. Sheng, Phys. Rev. Lett. **107**, 066602 (2011).

[223] Franz Herling, C. K. Safeer, Josep Ingla-Aynés, Nerea Ontoso, Luis E. Hueso, and Fèlix Casanova, APL Materials **8**, 071103 (2020).

[224] Petra Högl, Tobias Frank, Klaus Zollner, Denis Kochan, Martin Gmitra, and Jaroslav Fabian, Phys. Rev. Lett. **124**, 136403 (2020).

[225] Mahdi Zarea and Nancy Sandler, Phys. Rev. B **79**, 165442 (2009).

[226] Z. Wang, D.-K. Ki, J. Y. Khoo, D. Mauro, H. Berger, L. S. Levitov, and A. F. Morpurgo, Phys. Rev. X **6**, 041020 (2016).

[227] Zahra Khatibi and Stephen R. Power, Phys. Rev. B **106**, 125417 (2022).

[228] Klaus Zollner, Marcin Kurpas, Martin Gmitra, and Jaroslav Fabian, Nature Reviews Physics **7**, 255 (2025).

[229] W. Meissner and R. Ochsenfeld, Naturwissenschaften **21**, 787 (1933).

[230] H. Kamerlingh Onnes, Koninklijke Nederlandse Akademie van Wetenschappen Proceedings Series B Physical Sciences **14**, 113 (1911).

[231] V. L. Ginzburg and L. D. Landau, Theory of superconductivity, 1950.

[232] J. Bardeen, L. N. Cooper, and J. R. Schrieffer, Phys. Rev. **108**, 1175 (1957).

[233] Christian Baumgartner, Semiconductor-Superconductor Josephson Junctions in the Presence of Zeeman and Spin-Orbit Fields, *PhD Thesis*, 2023.

[234] Michael Tinkham and Victor Emery, Physics Today **49**, 74 (1996).

[235] G. Grosso and G.P. Parravicini, Solid State Physics (Elsevier Science, London, 2000).

[236] B. Pannetier and H. Courtois, Journal of Low Temperature Physics **118**, 599 (2000).

[237] B.D. Josephson, Advances in Physics **14**, 419 (1965).

[238] D. Newell and E. Tiesinga, The International System of Units (SI), 2019 Edition, https://doi.org/10.6028/NIST.SP.330-2019, 2019.

[239] Federico Bonasera, Giuseppe A. Falci, Elisabetta Paladino, and Francesco M. D. Pellegrino, The European Physical Journal Special Topics (2025).

[240] Morten Kjaergaard, Mollie E. Schwartz, Jochen Braumüller, Philip Krantz, Joel I.-J. Wang, Simon Gustavsson, and William D. Oliver, Annual Review of Condensed Matter Physics **11**, 369 (2020).

[241] L. Casparis, T. W. Larsen, M. S. Olsen, F. Kuemmeth, P. Krogstrup, J. Nygård, K. D. Petersson, and C. M. Marcus, Phys. Rev. Lett. **116**, 150505 (2016).

[242] G. de Lange, B. van Heck, A. Bruno, D. J. van Woerkom, A. Geresdi, S. R. Plissard, E. P. A. M. Bakkers, A. R. Akhmerov, and L. DiCarlo, Phys. Rev. Lett. **115**, 127002 (2015).

[243] Albert Hertel, Michaela Eichinger, Laurits O. Andersen, David M.T. van Zanten, Sangeeth Kallatt, Pasquale Scarlino, Anders Kringhøj, José M. Chavez-Garcia, Geoffrey C. Gardner, Sergei Gronin, Michael J. Manfra, András Gyenis, Morten Kjaergaard, Charles M. Marcus, and Karl D. Petersson, Phys. Rev. Appl. **18**, 034042 (2022).

[244] William M. Strickland, Lukas J. Baker, Jaewoo Lee, Krishna Dindial, Bassel Heiba Elfeky, Patrick J. Strohbeen, Mehdi Hatefipour, Peng Yu, Ido Levy, Jacob Issokson, Vladimir E. Manucharyan, and Javad Shabani, Phys. Rev. Res. **6**, 023094 (2024).

[245] Giordano Scappucci, Christoph Kloeffel, Floris A. Zwanenburg, Daniel Loss, Maksym Myronov, Jian-Jun Zhang, Silvano De Franceschi, Georgios Katsaros, and Menno Veldhorst, Nature Reviews Materials **6**, 926 (2021).

[246] Axel Leblanc, Chotivut Tangchingchai, Zahra Sadre Momtaz, Elyjah Kiyooka, Jean-Michel Hartmann, Gonzalo Troncoso Fernandez-Bada, Zoltán Scherübl, Boris Brun, Vivien Schmitt, Simon Zihlmann, Romain Maurand, Étienne Dumur, Silvano De Franceschi, and Fran çois Lefloch, Phys. Rev. Res. **6**, 033281 (2024).

[247] Elyjah Kiyooka, Chotivut Tangchingchai, Leo Noirot, Axel Leblanc, Boris Brun, Simon Zihlmann, Romain Maurand, Vivien Schmitt, Étienne Dumur, Jean-Michel Hartmann, Francois Lefloch, and Silvano De Franceschi, Nano Letters **25**, 562 (2025), pMID: 39690124.

[248] Joel I-Jan Wang, Daniel Rodan-Legrain, Landry Bretheau, Daniel L. Campbell, Bharath Kannan, David Kim, Morten Kjaergaard, Philip

Krantz, Gabriel O. Samach, Fei Yan, Jonilyn L. Yoder, Kenji Watanabe, Takashi Taniguchi, Terry P. Orlando, Simon Gustavsson, Pablo Jarillo-Herrero, and William D. Oliver, Nature Nanotechnology **14**, 120 (2019).

[249] M F Goffman, C Urbina, H Pothier, J Nygård, C M Marcus, and P Krogstrup, New Journal of Physics **19**, 092002 (2017).

[250] Michael Hell, Martin Leijnse, and Karsten Flensberg, Phys. Rev. Lett. **118**, 107701 (2017).

[251] Karsten Flensberg, Phys. Rev. B **48**, 11156 (1993).

[252] K. A. Matveev, Phys. Rev. B **51**, 1743 (1995).

[253] Yuli V. Nazarov, Phys. Rev. Lett. **82**, 1245 (1999).

[254] A. Kringhøj, B. van Heck, T. W. Larsen, O. Erlandsson, D. Sabonis, P. Krogstrup, L. Casparis, K. D. Petersson, and C. M. Marcus, Phys. Rev. Lett. **124**, 246803 (2020).

[255] Carlo Ciaccia, Roy Haller, Asbjørn C. C. Drachmann, Tyler Lindemann, Michael J. Manfra, Constantin Schrade, and Christian Schönenberger, Phys. Rev. Res. **5**, 033131 (2023).

[256] Peter Brooks, Alexei Kitaev, and John Preskill, Phys. Rev. A **87**, 052306 (2013).

[257] W. C. Smith, A. Kou, X. Xiao, U. Vool, and M. H. Devoret, npj Quantum Information **6**, 8 (2020).

[258] Constantin Schrade, Charles M. Marcus, and András Gyenis, PRX Quantum **3**, 030303 (2022).

[259] Andrea Maiani, Morten Kjaergaard, and Constantin Schrade, PRX Quantum **3**, 030329 (2022).

[260] Simon Messelot, Nicolas Aparicio, Elie de Seze, Eric Eyraud, Johann Coraux, Kenji Watanabe, Takashi Taniguchi, and Julien Renard, Phys. Rev. Lett. **133**, 106001 (2024).

[261] Axel Leblanc, Chotivut Tangchingchai, Zahra Sadre Momtaz, Elyjah Kiyooka, Jean-Michel Hartmann, Frédéric Gustavo, Jean-Luc Thomassin, Boris Brun, Vivien Schmitt, Simon Zihlmann, Romain Maurand, Étienne Dumur, Silvano De Franceschi, and François Lefloch, Nature Communications **16**, 1010 (2025).

[262] C. W. J. Beenakker, Rev. Mod. Phys. **69**, 731 (1997).

[263] P. G. de Gennes and D. Saint-James, Physics Letters **4**, 151 (1963).

[264] A F Andreev, Zh. Eksperim. i Teor. Fiz. **Vol: 46**, (1964).

[265] Fabrizio Dolcini, "Andreev reflection." Lecture Notes for XXIII Physics GradDays 5 (2009): 9, arXiv:1810.04588.

[266] Muhammad Irfan and Anton R. Akhmerov, (2018), arXiv:1810.04588.

[267] C.W.J. Beenakker and H. van Houten, in Nanostructures and Mesoscopic Systems, edited by Wiley P. Kirk and Mark A. Reed (Academic Press, New York, 1992), pp. 481–497.

[268] C. W. J. Beenakker, in Transport Phenomena in Mesoscopic Systems, edited by Hidetoshi Fukuyama and Tsuneya Ando (Springer Berlin Heidelberg, Berlin, Heidelberg, 1992), pp. 235–253.

[269] M. Titov and C. W. J. Beenakker, Phys. Rev. B **74**, 041401 (2006).

[270] I. Hagymási, A. Kormányos, and J. Cserti, Phys. Rev. B **82**, 134516 (2010).

[271] Léon Van Hove, Phys. Rev. **89**, 1189 (1953).

[272] W. Kohn and J. M. Luttinger, Phys. Rev. Lett. **15**, 524 (1965).

[273] J. E. Hirsch and D. J. Scalapino, Phys. Rev. Lett. **56**, 2732 (1986).

[274] IE Dzyaloshinskii, Zhurnal Eksperimental'noi i Teoreticheskoi Fiziki **93**, 1487 (1987).

[275] R. S. Markiewicz, in High-Temperature Superconductivity: Physical Properties, Microscopic Theory, and Mechanisms, edited by Josef Ashkenazi, Stewart E. Barnes, Fulin Zuo, Gary C. Vezzoli, and Barry M. Klein (Springer US, Boston, MA, 1991), pp. 555–560.

[276] D. M. Newns, H. R. Krishnamurthy, P. C. Pattnaik, C. C. Tsuei, and C. L. Kane, Phys. Rev. Lett. **69**, 1264 (1992).

[277] R.S Markiewicz, Journal of Physics and Chemistry of Solids **58**, 1179 (1997).

[278] J. González, Phys. Rev. B **78**, 205431 (2008).

[279] Guohong Li, A. Luican, J. M. B. Lopes dos Santos, A. H. Castro Neto, A. Reina, J. Kong, and E. Y. Andrei, Nature Physics **6**, 109 (2009).

[280] J. L. McChesney, Aaron Bostwick, Taisuke Ohta, Thomas Seyller, Karsten Horn, J. González, and Eli Rotenberg, Phys. Rev. Lett. **104**, 136803 (2010).

[281] Kyoo Kim, Sooran Kim, J. S. Kim, Heejung Kim, J.-H. Park, and B. I. Min, Phys. Rev. B **97**, 165102 (2018).

[282] Hiroki Isobe, Noah F. Q. Yuan, and Liang Fu, Phys. Rev. X **8**, 041041 (2018).

[283] Yury Sherkunov and Joseph J. Betouras, Phys. Rev. B **98**, 205151 (2018).

[284] Xianxin Wu, Tilman Schwemmer, Tobias Müller, Armando Consiglio, Giorgio Sangiovanni, Domenico Di Sante, Yasir Iqbal, Werner Hanke, Andreas P. Schnyder, M. Michael Denner, Mark H. Fischer, Titus Neupert, and Ronny Thomale, Physical Review Letters **127**, (2021).

[285] Wen Wan, Rishav Harsh, Paul Dreher, Fernando de Juan, and Miguel M. Ugeda, npj 2D Materials and Applications **7**, 41 (2023).

[286] Mingu Kang, Shiang Fang, Jeong-Kyu Kim, Brenden R. Ortiz, Sae Hee Ryu, Jimin Kim, Jonggyu Yoo, Giorgio Sangiovanni, Domenico Di Sante, Byeong-Gyu Park, Chris Jozwiak, Aaron Bostwick, Eli Rotenberg, Efthimios Kaxiras, Stephen D. Wilson, Jae-Hoon Park, and Riccardo Comin, Nature Physics **18**, 301 (2022).

[287] T. M. Rice and G. K. Scott, Phys. Rev. Lett. **35**, 120 (1975).

[288] M. Cranney, F. Vonau, P. B. Pillai, E. Denys, D. Aubel, M. M. De Souza, C. Bena, and L. Simon, EPL (Europhysics Letters) **91**, 66004 (2010).

[289] D. Makogon, R. van Gelderen, R. Roldá n, and C. Morais Smith, Physical Review B **84**, (2011).

[290] Eduardo Fradkin, Field Theories of Condensed Matter Physics, 2 ed. (Cambridge University Press, Cambridge, 2013).

[291] Cheng-Cheng Liu, Li-Da Zhang, Wei-Qiang Chen, and Fan Yang, Phys. Rev. Lett. **121**, 217001 (2018).

[292] Su-Yang Xu, Chang Liu, I. Belopolski, S. K. Kushwaha, R. Sankar, J. W. Krizan, T.-R. Chang, C. M. Polley, J. Adell, T. Balasubramanian, K. Miyamoto, N. Alidoust, Guang Bian, M. Neupane, H.-T. Jeng, C.-Y. Huang, W.-F. Tsai, T. Okuda, A. Bansil, F. C. Chou, R. J. Cava, H. Lin, and M. Z. Hasan, Phys. Rev. B **92**, 075115 (2015).

[293] Bahadur Singh, Xiaoting Zhou, Hsin Lin, and Arun Bansil, Phys. Rev. B **97**, 075125 (2018).

[294] Barun Ghosh, Sougata Mardanya, Bahadur Singh, Xiaoting Zhou, Baokai Wang, Tay-Rong Chang, Chenliang Su, Hsin Lin, Amit Agarwal, and Arun Bansil, Phys. Rev. B **100**, 235101 (2019).

[295] Jian Wang and Luiz H. Santos, Phys. Rev. Lett. **125**, 236805 (2020).

[296] Shuang Wu, Zhenyuan Zhang, K. Watanabe, T. Taniguchi, and Eva Y. Andrei, Nature Materials **20**, 488 (2021).

[297] Kyungchan Lee, Gunnar F. Lange, Lin-Lin Wang, Brinda Kuthanazhi, Thaís V. Trevisan, Na Hyun Jo, Benjamin Schrunk, Peter P. Orth, Robert-Jan Slager, Paul C. Canfield, and Adam Kaminski, Nature Communications **12**, 1855 (2021).

[298] Yong Hu, Xianxin Wu, Yongqi Yang, Shunye Gao, Nicholas C. Plumb, Andreas P. Schnyder, Weiwei Xie, Junzhang Ma, and Ming Shi, (2022), arXiv:2205.15927.

[299] Xu-Gang He, Xiaoxiang Xi, and Wei Ku, (2014), arXiv:1410.2885.

[300] Hong Yao and Fan Yang, Phys. Rev. B **92**, 035132 (2015).

[301] Yong Hu, Xianxin Wu, Brenden R. Ortiz, Sailong Ju, Xinloong Han, Junzhang Ma, Nicholas C. Plumb, Milan Radovic, Ronny Thomale, Stephen D. Wilson, Andreas P. Schnyder, and Ming Shi, Nature Communications **13**, (2022).

[302] F. Bonasera, S.-B. Zhang, L. Privitera, and F. M. D. Pellegrino, Phys. Rev. B **106**, 195115 (2022).

[303] S. Tchoumakov, V. Jouffrey, A. Inhofer, E. Bocquillon, B. Plaçais, D. Carpentier, and M. O. Goerbig, Phys. Rev. B **96**, 201302 (2017).

[304] Song-Bo Zhang, Hai-Zhou Lu, and Shun-Qing Shen, New Journal of Physics **18**, 053039 (2016).

[305] Zhenhua Wu, F. M. Peeters, and Kai Chang, Phys. Rev. B **82**, 115211 (2010).

[306] M. Titov, Europhysics Letters **79**, 17004 (2007).

[307] F. M. D. Pellegrino, G. G. N. Angilella, and R. Pucci, Phys. Rev. B **84**, 195404 (2011).

[308] F. M. D. Pellegrino, G. Falci, and E. Paladino, Communications Physics **5**, 265 (2022).

[309] Ignazio Vacante, Francesco M. D. Pellegrino, G. G. N. Angilella, Giuseppe A. Falci, and Elisabetta Paladino, Phys. Rev. Res. **7**, 013189 (2025).

[310] Wolfram Research, Inc., Mathematica, Version 14.1, champaign, IL, 2024.

[311] J. Tworzydło, B. Trauzettel, M. Titov, A. Rycerz, and C. W. J. Beenakker, Phys. Rev. Lett. **96**, 246802 (2006).

[312] O. Klein, Zeitschrift für Physik **53**, 157 (1929).

[313] P. Rout, N. Papadopoulos, F. Peñaranda, K. Watanabe, T. Taniguchi, E. Prada, P. San-Jose, and S. Goswami, Nature Communications **15**, 856 (2024).

[314] Christoph W Groth, Michael Wimmer, Anton R Akhmerov, and Xavier Waintal, New Journal of Physics **16**, 063065 (2014).

[315] Ming-Hao Liu, Peter Rickhaus, Péter Makk, Endre Tóvári, Romain Maurand, Fedor Tkatschenko, Markus Weiss, Christian Schönenberger, and Klaus Richter, Phys. Rev. Lett. **114**, 036601 (2015).

[316] V. V. Ivanovskaya, P. Wagner, A. Zobelli, I. Suarez-Martinez, A. Yaya, and C. P. Ewels, in GraphITA 2011, edited by Luca Ottaviano and Vittorio Morandi (Springer Berlin Heidelberg, Berlin, Heidelberg, 2012), pp. 75–85.

[317] B. Baxevanis, V. P. Ostroukh, and C. W. J. Beenakker, Phys. Rev. B **91**, 041409 (2015).

[318] R. C. Dynes and T. A. Fulton, Phys. Rev. B **3**, 3015 (1971).

[319] Jian Li, Ivar Martin, Markus Büttiker, and Alberto F. Morpurgo, Nature Physics **7**, 38 (2011).

[320] Fuyuki Ando, Yuta Miyasaka, Tian Li, Jun Ishizuka, Tomonori Arakawa, Yoichi Shiota, Takahiro Moriyama, Youichi Yanase, and Teruo Ono, Nature **584**, 373 (2020).

[321] Christian Baumgartner, Lorenz Fuchs, Andreas Costa, Simon Reinhardt, Sergei Gronin, Geoffrey C. Gardner, Tyler Lindemann, Michael J. Manfra, Paulo E. Faria Junior, Denis Kochan, Jaroslav Fabian, Nicola Paradiso, and Christoph Strunk, Nature Nanotechnology **17**, 39 (2022).

[322] Kun-Rok Jeon, Jae-Keun Kim, Jiho Yoon, Jae-Chun Jeon, Hyeon Han, Audrey Cottet, Takis Kontos, and Stuart S. P. Parkin, Nature Materials **21**, 1008 (2022).

[323] Bianca Turini, Sedighe Salimian, Matteo Carrega, Andrea Iorio, Elia Strambini, Francesco Giazotto, Valentina Zannier, Lucia Sorba, and Stefan Heun, Nano Letters **22**, 8502 (2022), pMID: 36285780.

[324] Pei-Hao Fu, Yong Xu, Shengyuan A. Yang, Ching Hua Lee, Yee Sin Ang, and Jun-Feng Liu, Phys. Rev. Appl. **21**, 054057 (2024).

[325] Muhammad Nadeem, Michael S. Fuhrer, and Xiaolin Wang, Nature Reviews Physics **5**, 558 (2023).

[326] Sayak Bhowmik, Dibyendu Samanta, Ashis K. Nandy, Arijit Saha, and Sudeep Kumar Ghosh, Communications Physics **8**, 260 (2025).

[327] Lucia Vigliotti, Alessio Calzona, Niccolò Traverso Ziani, F. Sebastian Bergeret, Maura Sassetti, and Björn Trauzettel, Nanomaterials **13**, (2023).

[328] Motohiko Ezawa and Naoto Nagaosa, Phys. Rev. B **88**, 121401 (2013).